Developing Parameter Constraints for Radar-based SWE Retrievals

by

Aaron Thompson

A thesis
presented to the University of Waterloo
in fulfillment of the
thesis requirement for the degree of
Doctor of Philosophy
in
Geography

Waterloo, Ontario, Canada, 2021

Examining Committee Membership

The following served on the Examining Committee for this thesis. The decision of the Examining Committee is by majority vote.

External Examiner	Richard Forster Professor, Geography The University of Utah
Supervisor	Richard Kelly Professor, Geography and Environmental Management University of Waterloo.
Internal Members	Claude Duguay Professor, Geography and Environmental Management University of Waterloo.
	Joshua King Adjunct Professor, Geography and Environmental Management University of Waterloo. Research Scientist, Climate Research Division Environment and Climate Change Canada.
Internal-external Member	Tony Endres Associate Professor, Earth and Environmental Sciences University of Waterloo.

AUTHOR'S DECLARATION

This thesis consists of material all of which I authored or co-authored: see Statement of Contributions included in the thesis. This is a true copy of the thesis, including any required final revisions, as accepted by my examiners.

I understand that my thesis may be made electronically available to the public.

Statement of Contributions

This manuscript-style thesis includes introductory material in Chapters 1 through 5, followed by manuscripts, published or submitted for review in peer-reviewed journals, in Chapters 6, 7, and 8. Thesis conclusions were presented in Chapter 9.

Aaron Thompson was the sole author of the introductory material and conclusions in Chapters 1 through 5 and Chapter 9, written under the supervision of Richard Kelly. This material was not written or submitted for publication in its current form.

Chapter 6 was published in the peer-reviewed journal, Canadian Journal of Remote Sensing (see Thompson et al., 2021a). Conceptualization, radar measurements and field data collection were a collaborative effort between Aaron Thompson and Richard Kelly with assistance in field data collection from Grant Gunn, Andrew Kasurak, Qinghuan Li, and Vicky Vanthof. The manuscript was written by Aaron Thompson and edited by Richard Kelly.

Chapter 7 is currently in review with the peer-reviewed journal, Remote Sensing Letters (see Thompson et al., 2021b). Conceptualization was a collaborative effort between Aaron Thompson and Richard Kelly. Radar measurements and field data collection was completed by Aaron Thompson with assistance from Vicky Vanthof. The manuscript was written by Aaron Thompson and edited by Richard Kelly.

Chapter 8 has been published in the peer reviewed journal, Remote Sensing (see Thompson et al., 2019). Conceptualization of the manuscript was a collaborative effort between Aaron Thompson and Richard Kelly. Radar measurements were completed by Aaron Thompson and Richard Kelly in Grand Mesa, CO during the SnowEx17 campaign (see Kelly and Thompson, 2018). Snow pit observations in Grand Mesa were managed, collected, and processed by Kelly Elder, Ludovic Brucker, Chris Hiemstra, and H.P. Marshall (see Elder et al., 2018). Snow microstructure measurements in Grand Mesa were collected and processed by Nick Rutter, Jinmei Pan, Mike Durand, Joshua King, Chris Derksen, Fanny Larue, Michaela Teich, and Mike Brady (see Derksen et al., 2017 and Rutter et al., 2018). Radar measurements and field data collection in Trail Valley Creek, NT was completed by Aaron Thompson with assistance from Vicky Vanthof. Radar measurements and field data collection in Tobermory, ON was a collaboration between Aaron Thompson and John Coughlin. Radar measurements and field observations Churchill, MB were made during the Can-CSI/CASIX campaign by Joshua King, Andrew Kasurak, Richard Kelly, Grant Gunn, and Claude Duguay. The manuscript was written by Aaron Thompson and edited by Richard Kelly.

Abstract

Terrestrial snow is an important freshwater reservoir with significant influence on the climate and energy balance. It exhibits natural spatiotemporal variability which has been enhanced by climate change, thus it is important to monitor on a large scale. Active microwave, or radar remote sensing has shown frequency-dependent promise in this regard, however, interpretation remains a challenge. The aim of this thesis was to develop constraints for radar based SWE retrievals which characterize and limit uncertainty with a focus on the underlying physical processes, snowpack stratigraphy, the influence of vegetation, and effects of background scattering.

The University of Waterloo Scatterometer (UWScat) was used to make measurements at 9.6 and 17.2 GHz of snow and bare ground in a series of field-based campaigns in Maryhill and Englehart, ON, Grand Mesa, CO (NASA SnowEx campaign, year 1), and Trail Valley Creek, NT. Additional measurements from Tobermory, ON, and Churchill, MB (Canadian Snow and Ice Experiment) were included. The Microwave Emission Model for Layered Snowpacks, Version 3, adapted for backscattering (MEMLS3&a) was used to explore snowpack parameterization and SWE retrieval and the Freeman-Durden three component decomposition (FD3c) was used to leverage the polarimetric response.

Physical processes in the snow accumulation environment demonstrated influence on regional snowpack parameterization and constraints in a SWE retrieval context with a single-layer snowpack parameterization for Maryhill, ON and a two-layer snowpack parameterization for Englehart, ON resulting in a retrieval RMSE of 21.9 mm SWE and 24.6 mm SWE, respectively. Use of *in situ* snow depths improved RMSE to 12.0 mm SWE and 10.9 mm SWE, while accounting for soil scattering effects further improved RMSE by up to 6.3 mm SWE. At sites with vegetation and ice lenses, RMSE improved from 60.4 mm SWE to 21.1 mm SWE when *in situ* snow depths were used. These results compare favorably with the common accuracy requirement of RMSE $\leq$ 30 mm and underscore the importance of understanding the driving physical processes in a snow accumulation environment and the utility of their regional manifestation in a SWE retrieval context. A relationship between wind slab thickness and the double-bounce component of the FD3c in a tundra snowpack was introduced for incidence angles $\geq 46°$ and wind slab thickness $\geq$ 19 cm. Estimates of wind slab thickness and SWE resulted in an RMSE of 6.0 cm and 5.5 mm, respectively. The increased double-bounce scattering was associated with path length increase within a growing wind slab layer. Signal attenuation in a sub-canopy SWE retrieval was also explored. The volume scattering component of the FD3c yielded similar

performance to forest fraction in the retrieval with several distinct advantages including a real-time description of forest condition, accounting for canopy geometry without ancillary information, and providing coincident information on forest canopy in remote locations.

Overall, this work demonstrated how physical processes can manifest regional outcomes, it quantified effects of natural inclusions and background scattering on SWE retrievals, it provided a means to constrain wind slab thickness in a tundra environment, and it improved characterization of coniferous forest in a sub-canopy SWE retrieval context. Future work should focus on identifying ice and vegetation conditions prior to SWE retrieval, testing the spatiotemporal validity of the methods developed herein, and finally, improving the integration of snowpack attenuation within retrieval efforts.

Acknowledgements

First of all, I would like to extend sincere gratitude to Dr. Richard Kelly for his support, guidance in supervision, and for providing the many opportunities which have encouraged growth and development in both an academic and a personal sense; He has been and continues to be a formidable mentor. I would also like to thank my committee members, Drs. Claude Duguay (GEM), Tony Enders (Earth Sciences), Joshua King (ECCC), and my external examiner, yet to be named, for your time, effort, and insightful discourse and suggestions.

I would like to acknowledge those who made my research possible through funding or support in kind: The Aurora Research Institute (ARI), the National Aeronautics and Space Administration (NASA), the Natural Sciences and Engineering Research Council of Canada (NSERC), the Northern Scientific Training Program (NSTP), the Ontario Graduate Scholarship (OGS), the Polar Continental Shelf Program (PCSP), and the University of Waterloo.

Thanks to the friends I've met on this journey. Thanks to those who lit the way before me - Joshua King, Andrew Kasurak, and Grant Gunn. Thanks to my contemporaries, who provided thoughtful encouragement, debate, and discussion -Qinghuan Li, Nastaran Saberi, Vicky Vanthof, and Margot Flemming, and very special thanks to Vicky Vanthof for helping me dig out more than 30 tonnes of snow in Trail Valley Creek.

Finally, and most importantly, thanks to my family – Vigy Yu, Mary Thompson, Doug Thompson, Sonia & Don Scott, and Alison & Jack Albert. Your boundless support provided the means and the courage to climb this mountain.

"If I have seen further it is by standing on the shoulders of Giants."

- Sir Isaac Newton (1642-1727)

Table of Contents

List of Figures

List of Tables

List of Abbreviations

A	Area resolved on the ground, used to normalize σ
A(x)	Snow grain correlation function
a.s.l.	Above sea level
A_i	Depolarization terms (A_1, A_2, and A_3)
AWI	Alfred Wegener Institute
bi	Basal ice
C	Covariance matrix
CASIX	Canadian Snow and Ice Experiment
CLPX	Cold Land Processes Experiment
CoReH20	Cold Regions Hydrology High-Resolution Observatory
D	Antenna diameter
dB	Decibel. Unit of power estimate on logarithmic scale
D_{max}	Maximum extent of a representative sample of snow grains
DMRT	Dense Media Radiative Transfer model
DUFISSS	Dual Frequency Integrating Sphere for snow SSA measurement. Precursor to IRIS
e	Emissivity
E_{0x}	Orthogonal component of an electric field in the x-dimension
E_{0y}	Orthogonal component of an electric field in the y-dimension
EN	Englehart
fd	Double-bounce scattering component of the Freeman-Durden 3-component decomposition
FD3c	Freeman-Durden 3-component decomposition
FF	Forest cover fraction
FFT	Fast Fourier transform
FM	Frequency modulated
FMCW	Frequency modulated, continuous wave
FOV	Radar field-of-view
FOV	Field of view
FP	General forest parameter (either VFD or FF)
fs	Surface scattering component of the Freeman-Durden 3-component decomposition
fv	Volume scattering component of the Freeman-Durden 3-component decomposition

G	Antenna gain
gv	Green vegetation
h	Standard deviation of surface height
H	Horizontal polarization
h_{ant}	Antenna height
h_{opt}	Optimized h
HUT	Helsinki University of Technology model
I	Fourier integral of the autocorrelation function
IBA	Improved Born Approximation
IRIS	Infrared Integrating Sphere. Successor to DUFFISS
j	The unit imaginary number, equivalent to the square root of -1
k	Wavenumber
K^2	Ratio of the mean squared electric fields inside and outside of the snow grain
k_a	Absorption coefficient
k_e	Extinction coefficient
k'_e	Normalized extinction coefficient
k_{eff}	Effective wavenumber of a wave with an apparent permittivity of ε_a
k_s	Scattering coefficient
MEMLS	Microwave Emission Model for Layered Snowpacks
MEMLS3&a	MEMLS version 3, adapted for backscattering
MH	Maryhill
mi	Mid-pack ice
M_v	Volumetric liquid water content
N_{ind}	Number of independent samples
N_n	Number of noise samples
obs	Observed
P	Summation of contributions from each scattering mechanism in the Freeman-Durden 3-component decomposition
p_c	Correlation length
P_d	Estimated contribution to double-bounce scattering in the Freeman-Durden 3-component decomposition
p_{double}	Proportion of double-bounce scattering
p_{ex}	Exponential correlation length
pq	Send-receive polarization state

P_r	Power returned to the radar antenna
P_r	Power measured from a given scene
P_{rc}	Power measured from the calibration target
P_s	Estimated contribution to surface scattering in the Freeman-Durden 3-component decomposition
P_t	Power transmitted from the radar antenna
P_v	Estimated contribution to volume scattering in the Freeman-Durden 3-component decomposition
r_t	Range to target
r	Reflectivity of a surface
R_c	Range to calibration target
r_{co}	Co-polarization ratio
r_{depol}	Depolarization ratio
Ret	Retrieved value
RF	Radio-frequency
r_f	Far-field distance
R_{gh}	Horizontal Fresnel reflectivity coefficient from a horizontal surface (eg. the ground)
R_{gv}	Vertical Fresnel reflectivity coefficient from a horizontal surface (eg. the ground)
R_H	Horizontal Fresnel reflectivity coefficient
r_t	Range-to-target
R_{th}	Horizontal Fresnel reflectivity coefficient from a vertical surface (eg. a tree trunk)
R_{tv}	Vertical Fresnel reflectivity coefficient from a vertical surface (eg. a tree trunk)
R_V	Vertical Fresnel reflectivity coefficient
S_a	Salinity
S	Scattering matrix
s	Number of sites
S_0	Reflectivity at the snow-soil interface
S_{int}	Reflectivity of interfaces between snow layers
SAR	Synthetic aperture radar
SCR	Signal-to-clutter ratio
s_d	Diffuse component of simulated backscatter in MEMLS3&a
S_H	H-polarized rough soil reflectivity
si	Surface ice
sim	Simulated

SMP	Snow micropenetrometer
SMRT	Snow Microwave Radiative Transfer Model
SNR	Signal-to-noise ratio
s_s	Specular component of simulated backscatter in MEMLS3&a
S_{d0}	Diffuse reflectivity at the snow-soil interface
S_{s0}	Specular reflectivity at the snow-soil interface
SSA	Specific surface area of snow (m^2/kg)
S_V	V-polarized rough soil reflectivity
SWE	Snow water equivalent (mm)
t	Temperature
T	Total backscattered power
$t_{two\text{-}way}$	Two-way transmissivity
TVC	Trail Valley Creek, NT
u	Layer transmissivity
UWScat	University of Waterloo Scatterometer
v	Volume fraction of the snowpack
V	Vertical polarization
V_{FD}	Volume scattering proportion derived from the Freeman-Durden 3-component decomposition
$\hat{x}$	Vector defining a plane in the x-dimension
$\hat{y}$	Vector defining a plane in the y-dimension
Z	Layer thickness
α	Dihedral scattering term in the Freeman-Durden 3-component decomposition
β	Bragg scattering term
γ_h	Propagation term for horizontal polarization
$\Gamma_{res}^{\pm}$	Multiplicative bias errors in UWScat measurement
$\Gamma_{cal}^{\pm}$	Residual multiplicative bias errors in UWScat measurement
Γ_r	Range-dependent correction factor
γ_v	Propagation term for vertical polarization
δ	Phase difference between E0x and E0y
δ_p	Penetration depth
$\Delta_{total}^{\pm}$	Total error in UWScat measurements
ϵ	Quantification of uncertainty
ε'	Real portion of complex relative permittivity, describes electrical storage

ε''	Imaginary portion of complex relative permittivity, describes loss or dissipation of energy
ε_a	Apparent permittivity
ε'_{ds}	Real portion of complex relative permittivity of dry snow
ε''_{ds}	Imaginary portion of complex relative permittivity of dry snow
ε''_{ice}	Imaginary portion of complex relative permittivity of ice
ε_h	Complex relative permittivity of host medium in conceptual snowpack (air)
ε_r	Complex relative permittivity
ε_s	Complex relative permittivity of inclusions in conceptual snowpack (ice particles)
ε'_{snow}	Real portion of complex relative permittivity of snow (non-specific)
ε'_{soil}	Real portion of complex relative permittivity of soil
ε''_{soil}	Imaginary portion of complex relative permittivity of soil
ζ	Scattering parameter for derivation of I
θ'	Angle of refraction
θ_{3dB}	One-way half-power beamwidth of the antenna
θ	Incidence angle
θ_p	Polarization angle (between the incident electric field and the direction of the scattered radiation)
λ	Wavelength
μCT	Micro-computed tomography
ρ_{ds}	Density of dry snow
ρ_{snow}	Density of snow (non-specific)
σ	Radar cross section
σ°	Normalized radar cross section
σ°_{obs}	Observed normalized radar cross section of sub-canopy snow target
σ°_{snow}	Retrieved normalized radar cross section of sub-canopy snow target
σ^{as}	Backscattering from the air-snow interface
σ_c	Radar cross section of the calibration target
$\sigma^{g'}$	Backscattering from the snow-ground interface
σ^{gv}	Backscattering from the interaction between the ground and snow volume
σ_{ran}	Random error in UWScat measurement
σ^t	Total backscattering
σ^v	Backscattering from the snow volume
$\varphi_{s\text{-}i}$	Scattering angle (angle between propagation direction of incident and scattered waves)
Φ	Microstructure scaling factor

Φ_{opt}	Optimized Φ
Φ_{VVHH}	Co-polarized phase difference
χ	Ellipticity angle
Ψ	Orientation angle

Chapter 1
Introduction

1.1 Motivation

Snow is a thermodynamically active material which exists at or near its melting temperature (Colbeck, 1982). Its widespread terrestrial accumulation acts as an important freshwater storage reservoir and at its seasonal peak, more than $3x10^3$ gigatonnes of snow blanket the Northern Hemisphere annually (Pulliainen et al., 2020). It has also been described as the most variable of all land surface conditions (Cohen, 1994) so uncertainty in its quantification is unsurprising (eg. Mudryk et al., 2015).

From a human perspective, annual runoff is snowmelt-dominated across much of the Northern Hemisphere and provides a source of freshwater for 17% of the global population (Barnett et al., 2005). It also contributes to hydropower generation which accounts for 20% of global power production (Sturm et al., 2015) and in some regions flooding from snowmelt is a safety concern posing risk to life and property (Borkhorst et al., 2015; Tuttle et al. 2017) such as the Red River basin flood in 1997 which resulted in $500 million CAD in damages in southern Manitoba (Rannie, 2016).

From a climate perspective, snow is an important component of the global energy balance given its high albedo and insulative properties which modulate the energy exchange at or near the Earth's surface (Henderson, et al., 2018) and has important implications for surface cooling, and subnivean conditions. The former is directly linked to the observed positive feedback in which an accelerated reduction in snow cover occurs with the enhanced warming associated with lower-albedo surfaces that result from reduced snow cover, particularly during spring (Flanner et al., 2011). The latter allows ecological activity to continue beneath the snow throughout winter (Pulliainen et al., 2020), exerts control on winter season carbon fluxes in permafrost regions (Natali et al., 2019) and influences permafrost distribution (Bormann et al., 2018). Snow is also an important input for Earth system models given its influence on the energy exchange (Mudryk et al., 2020; Pulliainen et al. 2020).

Given the demonstrated importance of snow, large scale remote measurement has remained a longstanding priority (eg. Kukla, 1978; Matson and Wiesnet, 1981; National Academy of Sciences, 2019; Riseborough et al., 1990; IGOS 2007; Sturm et al., 2015). However, in consideration of the natural variability of snow (Bormann et al., 2018; Cohen, 1994; Cohen 2018; Mudryk et al., 2017; Mudryk et al., 2020; Sturm et al., 2017) and mounting uncertainty in spatiotemporal distribution due to climate change (Brown and Mote, 2009; Pulliainen et al., 2020), it becomes evermore critical to improve our estimates of snow accumulation. Other platforms have been used for snow remote sensing; however, optical methods are limited by darkness, cloud cover, and forest canopy (Nolin,

2010) while airborne LiDAR is cost prohibitive at large scales, providing only snow depth information on a basin to regional scale. Microwave remote sensing overcomes many of these limitations (Kelly, 2009) and is also sensitive to snowpack volume (Hall et al., 2005) which is important for retrievals of snow water equivalent (SWE). Although passive microwave measurements have a more established history in space-borne snow observation, originating with the launch of the Electrically Scanning Microwave Radiometer in 1972 (Rango et al., 1979), active microwave, or radar measurements have the advantage of finer spatial resolution (Shi et al., 2016) which is important given the spatial variability characteristic of the snow accumulation environment. However, interpretation remains a challenge for both approaches. This is in part, due to the complexity of the natural snow accumulation environment which may include soil, vegetation, and ice, along with snow. Natural spatiotemporal variability of the physical properties of snow, such as depth, density, microstructure, and moisture, add to this complexity. This can lead to the problem of equifinality in SWE retrievals, where multiple combinations of parameter values can produce the same outcome. Therefore, understanding the variability and developing constraints on parameters is critical to characterizing uncertainty in SWE retrievals, and is the driver of this thesis. Analysis of the radar response at the local to regional scale provides insights into controlling environmental processes. Therefore, this thesis focuses on significant factors that control the radar responses from seasonal snow in common multiple wintertime landscapes. While these factors may be manifest at a local to regional scale, they are governed by underlying physical processes that have far wider applicability.

1.2 Objectives

The overall aim of this thesis was to develop knowledge of constraints on radar based SWE retrievals related to terrestrial snow environments. This includes consideration of vegetation (buried or aerial), and subnivean soil state that impact retrieval accuracy. This work is guided by three important considerations: the role of stratigraphy, the influence of vegetation on retrieval accuracy, and the effects of background scattering. To address this aim, four specific objectives were set out:

1) Demonstrate how physical processes driving the snow accumulation environment manifest regional outcomes in terms of parameterization and constraints.
2) Quantify effects of ice lenses, agricultural vegetation, and background scattering on retrievals.
3) Develop a means to constrain wind slab thickness in an arctic tundra snowpack in a retrieval context.
4) Improve characterization of coniferous forest in a retrieval context.

Wet and melting snow will be excluded from this thesis since they render the snow opaque at the frequencies under consideration and are of concern primarily during the melt season. Perennial snow on glaciers and ice sheets and snow on sea, lake, and river ice will also be excluded.

1.3 Structure

This thesis follows the manuscript format and comprises nine chapters in order to provide sufficient background information and address the stated objectives. Published chapters have retained their original content which may result in repetition of foundational material throughout the document.

The first chapter provides an introduction to the thesis. This includes the motivation, aim, and objectives. The intention of chapter is to illustrate impetus for the work herein.

The second chapter provides a review of the characteristics and variability of terrestrial snow accumulation critical to radar remote sensing. This includes snow depth, snow density, SWE, metamorphosis, permittivity, and stratigraphy. A description of current measurement techniques and uncertainty is provided.

The third chapter introduces the radar power response and includes description of backscattered power, absorption, and scattering, adapted to the snow accumulation environment. This chapter also provides an introduction to a popular radiative transfer model, used in Chapter 6 to explore the radar response of snow and backscatter sensitivity to measurable snowpack and soil parameters.

The fourth chapter describes the polarimetric response in terms of vegetation and snowpack. The polarimetric description of a wave is followed by a review of statistics useful in characterization of the polarimetric response. Finally, the Freeman-Durden three component decomposition is introduced, which was implemented in Chapters 7 and 8.

The fifth chapter introduces the UWScat instrument which provided all radar measurements used in this thesis. An introduction to the system and deployment methods is followed by a description of post-processing methods and error estimation. The chapter concludes with a summary of deployment.

The sixth chapter address the first and second objectives and provides insight into radar based SWE retrievals at mid-latitude agricultural sites, including the influence of vegetation, ice lenses and background scattering effects. This chapter has been published in the peer reviewed journal *Canadian Journal of Remote Sensing*:

Thompson, A., & Kelly, R. (2021). Considerations for Ku-band radar retrieval of snow water equivalent for mid-latitude Ontario agricultural sites. *Canadian Journal of Remote Sensing*, 47(1), 119-142. doi: 10.1080/07038992.2021.1898938.

The seventh chapter addresses the third objective and introduces a means to constrain wind slab thickness in a tundra snowpack. This chapter has been published in *Remote Sensing Letters*:

Thompson, A., & Kelly, R. (2021). Estimating wind slab thickness in a Tundra snowpack using Ku-band scatterometer observations Ku-band scatterometer observations. *Remote Sensing Letters*, *12*(11), 1123–1135. doi: 10.1080/2150704X.2021.1961174.

The eighth chapter addresses the final objective and improves characterization of coniferous forest in a retrieval context. This chapter has been published in the peer reviewed journal *Remote Sensing*:

Thompson, A. & Kelly, R. (2019). Observations of a coniferous forest at 9.6 and 17.2 GHz: Implications for SWE retrievals. *Remote Sensing*, 11(6). doi: 10.3390/rs11010006.

The final chapter summarizes the contributions of the thesis and its limitations. Suggestions for future work arising from this thesis are also provided.

Chapter 2

Characteristics and variability of terrestrial snow

Many of the physical properties used to characterize a snowpack are of interest to the remote sensing community. Such characteristics include snow depth, snow density, SWE, grain size and microstructure (and metamorphosis), and permittivity, whether aggregated into a bulk property or defined within a given stratigraphy. Understanding these characteristics and their variability is important to interpretation of the microwave response. It is also important to understand uncertainty in field measurements of snow since these may be used to parameterize SWE retrievals or to assess their accuracy and therefore could introduce apparent error.

2.1 Snow depth

Snow depth is among the most sought snowpack characteristics and among the most frequently and easily measured (Fassnacht et al., 2018; Sturm et al., 2010). It defines roughly, and in part, the path length microwave energy must transit within a snowpack. The primary drivers of variability in snow depth include precipitation and windspeed, while topography, elevation, and surface roughness, which can be linked to vegetation, exert considerable influence (Fassnacht et. al., 2018; Liston and Sturm, 1998; Pomeroy and Gray, 1995; Pomeroy et al., 1997), however the magnitude of the influence of each factor is site specific (Liston, 2004). In open areas, common in tundra and prairie landscapes, consistency is observed in annual patterns of snow depth driven by precipitation, windspeed, and invariant topographic features with patterns of wind redistribution occurring on a scale of up to hundreds of metres (Fassnacht et al., 2018; Liston, 2004) where wind-blown snow collects on lee hillsides and in valleys, gullies, and depressions (Pomeroy et al., 1997). Periods of strong, sustained wind can drive mass loss of wind-blown snow by up to 50% during saltation and suspension of snow particles (Liston, 2004). This can limit the amount of snow available for accumulation. At short distance scales, up to one hundred metres, snow depth is correlated with vegetation (Deems et al., 2006; Liston, 2004) which enhances surface roughness, catching blowing snow in quantities proportional to vegetation height (Pomeroy and Gray, 1995; Pomeroy et al., 1993; Sturm and Douglas, 2005); in arctic tundra, the deepest snow is often associated with the tallest shrubs (Sturm at al., 2001). Simulations by Liston et al. (2002) noted an increase in average snow depth of 14% in a tundra domain when the basin was redefined as shrub tundra. Drift features in tundra landscapes can hold disproportionally large amounts of SWE relative to their areal extents (Sturm et al., 2001; Pomeroy et al., 1997) but are limited in growth by available precipitation (Sturm et al., 2001). In regions with more dense forest canopy, snow distribution is controlled by the structure and density of the canopy and so may vary seasonally with highest-density forest featuring reduced snow accumulation (Rice and Bales, 2010). In alpine regions, elevation, and orographic effects, including precipitation, local wind fields, atmospheric stability, and moisture distributions

control snow depth at kilometre scales, often producing similar snow distribution patterns each year where wind direction is consistent, although depth may vary (Deems et al., 2006; Liston, 2004).

The simplest field measurement of snow depth can be obtained with a ruler, but such measurements are subject to operator bias in terms of making the measurement and siting, which refers to choosing measurement sites that emphasize depth or shallowness (Goodison et al., 1981). The magnaprobe, a GPS-enabled automated snow depth probe, is still subject to operator bias, but allows for quicker snow depth measurement with greater accuracy and precision for snow depths less than 120 cm, enabling rapid transect measurement coupled with GPS locations. Snow depth accuracy of the device is better than 5 cm (improving over impenetrable subnivean surfaces) with most measurement error resulting from over-probing of soft substrate and off-vertical positioning of the probe during measurement, while positional accuracy is ± 2.5 m (Sturm and Holmgren, 2018). Stationary measurements of snow depth can be made with ultrasonic instruments which can measure snow depth within ± 1 cm when compared to manual observations but are sensitive to mounting and may generate error in low density snow (Ryan et al., 2008).

2.2 Snow density

Snow density is defined as the mass of snow contained in an arbitrary reference volume (Kinar and Pomeroy, 2015) and is important for remote sensing of SWE and parameterization of snow models (Bormann et al., 2013). Snow density varies both spatially and temporally (Bormann et al., 2013) but it varies conservatively compared to snow depth (Brown, 2000; Sturm et al., 2010). Density of new snow ranges from 10 kg/m^3 to 350 kg/m^3 (Judson and Doesken, 2000) while maximum density of snow can approach 600 kg/m^3 beyond which it transitions to firn (Paterson, 1981; Pomeroy and Gray, 1995). Variability in inter-annual snow density is driven primarily by total winter precipitation, followed by mean air temperature (Bormann et al, 2013). Intra-annual spatial variability of density can be caused by elevation and latitude (through linkage to air temperature), sustained wind speed, melt-refreeze events, metamorphosis, and water content (Bormann et al., 2013; Colbeck, 1982; Marshall et al., 1999; Sturm et al. 2010). Temporal variation in compaction behaviour of snow is controlled primarily by snow grain characteristics which are strongly affected by local weather and thermodynamic conditions contributing to inter-annual similarity at a particular location and within particular snow-climate classes (Sturm and Holmgren, 1998).

Jonas et al. (2009) also highlighted regional influence on density in the Swiss Alps. In a study of three snow-climate classes, Sturm and Holmgen (1998) identified stronger inter-annual consistency in Maritime and Taiga snow compaction behaviour than for Tundra snow which exhibited variation in compaction behaviour attributed to differences in wind exposure between exposed and sheltered Tundra sites; This provides compelling evidence that wind can have a strong control on snow densification. Wetness also has a profound effect on snow density whereby densification rates on first wetting can reach three orders of magnitude greater than for dry snow

(Marshall et al., 1999). Vegetation may create local variation in density by introducing gaps in the snowpack and by modifying the thermal regime thus enhancing kinetic growth of snow grains (Marbouty, 1980; refer to Section 2.4 of this thesis).

Since snow density is a critical component in the determination of SWE, it is important to also consider uncertainty in field measurements since these may be used to assess the accuracy of SWE retrieval algorithms. Field measurements of snow density are typically made with rectangular, wedge, or cylindrical density cutters in snow pits following Fierz et al. (2009). Experiments have concluded that larger box-style and cylindrical cutters (200 cm^3 and 500 cm^3, respectively) produce less error than other types (± 2% and -2% to +1% under sampling and weight errors, respectively) in layers between 10 cm and 30 cm thick, while all cutter styles measured within 11% of the true value (Conger and McClung, 2009); Proksch et al. (2016) found wedge cutters produced the largest bias however this could be minimized if the cutter could be inserted vertically (Conger and McClung, 2009). Carroll (1977) observed no difference between cutter styles but suggested sampling difficulty particularly in new snow and depth hoar may contribute error dependent on operator experience, resulting in measurement errors in depth hoar and new snow of up to 6% and 4% respectively. The primary source of uncertainty when using density cutters arises from compaction of snow and sample loss (Proksch et al., 2016). Undersampling may occur when sampling amidst vegetation which can become trapped in the box cutter, displacing snow (eg. Thompson and Kelly, 2021a).

Micro-computed tomography (μCT) can produce mean snowpack density with a 3% error at millimetre resolution but provides equivalent performance (within 9%) to density cutters if the cm-resolution of these instruments is sufficient (Proksch et al., 2016); the requisite equipment is not portable and is prohibitively expensive so μCT will not be discussed at length since it cannot be readily used to make field measurements in most cases.

The snow micropenetrometer (SMP) is a high-precision alternative to estimate snow density. Resistive force is measured by a transducer on the top of a rod which penetrates the snowpack at a constant velocity (adjustable, 6-20 mm s^{-1}) with a force resolution of 0.01 N and millimetre spatial resolution (Schneebeli and Johnson, 1998; Schneebeli et al., 1999). Combining SMP force measurements and coincident μCT snow density measurements, this method relies on regression analysis relating penetrative force and distance between two rupturing elements to snow density measured by μCT to provide a vertical density profile with an error not exceeding 11%, however, it depends on accurate, local density measurements for optimal results (Proksch et al., 2015).

Modeling has also been used to estimate density based on climate variables and location with varied success, heavily regionalized and dependent on model parameterization (Jonas et al., 2009; Sturm et al., 2010; Sturm and Holmgren, 1998); best results were achieved for high-latitude taiga, tundra, and alpine sites (Bormann et al., 2013). The snow fork offers another means to

estimate density by leveraging its relationship with measured permittivity (Sihvola and Tiuri, 1986; Tiuri, 1984) producing error of around 5% (Kinar and Pomeroy, 2015).

2.3 SWE

SWE characterizes the hydrological significance of snow cover (Jonas et al., 2009). It is an indicator of the amount of water stored in a snowpack and is therefore the most important metric for understanding global snow water trends (Sturm et al., 2010). As the product of snow depth and vertically integrated snow density, SWE varies with these quantities but the derived value, and the uncertainty, is most closely linked with snow depth given the conservative variability of snow density (Derksen et al., 2009; Sturm et al., 2010) and can therefore vary considerably even within a sample site (Jonas et al., 2009); it varies in response to environmental conditions, region, and elevation (Brown and Mote, 2009). SWE is most commonly measured in the field with a snow tube or derived from snow pit measurements of depth and vertically integrated density measured with a density cutter (aggregating the measurement error). The most common cause of error in snow tube measurements is loss of snow as the tube is extracted (Sturm et al., 2010) although, in a review of earlier field work, Goodison et al. (1981) noted a frequent positive bias with an error of up to 18% attributed to additional snow being forced into the snow tube. Uncertainty in SWE derived from snow pit measurements is aggregated from the depth and density measurements. Measurements using density cutters were found to be more reliable and accurate than those made with snow tubes which resulted in a negative bias of 7% on average when compared to layer-integrated box cutter measurements (Sturm et al. 2010). Snow pillows are the standard method for automatic, stationary, ground based SWE measurement (Dozier et al., 2016). Snow pillow error predominately comprises overestimation with errors exceeding 40% in some cases, but corrections can be applied based on snowpack conditions and air temperature (Johnson and Marks, 2004). Gamma radiation sensors provide another stationary alternative for SWE measurement with a nominal accuracy of ±15 mm SWE from 0 to 300 mm SWE and 15 % for SWE greater than 300 mm, however errors of up to 35% could occur during spring melt or if the soil moisture calibration is completed improperly (Smith et al., 2017).

2.4 Snow grain characterization and metamorphosis

A snowpack is composed of grains of many different shapes and sizes (Sturm and Benson, 1997) that can be described in terms of grain size and microstructure. Grain size has been measured historically as the maximum extent of a grain (D_{max}) and reported as the average of several such measurements of representative grains in a snow layer (Arons and Colbeck, 1995; Fierz et al., 2009). More recently, the term microstructure denotes a more comprehensive description of a snow sample which accounts for the structure, shape, and size characteristics at the grain scale as well as the unique geometric configuration of the air and ice matrix (Arons and Colbeck, 1995; Fierz et al.,

2009). Microstructure is often reported in terms of correlation length (p_c) and exponential correlation length (p_{ex}) and is commonly used as an input in radiative transfer modeling. The former provides a statistical description of the autocorrelation of snow structural variation in a spatial dimension (Lemmetyinen et al., 2018; Mätzler, 2002). The latter fits the correlation function to an exponential form thereby defining structural variation at a greater length scale, characterizing the correlation function as a whole (Mätzler, 2002; Proksch 2015). Mätzler (2002) suggested an empirical relationship between measured *pc* and p_{ex} where $p_{ex} = 0.75p_c$ however when used in radiative transfer models such as MEMLS, the scaling factor (Φ=0.75) may vary for different models, field measurements and dominant metamorphic snow processes, and is typically optimized to account for error in model physics and parameterization (Brucker et al., 2011; King et al., 2018; Lemmetyinen et al. 2018; Montpetit et al., 2013; Sandells et al., 2017). Microstructure is also commonly described by the specific surface area (SSA) which is the ratio of surface area to volume of a snow grain, or alternatively, it may be expressed in terms of mass instead of volume (Gallet et al., 2009; Proksch et al., 2015); conversions exist between terms (eg. Mätzler, 2002). Other grain metrics exist (eg. optical grain size: Grenfell and Warren, 1999) but will not be discussed here.

Existing at or near its melting temperature, ice is thermally unstable, therefore, dry snow, which is a granular aggregate of ice and water vapor, is thermally unstable and constantly undergoes metamorphosis (Arons and Colbeck, 1995; Colbeck, 1982; Colbeck, 1983; Colbeck, 1987). While grain growth and vapour transport form the basis of dry snow metamorphosis (Sturm and Benson, 1997) there are two distinct types that can occur termed equilibrium and kinetic form (Colbeck, 1980; Colbeck, 1982; Colbeck 1983) which can be distinguished by their growth rate, separated by a critical temperature gradient threshold (Colbeck, 1986). In both cases transfer of latent heat occurs across the snow grains given their greater thermal conductivity compared to the air in pore spaces which can enhance temperature gradients and vapor transport (Sturm et al., 1997).

The equilibrium form of metamorphosis occurs under isothermal conditions, in the absence of a of significant temperature gradient and produces the rounded and sintered grains. Early-stage equilibrium form is shown in Figure 2.1. It is characterized by phase equilibrium thermodynamics and is considered a destructive process. Larger grains grow at the expense of smaller ones since vapour pressure is greater over surfaces with smaller radii of curvature which sublimate allowing mass transfer to larger grains by condensation thereby driving the system towards equilibrium (Colbeck, 1982). Kelvin's law is used to describe vapor diffusion in equilibrium metamorphosis where negligible temperature gradients exist, however the effect is weak in natural snow cover where a temperature gradient almost always exists (Colbeck, 1983); the equilibrium form of metamorphosis will persist until the temperature gradient exceeds approximately 10°C/m (Arons and Colbeck, 1995). In a natural snowpack, isothermal conditions, and negligible temperature gradients (<1°C/m) occur primarily in fresh snow in upper layers of the snowpack where fine radii of curvature ($<10^{-3}$mm) drive initial equilibrium metamorphism (Colbeck, 1980). The equilibrium

form of metamorphosis progresses very slowly (Colbeck, 1980) and densifies over time (Sturm and Homgren, 1998), developing a settled, cohesive structure (Armstrong, 1980). Equilibrium metamorphosis will occur in any dry snowpack where the temperature gradient is less than approximately 10°C/m, which occurs predominately in regions with warmer winters such as those identified as maritime, prairie snow climate classes (Sturm et al., 1995).

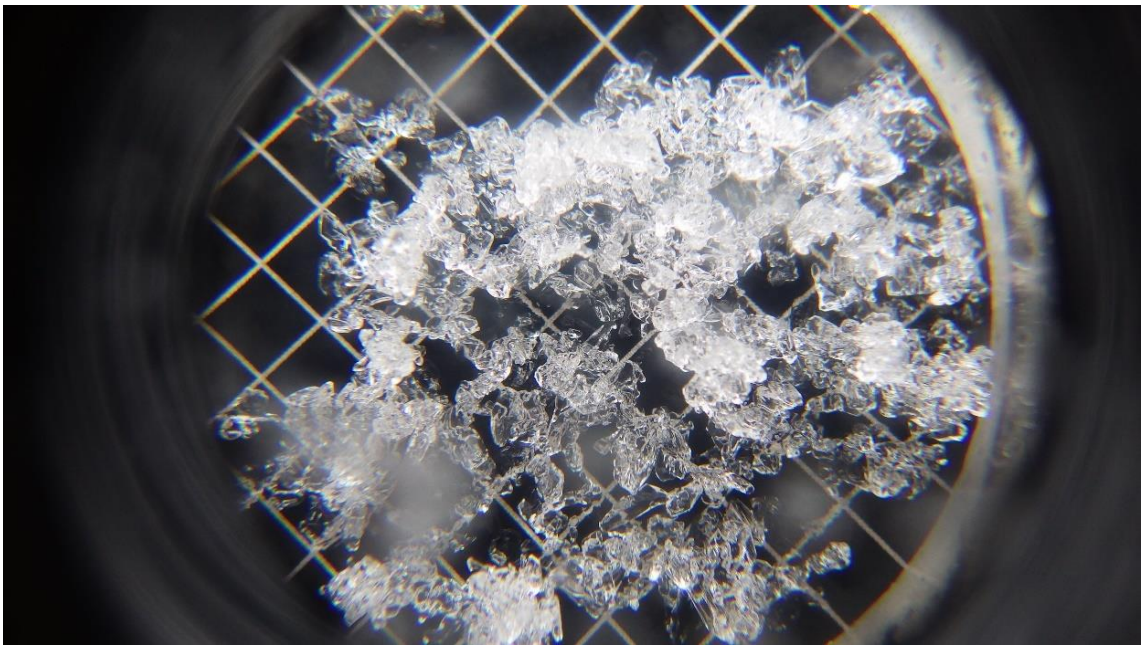

Figure 2-1. Early-stage equilibrium growth form snow grains in Trail Valley Creek during April 2016 photographed on 2 mm grid.

Kinetic metamorphosis occurs when dry snow is exposed to a minimum temperature gradient exceeding approximately 10°C/m and where water vapour is available (Arons and Colbeck, 1995; Colbeck, 1983). Kinetic metamorphism develops faceted grains, and ultimately large depth hoar, as the temperature gradient drives a vapor pressure gradient and associated vapor flux in the pore space, inducing recrystallization (Colbeck, 1982); depth hoar is presented in Figure 2.2. An upward transfer of mass and latent heat occurs as vapor condenses on the bottom of each grain while sublimation occurs simultaneously from the top (Colbeck, 1983); rate inequality results in grain growth or loss (Sturm and Benson, 1997). Yosida (1955) described this process as a hand-to-hand transfer of water vapor molecules which was later affirmed using time-lapse μCT observations by Pinzer et al. (2012) who also determined that kinetic growth could result in a daily mass turnover rate of up to 60% and a typical grain residency time of two to three days. The rate of metamorphism increases with larger temperature gradients and vapor fluxes, particularly lower in the snowpack (Colbeck, 1982). A vertical structure develops, and grains oriented vertically experience preferential growth compared to grains with alternate orientations (Adams and Miller, 2003; Miller and Adams, 2009), however once the temperature gradients have relaxed the grains begin to round as they move towards an equilibrium state (Colbeck, 1986). Densification occurs

less with kinetic growth form than with the equilibrium form (Armstrong, 1980; Pinzer et al., 2012; Sturm and Holmgren, 1998) as the nature of its form inhibits settlement (Armstrong, 1980). Depth hoar can range in density from around150 kg/m^3 to around 250 kg/m^3 (Armstrong, 1980; Benson and Sturm, 1993). Given the requirement of a large temperature gradient, kinetic metamorphism is most often found where sustained periods of extreme cold occur such as in regions identified as tundra, taiga, and the alpine snow climate class, however it can be found anywhere the critical temperature gradient threshold has been exceeded for sufficient duration (Sturm et al., 1995). Ice lenses may restrict vertical vapor diffusion (Rutter et al., 2019) and depth hoar growth may be enhanced beneath such impermeable layers, which also includes high-density wind slab, since restrictions in upward vapour flux result in elevated levels of supersaturation (Colbeck, 1991). Shrub vegetation may influence both magnitude and distribution of kinetic growth in tundra environments resulting in thickness of depth hoar layers reaching shrub height (Domine et al., 2016; Domine et al., 2015; Liston et al., 2002; Sturm et al., 2001). Furthermore, gaps and low-density snow within the network of shrub branches facilitate growth of depth hoar (Marbouty, 1980). Larger depth hoar crystals have been associated with shrubs in tundra environments according to Domine et al. (2016) who attributed favorable growth of depth hoar to enhanced early-season accumulation of low-density snow in shrubs which maintains soil warmth and the critical temperature gradient required for kinetic growth over a longer duration compared to snow without shrubs.

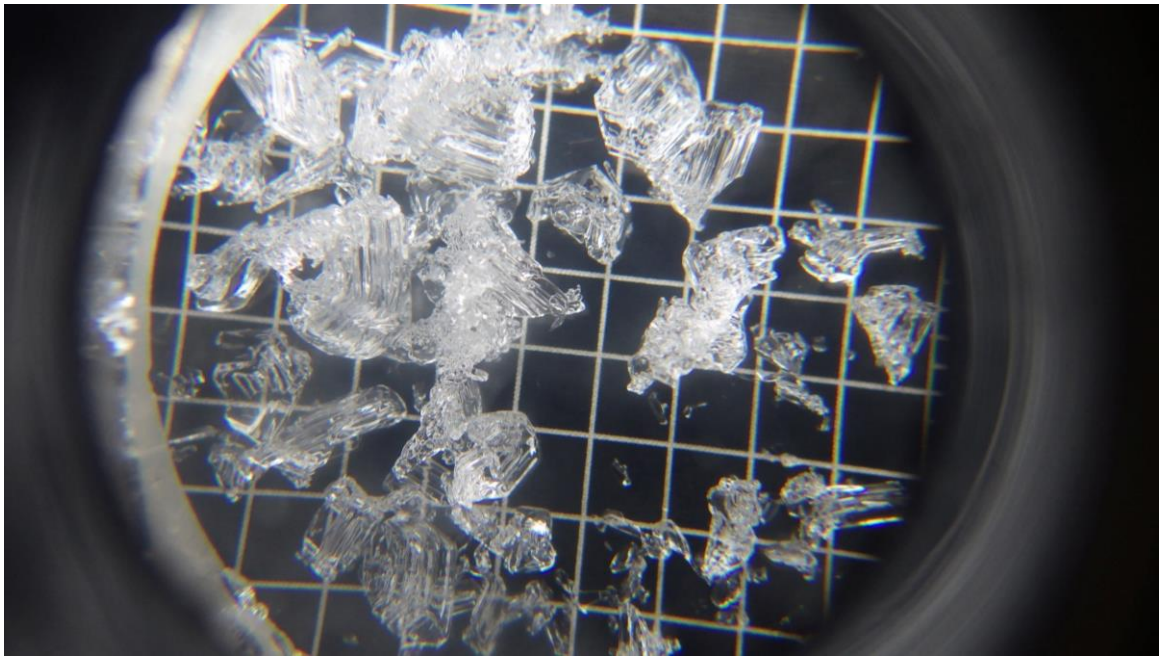

Figure 2-2. Depth hoar resulting from kinetic growth in Trail Valley Creek during April 2016 photographed on 2 mm grid.

In a natural snowpack it is common to encounter snow grains which are at varying stages of metamorphism and exhibit traits of both equilibrium form and kinetic form, appearing

simultaneously rounded and faceted (Colbeck, 1982). These may result from intermediate growth rates, transitioning from equilibrium form to kinetic form, or from kinetic form to equilibrium form (Colbeck, 1986). The processes governing this form are identical to those discussed above.

At the snowpack surface, sustained periods of high windspeed can lead to the development of a wind slab layer. This is the result of wind-drive fractured grain fragments packing into high-density layers (Colbeck, 1982). Snow density in wind slab can reach 500 kg/m^3 (Benson and Sturm, 1993) because the grain fragments round and sinter quickly, and because of their relatively large bonds (Colbeck, 1991). These dense, high-strength layers can be found in open areas exposed to sufficient wind and are a hallmark of the tundra snow climate class (Sturm et al., 1995).

Warming temperatures over the winter season and conditions during the shoulder seasons can lead to melt-refreeze events and rain-on-snow events. These are common in lower latitude regions, but they are predicted to occur more frequently in the north associated with increasing Artic winter temperatures (Derksen et al., 2009; Liston and Hiemstra, 2011; Overland et al., 2017).
When even small amounts of water are introduced at the surface of the snowpack grains round and grow quickly while polycrystalline clusters form (Colbeck, 1982). A layer of increased strength and density develops as the water infiltrates and refreezes at, or beneath the surface or melt location (Colbeck, 1982; Colbeck, 1991). Ice lenses may form, typically at layer horizons where water is retained by capillarity of the finer-grained layer. Upon refreezing, grains lose their distinctive rounded shape, replaced with an amorphous character shown in Figure 2.3 (Colbeck, 1986). During rain-on-snow events, supercooled rainwater refreezes on the snow surface to form a smooth impermeable ice layer (Colbeck, 1982).

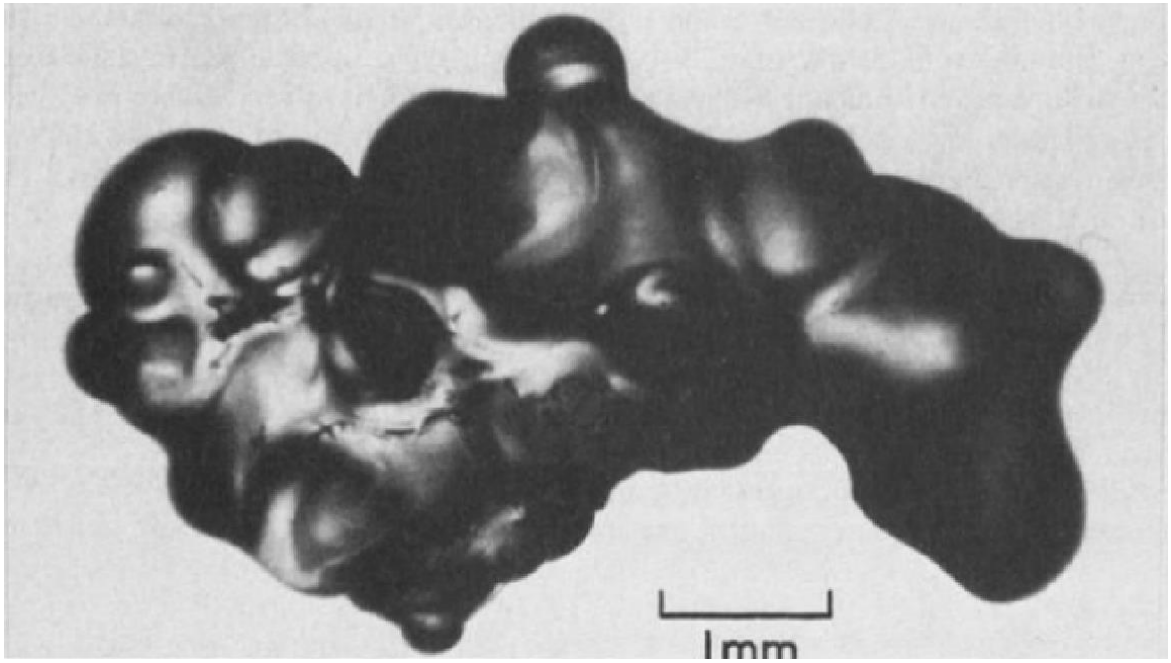

Figure 2-3. Polycrystalline melt-refreeze grain from Colbeck (1986).

Measurement of D_{max} is generally simpler to accomplish in the field than microstructure measurement as it requires only a gridded grain card and a loupe. However, such measurements ignore the shape and orientation of the snow grains and are prone to bias and subjectivity (Aoki et al., 2000; Durand et al., 2008; Mätzler, 2002). Use of D_{max} may also lead to overestimations for complex crystals like new snow and depth hoar (Mätzler, 2002). Nonetheless, given the robust nature of the equipment, the simplicity of grain size measurements, and the catalogue of historical grain size measurements, they are often still incorporated in modern studies. Empirical relationships have been developed in order to estimate correlation length (p_c) from grain size such as the model given in (2.1) and used in Chapter 6, derived by Royer et al. (2017). Such a model may be of limited applicability beyond the region for which it was developed (Royer et al., 2017), and therefore such conversion should be used with caution since it may introduce more uncertainty than the measurements of grain size (Durand et al., 2008).

$$p_c = 0.1069 D_{max} \tag{2.1}$$

Snow grain microstructure can be estimated from field measurements with great accuracy and repeatability from infrared reflectance. Equipment such as the Dual Frequency Integrating Sphere for snow SSA measurement (DUFISSS) and Infrared Integrating Sphere (IRIS) measures hemispherical infrared reflectance of snow samples (Gallet et al., 2009; Montpetit et al., 2012) from which microstructure parameters can be derived following Kokhanovsky and Zege (2004) since most variation in directional reflectance can be explained by variations in SSA (shape effects cancel out in natural snow) (Domine et al., 2006; Montpetit et al., 2012; Picard et al., 2009). Accuracy of SSA estimates is better than 12% providing an appropriate calibration curve has been generated and snow samples have been prepared properly (Gallet et al., 2009; Montpetit et al., 2012; Proksch et al., 2015). High-quality estimates of microstructure can be obtained from the SMP as well with regression analysis relating penetrative force and distance between two rupturing elements to correlation length measured by μCT to provide microstructure estimates with errors of 23.1% and 16.4% for SSA and correlation length, respectively (Proksch et al., 2015). As with SMP estimates of density, this method relies on high-quality local measurements to generate the regression coefficients.

High-accuracy measurements of microstructure can also be made by μCT since it allows full three-dimensional reconstruction and statistical analysis of the microstructure thus providing an accurate baseline for comparison with other methods (Proksch et al., 2015). This method will not be discussed further for the reasons outlined in Section 2.2.

2.5 Permittivity

Complex relative permittivity (ε_r) is a dielectric property which describes the electrical storage of a dielectric medium when exposed to an electrical field, relative to a vacuum. Given in (2.2), it is a complex term comprised of a real component (ε') which governs the electrical storage and the ability of a medium to be polarized and an imaginary component (ε") which defines the loss or dissipation of energy in the medium.

$$\varepsilon_r = \varepsilon' - j\varepsilon'' \tag{2.2}$$

Discussion of permittivity is warranted since the interactions of microwave in snow are governed in part by its dielectric properties (Stiles and Ulaby, 1981). In the microwave frequency range, the real portion of permittivity of dry snow, ε'_{ds}, is primarily dependent on snow density while independent of frequency (Cumming, 1952). Since the relaxation frequency of ice is in the kilohertz range, dry snow doesn't exhibit dispersion above 100 KHz, therefore an apparent lack of sensitivity of ε'_{ds} to frequency is observed in the gigahertz microwave range (Stiles and Ulaby, 1981). However, ε''_{ds} exhibits both temperature and frequency dependence (Mätzler, 1996; Stiles and Ulaby, 1981).

Given that dry snow is an ice matrix with an air background, ε'_{ds} is a function of its constituents and can be estimated through mixing formulas and empirical relationships (eg. Mätzler, 1996; Polder & van Santen, 1946; Tinga, 1973; Tiuri, 1984). Using (2.3) and (2.4) (Mätzler, 1996; Wiesmann and Mätzler, 1999), ε'_{ds} can be estimated in terms of the density of dry snow (ρ_{ds}) which accounts for changes in volume fraction of ice. In (2.4), $\varepsilon_h = 1$ and is the permittivity of the host medium (ie. air) while ε_s is the permittivity of ellipsoid inclusions (ie. ice) in the host medium, and *v* is the volume fraction of the snowpack. An assumption of such mixing models is that losses from absorption far exceed those from scattering which may be violated in snow when wavelength becomes comparable in size to scatterers (refer to Section 3.2).

$$\varepsilon'_{ds} = 1 + 1.5995\rho_{ds} + 1.861\rho_{ds}^3, \quad \rho_{ds} < 400\ g/cm^3 \tag{2.3}$$

$$\varepsilon'_{ds} = ((1-v)\varepsilon_h + v\varepsilon_s)^3, \quad \rho_{ds} \geq 400\ kg/m^3 \tag{2.4}$$

Following Tiuri et al. (1984), ε''_{ds} can be estimated from snow density and ε''_{ice} in (2.5), however it can be neglected in dry snow at microwave frequencies because it is so small (Hallikainen et al., 1986; King, 2014). An alternative formulation is provided in Wiesmann and Mätzler (1999). Estimation of ε''_{ice} can be obtained from Wiesmann et al. (1998). Equations (2.3), (2.4), and (2.5) were implemented in the Microwave Emission Model of Layered Snowpacks (MEMLS; Mätzler and Wiesmann, 1999; Wiesmann and Mätzler, 1999).

$$\varepsilon_{ds}^{"} = \varepsilon_{ice}^{"}(0.52\rho_{ds} + 0.62\rho_{ds}^{2}) \quad (2.5)$$

The natural range of dry snow density (approximately 200 kg/m^3 to 500 kg/m^3) corresponds to a range of ε_{ds}' between 1.4 and 2 (Ulaby et al., 1986a) while ε_{ice}' is approximately 3.17 (variation of this value in the literature may be related to slight temperature dependence) with negligible frequency response over the microwave range (Mätzler and Wegmüller, 1987). The loss tangent of ice is very small with $\varepsilon_{ice}^{"} \approx 10^{-3}$ at 1 GHz (Hallikainen et al., 1986). Water has much greater $\varepsilon_r$than snow and has a relaxation frequency around 9 GHz at 0°C (Hallikainen et al., 1986; Ulaby et al., 1986b; Ulaby et al., 1981) which enhances energy dissipation in this frequency range with substantial implications for microwave remote sensing and explains why observations of wet snow have been excluded from this thesis.

Since ε_r of dry snow varies primarily with snow density, in a natural snow accumulation environment it can be expected to vary spatially and temporally in accordance with the discriminants of snow climate class in Sturm et al. (1995) and seasonal weather patterns which drive snowpack thermodynamics.

Field measurements of ε_r of snow can be made using a snow fork with accuracy of 1.5% to 2.09% for snow densites of 200 kg/m^3 to 500 kg/m^3 (Sihvola and Tiuri, 1986). The Denoth meter provides another measurement option with an error of about 2% (Denoth, 1994). Techel and Pielmeier (2011) noted measurements made with the snow fork were consistently higher than those with the Denoth meter but were well correlated.

2.6 Stratigraphy

Stratigraphy describes the layered nature of a snowpack which is generated by wind, intermittent precipitation, and continuous metamorphism of snow and controlled by physical properties of the environment including vegetation and topography (Colbeck, 1991; Fierz et al., 2009; Sturm, 1991; Sturm and Benson, 1997; Sturm and Benson, 2004). Each layer is a tabular body of snow with observable boundaries and characteristics distinct from adjacent layers (Sturm and Benson, 2004). Knowledge of stratigraphy is important because variation in the physical properties of each layer cannot be resolved from averaged or bulk snowpack properties, and the sequence of layers can impart dielectric discontinuities with implications for the microwave response (Colbeck, 1991). Bernier (1987) suggested uncertainty in the understanding of snowpack structure would impede microwave estimation of SWE and indeed, three decades on, it still presents a formidable challenge in terms of both microwave interpretation and SWE retrieval (eg. King et al., 2018; Montpetit et al., 2013; Thompson and Kelly, 2021).

Heterogeneity of snowpack structure across a landscape is common (Derksen et al., 2009; Mätzler, 1996a; Sturm and Benson, 2004), however the scale of heterogeneity may be constrained.

For example, maximum lateral heterogeneity in the arctic tundra snowpack was observed at scales up to 100 m, associated with wind and its interaction with topography and vegetation, after which point synoptic-scale weather events controlled diminishing heterogeneity (Sturm and Benson, 2004). Conversely, shrubs and trees amplified local scale heterogeneity by controlling snow depth, stratigraphy, and metamorphism (Benson, 1972; Derksen et al., 2009; Kort et al., 2011; Sturm, 1992; Sturm, 2001).

Field observations of stratigraphy are commonly derived from classic snow pit measurements comprising those discussed in Sections 2.1 through 2.5 in either a continuous vertical profile, or from layers distinguished visually by textural characteristics. However, individual snow pits represent only a point measurement and fail to capture variability unless a temporally or spatially distributed series of snow pits is observed (eg. Derksen et al., 2009; King et al., 2018; Sturm and Benson, 2004; Rutter et al., 2019; Thompson et al., 2019). Traditional stratigraphy observations can be complimented with high-resolution force profiles generated from the SMP which can identify fine strata imperceptible with other methods (Proksch et al., 2015). As discussed in Sections 2.2 and 2.4 it can also be used to generate profiles of density and microstructure subject to appropriate calibration. Near-infrared photography of snow pit faces provides another means to observe structural variation by leveraging reflectance of ice in the near-infrared portion of the spectrum (Matzl and Schneebeli, 2006). Marshall et al. (2004; 2007) demonstrated the use of frequency modulated continuous wave (FMCW) radar for identifying changes in dielectric properties in the snowpack which can be associated with layer boundaries. These non-destructive methods offer high resolution but are subject to interpretation and may not work well for layers with gradual density transitions (Marshall et al., 2007).

Sections 2.1 through 2.6 described the most important snow properties from the perspective of microwave remote sensing of terrestrial snow. An understanding of these properties is fundamental in understanding the microwave response and is also required for successful modeling and retrieval efforts. Measurement techniques were also described which are of critical importance to remote sensing studies of snow because our understanding of the physical processes and their spatiotemporal distribution depend on accurate measurement at the appropriate resolution. Furthermore, accurate measurements of snow properties are critical during ground reference campaigns where the performance of SWE retrieval methods are evaluated against such measurements; error due to poor ground reference measurements could be wrongfully attributed to poor retrieval performance.

Chapter 3
Radar power response from a snow-covered landscape

Microwaves are transverse electromagnetic waves that consist of time-varying electric and magnetic fields that can be described in terms of their frequency, wavelength, amplitude, phase, and polarization (Elachi et al., 1990; Ulaby & Long, 2014). The interaction of microwaves with the snowpack occurs in different ways and in different scattering centres within the snowpack which can be summarized in (3.1) for a given send-receive polarization (*pq*).

$$\sigma_{pq}^{t} = \sigma_{pq}^{as} + \sigma_{pq}^{v} + \sigma_{pq}^{gv} + \sigma_{pq}^{g\prime} \tag{3.1}$$

Conceptually, total backscattering (σ^t) is a summation of the scattering at the air-snow interface (σ^{as}), snow volume scattering (σ^v), scattering from the interaction between the ground and snow volume (σ^{gv}) and scattering from the snow-ground interface ($\sigma^{g'}$) (Rott et al., 2010) which is illustrated in Figure 3.1 in a bistatic arrangement for clarity.

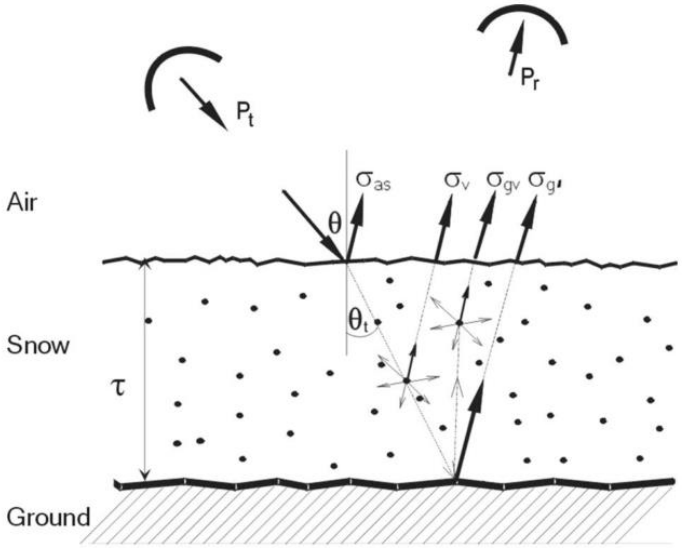

Figure 3-1. Scattering contributions from terrestrial snow. Power transmitted, power received is given by Pr, and Pt. Figure from Rott et al., 2010. Bistatic configuration shown for clarity however monostatic configuration is the default configuration assumed in this paper.

Backscattered power received at the antenna (P_r) following two-way propagation through a snowpack in the manner depicted in Figure 3.1 has been subject to loss described by the extinction coefficient (k_e) which is a summation of both absorption and scattering represented by absorption (k_a) and scattering (k_s) coefficients as in (3.2).

$$k_e = k_a + k_s \tag{3.2}$$

The following subsections will describe backscattered power given in (3.1) and illustrated in Figure 3.1, in terms of (3.2).

3.1 Backscattered power

Measuring backscattered power from a target fundamentally depends on power of the received echo resulting from system and target parameters as determined from the radar equation (Woodhouse, 2006). For monostatic instruments, the power returned to an antenna (P_r) is given by (3.3) which includes both radar system parameters, such as transmitted power (P_t), antenna gain (G), wavelength (λ), and range to target (r_t), and the sole target parameter, radar cross section (σ) (Ulaby & Elachi, 1990; Ulaby et al., 1986a; Woodhouse, 2006).

$$P_r = \frac{P_t G^2 \lambda^2 \sigma}{(4\pi)^3 r_t^4} \tag{3.3}$$

The σ is a function of the incidence angle as well as the physical and dielectric properties of the scattering target (Ulaby et al., 1986a). Given σ is the only variable in the radar equation that is dependent on the target properties (Woodhouse, 2006) it is of crucial importance for understanding snow properties in the radar field-of-view (FOV) so (3.3) is re-expressed in terms of σ. However, snow is a distributed target so σ is normalized by the area resolved on the ground (A) in (3.4), which produces the normalized radar cross section or scattering coefficient, σ° (Ulaby & Elachi, 1990; Ulaby et al., 1986a; Woodhouse, 2006). This critical link between the sensor and the scene within the FOV is usually expressed in units of decibel (dB) on a logarithmic scale allowing easier discrimination of variation among small power estimates (Ulaby & Long, 2014).

$$\sigma^\circ = \frac{\sigma}{A} = \frac{P_r (4\pi)^3 R^4}{A P_t G^2 \lambda^2} \tag{3.4}$$

3.2 Microwave absorption

The dielectric properties of the snowpack have a notable influence on the absorption of microwave energy (and therefore P_r) which can be described by the power absorption coefficient (k_a) given in (3.5).

$$k_a = \frac{4\pi}{\lambda}\left\{\frac{\varepsilon'}{2}\left[\left(1+\left(\frac{\varepsilon''}{\varepsilon'}\right)^2\right)^{1/2}-1\right]\right\}^{1/2} \tag{3.5}$$

From (3.5) it is clear that k_a exhibits a frequency dependence where lower frequencies will have greater penetration. It is also clear that k_a will increase with ε_r which was shown in (2.2) through (2.4) to be dependent on snow density. Therefore, spatial, and temporal variation in snowpack structure, including metamorphosis, settling and compaction, will directly affect attenuation of microwave energy through (3.5). This relationship demonstrates potential for microwave attenuation in high-density tundra wind slab resulting from sustained periods of elevated wind speed and open terrain. Although excluded from this thesis, additional attenuation from snowpack wetness (ie. due to melt or precipitation) could also be described in this manner.

The reciprocal of k_a provides the penetration depth (δ_p), or the depth at which microwave power reaches 1/*e* of the power originally incident at the air-snow interface. Like k_a on which it is based, δ_p is sensitive to variation in density, wetness, and the frequency of incident wavelength. Where δ_p is limited, the ability to retrieve information from the snowpack volume becomes diminished along with the potential utility of microwave SWE retrieval thus explaining the restrictions on microwave remote sensing of wet snow. There are also implications for retrievals in areas with dense wind slab-dominated accumulation. At frequencies in the 10 GHz and 17 GHz range, δ_p is on the order of 10 m and 3 m, respectively (Mätzler, 1987; Rott et al., 1993), however, these estimates assume a homogeneous snowpack with effective values of ε' and ε" and do not account for natural variation in the snowpack.

The quantity k_a only accounts for a portion of microwave extinction from propagating through a snowpack and does not account for microwave scattering. At low frequencies k_e is often approximated by k_a since $k_s \ll k_a$, however above 10 GHz to 15 GHz, the magnitude of k_s may approach k_a especially for grains approaching the scale of incident wavelength (Hallikainen et al., 1986; Stiles & Ulaby, 1981;). Therefore, microwave scattering must not be neglected at higher frequencies.

3.3 Microwave scattering

3.3.1 Surface scattering

Surface scattering can be conceptualized in Figure 3.2 by σ_{as} and $\sigma_{g'}$ and may also occur at layer interfaces within the snowpack, however, given the similarity between ε_{air} and ε_{snow}, σ_{as} is negligible unless the snow is wet (eg. Kendra et al., 1998; Thompson et al., 2019). Microwave behaviour when encountering a surface depends in part on the roughness of the surface relative to λ and

incidence angle. A surface is considered smooth if the standard deviation of surface height (h) is less than Fraunhofer's criteria (3.6) but is considered rough otherwise (Ulaby et al., 1986a).

$$h = {\lambda}/{32cos\theta} \tag{3.6}$$

A quantity of microwave energy incident on a smooth surface at a given incidence angle (θ_i) will reflect in a specular fashion according to the Fresnel reflectivity coefficients for horizontal (R_H) and vertical (R_V) incident polarizations given in (3.7) and (3.8) which describe the proportion of incident energy reflected and transmitted at an interface (Senior and Sarabandi, 1990). Fresnel reflectance at a smooth surface is illustrated in Figure 3.2 for a surface where $\varepsilon_r = 3.0 - j0$. An initial decrease to minimum reflectance at the Brewster angle occurs for R_V followed by exponential growth, which is observed for R_H through the entire range of incidence angles. Energy that is not reflected is transmitted and subject to refraction governed by Snell's law. The air-snow interface and snowpack layer interfaces may be treated as smooth layers in models such as MEMLS (Proksch et al., 2015).

$$R_V = \left(\frac{\varepsilon_r cos\theta_i - \sqrt{\varepsilon_r - sin^2\theta_i}}{\varepsilon_r cos\theta_i + \sqrt{\varepsilon_r - sin^2\theta_i}}\right)^2 \tag{3.7}$$

$$R_H = \left(\frac{cos\theta_i - \sqrt{\varepsilon_r - sin^2\theta_i}}{cos\theta_i + \sqrt{\varepsilon_r - sin^2\theta_i}}\right)^2 \tag{3.8}$$

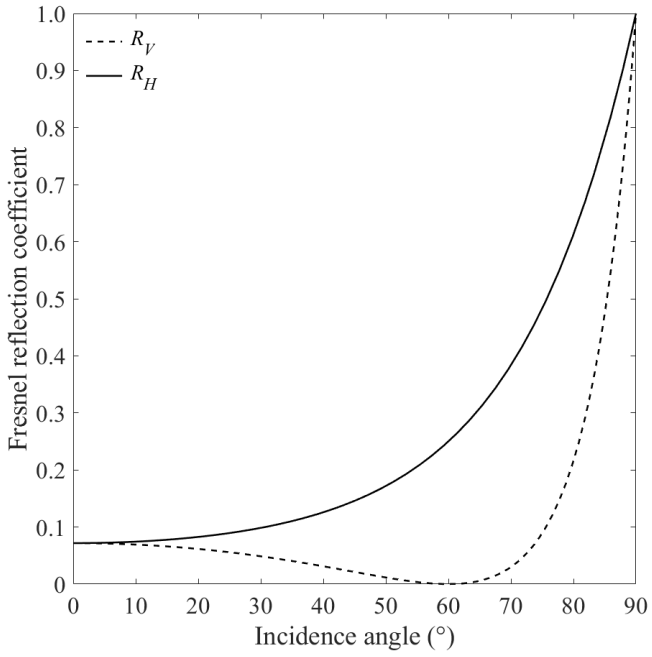

Figure 3-2. Fresnel reflection coefficients for a surface where Er = 3.0 - j0.

Ice lenses within or at the surface of the snowpack may also act as smooth surface scatterers where specular reflection occurs at interfaces with the ice and adjacent snow strata or air (Montpetit et al., 2013; Proksch et al., 2015); this effect may be enhanced for wet surface ice lenses (Thompson et al., 2021). Coherent scattering effects may occur for ice lenses where thickness is less than $\lambda/2$ (Mätzler, 1996b). There is a deficit of radar measurements and coincident field measurements of ice lenses, therefore, more work must be done to understand their influence (Rutter et al., 2019).

When microwaves encounter a rough surface such as the snow-soil interface, scattering becomes more diffuse. Several models have been developed to account for this including the small perturbation model, Kirchoff model, geometric optics model and physical optics model, each used for specific degrees of surface roughness (Ulaby & Long, 2014). Other models include the integral equation family of models (Fung et al., 1992; Fung et al., 2002; Wu & Chen., 2004) and the empirical model by Oh et al. (1992). The semi-empirical Rough Bare Soil model of Wegmüller and Mätzler (1999), used in Chapter 6 and given in (3.9) and (3.10), facilitates estimation of rough soil surface scattering in models such as MEMLS by determining horizontal-polarized (S_H) and vertical-polarized (S_V) reflectivity from a rough soil surface; the quantity $k = 2\pi/\lambda$ represents wavenumber. It remains a popular choice for estimating soil surface reflectivity in microwave modelling (eg. King et al., 2018; Lemmetyinen et al., 2018; Lemmetyinen et al., 2016; Montpetit et al., 2018; Montpetit et al., 2013; Royer et al., 2017; Thompson and Kelly, 2021; Vargel et al., 2020). It is a simple model with few parameters to optimize, bolstering its popularity (Montpetit et al., 2018). Estimating the background scattering is important in microwave modelling of dry snow given δ_p in dry snow conditions (Proksch et al., 2015).

$$S_H = R_H exp\left(-(kh)^{\sqrt{-0.3cos\theta}}\right) \tag{3.9}$$

$$S_V = S_H cos\theta^{0.655} \tag{3.10}$$

Since S_V is derived from S_H and S_H is dependent on R_H which is a function of soil ε_r, reflectivity is in part controlled by soil wetness and temperature especially with respect to freeze and thaw. Frozen soil thus results in decreased reflectivity. It also varies with incidence angle directly and through the association with R_H with larger incidence angles yielding greater reflection. Care may be required in the estimation of background scattering of moist or unfrozen soils to distinguish between organic and mineral soil type (Mathieu et al., 2003) since ε' of mineral soil is generally greater than that of organic soil according to studies on mid-latitude samples (Kim et al., 2000; Roth et al., 2002). This occurs because bound water molecules in organic soil experience restricted rotation as a film over the larger surface area, thus decreasing ε' (Wang and Schmugge, 1980). However, when there is limited moisture, there is little observable difference in ε' between organic and mineral soil (Mathieu et al., 2003). Of particular relevance in shoulder seasons, arctic and subarctic peatlands

may behave differently since they retain liquid water at temperatures down to -5°C according to limited laboratory experiments (Nagare, 2012), however, Kujala et al. (2008) found water in peat samples from the surface of palsas froze between 0° and -0.8°C but noted that properties of peat vary with humification and plant composition. This apparent inconsistency highlights the need for improved understanding of the dielectric properties of frozen peat. Uncertainty in terms of soil condition may be mitigated in SWE retrievals by implementing a soil subtraction scheme (eg. Thompson and Kelly, 2021a), otherwise regional soil models may be required.

3.3.2 Volume scattering

As microwaves are transmitted past the air-snow interface and into the snow volume, they may be subject to volume scattering primarily caused by dielectric discontinuity within the medium (Ulaby et al., 1986a) driven by variation in physical snowpack properties and dependent on path length within the medium and observation frequency. Density variation associated with stratigraphy can enhance coherent and incoherent superposition effects (Mätzler, 1987). Furthermore, vertical, and horizontal variation in snow density can lead to wave phase front distortion contributing to forward scattering due to diffraction and geometrical optics (Mätzler, 1987). Interaction between microwaves and snow grains can often be described by Rayleigh scattering given that the grains, assumed to be spherical, are usually smaller than the incident wavelength; if grain sizes exceed the wavelength, Mie scattering replaces the Rayleigh model (Ulaby & Long, 2014). Another assumption of this model is that spacing of the spheres is random, and large enough that phase correlations and near-field effects can be ignored (Chang et al., 2014; Picard et al., 2013; Tsang et al., 2007), therefore the total cross section is simply the sum of the cross sections within the FOV (Mätzler, 1987). However, this assumption often leads to underestimation of scattering due to phase correlation that occurs when v exceeds about 20% as is often the case with older snow in a natural snowpack (Mätzler, 1987; Picard et al., 2013). An improvement over Rayleigh scattering model in terms of these shortcomings is the Improved Born Approximation (IBA) which accounts for close spacing of snow grains (Mätzler, 1987). The scattering coefficient (k_s) introduced in Mätzler (1998) is given in (3.11) as a function of v, permittivity of ice (ε_i), wave number (k), and polarization angle (Θ_p). The ratio of the mean squared electric fields inside and outside of the grains (K^2) is given in (3.12) where apparent permittivity $\varepsilon_a = {}^1\!/_3\,(2\varepsilon_{snow} + 1)$. The depolarization terms (A_i) describe the relationship of permittivity with grain shape. In (3.13) A_1 is given for oblate spheroids, A_2=A_1, and A_3 = 1-2A_i. The Fourier integral of the autocorrelation function (I) which is provided in (3.14) contains the microstructure information in terms of the autocorrelation function, $A(x)$, while the scattering factor $\xi = 2k_{eff}({}^{\sin\varphi_{s-i}}\!/_2)$ where $\varphi_{s\text{-}i}$ is the scattering angle and k_{eff} = $k(\varepsilon_a)^{1/2}$. Equations (3.11) – (3.14) follow Mätzler (1998).

$$k_s = v(1-v)(\varepsilon_i - 1)^2 K^2 I k^4 \sin^2\theta_p \tag{3.11}$$

$$K^2 = \frac{1}{3}\sum_{j=1}^{3}\left|\frac{\varepsilon_a}{\varepsilon_a + (\varepsilon_i - 1)A_j}\right|^2 \tag{3.12}$$

$$A_1 = \begin{cases} 0.1 + 0.5v; & 0 < v \leq 0.33 \\ 0.476 - 0.64v; & 0.33 < v < 0.6 \end{cases} \tag{3.13}$$

$$I = \frac{1}{\alpha}\int_0^{\infty} A(x)x\sin(\zeta x)\,dx \tag{3.14}$$

Microstructure (including grain size) has a strong effect on volume scattering and its influence has been acknowledged in studies of microwave scattering in natural snow (Durand et al, 2008; Kendra et al., 1998; King et al., 2018; King et al., 2015; Mätzler, 1987; Proksch et al., 2015; Rott et al., 2010; Sandells et al., 2017). Volume scattering is also enhanced by snow density through the influence of density-dependent ε_{snow} on K^2. Measurable quantities required to calculate k_s in IBA include snow p_c and σ_{ds} which is advantageous since these can be easily measured in the field making IBA desirable for radiative transfer models like MEMLS (Mätzler et al., 2014; Proksch et al., 2015). Volume scattering may also occur within dense vegetation canopies (McNairn et al., 2002) however if the dimensions of the scatterer are much smaller than the propagating wave the medium appears electromagnetically homogeneous, and scattering will be diminished (Ulaby et al. 1981).

Not only do radiative transfer models, such as MEMLS, incorporate surface and volume scattering theory, but they also incorporate measurable physical snowpack properties such as those discussed in Sections 2.1 through 2.6 in order to simulate backscattered power. MEMLS was adapted in 2015 to include a backscatter model for active microwave (MEMLS3&a; Proksch et al., 2015) and remains a popular radiative transfer model (eg. Brucker et al., 2011; Harlow and Essery, 2012; King et al., 2018; Lemmetyinen et al., 2018; Lemmetyinen et al., 2016; Montpetit et al., 2013; Thompson et al., 2021). Given that MEMLS3&a is used in Chapter 6 it will be introduced in the following section.

3.4 MEMLS3&a

Microwave models are instrumental in understanding the radar response of snow and facilitating exploration of backscatter sensitivity to manipulation within the parameter space. As a result, this can improve our understanding of the relationship between variation in snowpack structure, including realistic constraints, and associated radar signatures while offering potential improvement in retrieval accuracy of parameters like SWE.

MEMLS3&a is a semi-empirical model that was adapted for active microwave backscatter from the original microwave emission model by leveraging Kirchoff's Law (3.15) which describes

the relationship between emissivity (e) and reflectivity (r) of a surface (Mätzler and Melsheimer, 2006; Mätzler et al., 2014; Proksch et al., 2015).

$$r = 1 - e \tag{3.15}$$

The snowpack is represented by a stack of homogeneous layers each characterized by parameters which can readily measured in the field including temperature (t), volumetric liquid water content (M_v), ρ_{snow}, layer thickness (Z), salinity (S_a), and p_{ex}. The modular nature of the snowpack representation allows for easy experimentation with stratigraphic parameterization in terms of number of layers. Absorption and scattering are determined using a six-flux approach. The k_a with angle of refraction (θ') drives layer transmissivity (u) and is controlled by ε_r which is influenced by frequency, ρ_{snow}, t, and S_a (Mätzler et al., 2014). The quantity k_s is a function of frequency, p_{ex} and ρ_{snow}. Several empirical formulations are available to calculate k_s (Wiesmann and Mätzler, 1999) as well as the IBA.

The air-snow interface is modeled as a slightly undulated surface where specular backscatter occurs only near normal incidence corresponding to the physical-optics solution for undulating surfaces and is determined from the empirically derived mean-square slope of surface undulation (Proksch et al., 2015). Mid-pack layers are separated by planar boundaries (Wiesmann and Mätzler, 1999) therefore reflectivity at layer interfaces (S_{int}) is governed by Fresnel reflectivity in (3.7) and (3.8) while refraction follows Snell's law and total specular reflectivity for all layers is calculated with a recurrence relation (Proksch et al., 2015). The model also accounts for coherent reflectivity for layers of sub-wavelength thickness (Mätzler et al., 2014; Wiesmann and Mätzler, 1999). The soil surface is considered rough, and reflectivity is defined externally using, for example, the Rough Bare Soil model in (3.9) and (3.10), while the specular portion of soil reflectivity is empirically defined. The "sandwich model" of Wiesmann et al. (1998) is implemented to track interface reflections and internal scattering within the snowpack while simulated backscatter is comprised of specular (s_s) and diffuse (s_d) components (Mätzler et al., 2014). Cross-polarized backscatter is determined directly from co-polarized backscatter with an empirical splitting factor thereby contributing no independent information (King et al., 2018). A schematic of the MEMLS3&a configuration is provided in Figure 3.3 which was modified from Proksch et al., 2015.

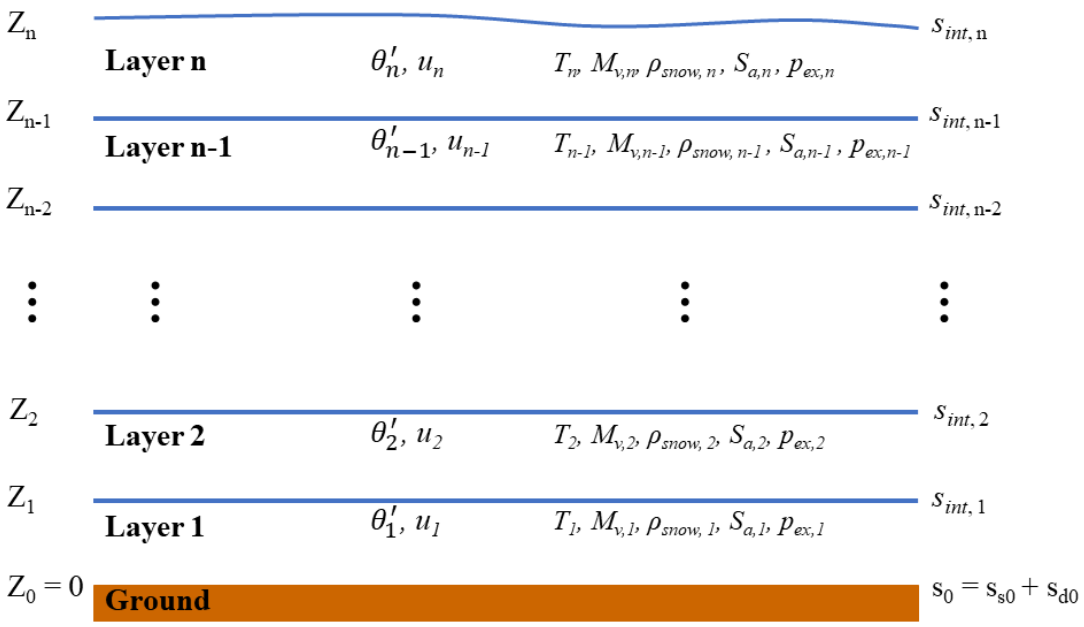

Figure 3-3. Schematic of MEMLS3&a configuration. Modified from Proksch et al., 2015.

An important distinction of MEMLS3&a (and the MEMLS family of models) and the reason why this model formulation was adopted in this thesis is the use of snow p_{ex} as the only microstructural input since this quantity can be objectively estimated from field or laboratory observations (King et al., 2018; Lemmetyinen et al., 2018; Proksch et al., 2015; Thompson and Kelly, 2021). In Chapter 6 this was achieved through conversion of D_{max} estimates followed by optimization of Φ (refer to Section 2.4 for D_{max} conversion and discussion of Φ). This is in contrast to models that use grain radius and conceptual parameters like stickiness which cannot be readily estimated in the field such as the Dense Media Radiative Transfer (DMRT) family of models, or the Helsinki University of Technology (HUT) model which relies on optical grain diameter. Furthermore, being a medium-complexity semi-empirical model (Proksch et al., 2015; Sandells et al., 2017), inversion and retrieval algorithms may be more easily accomplished than with a physically based model of greater complexity such as DMRT.

Chapter 4

Radar polarimetric response from a snow-covered landscape

4.1 Polarimetric description of a wave

The electric field of a wave can be described as the vector sum of orthogonal components, E_{0x} and E_{0y}, in the plane of $\hat{x}$ and $\hat{y}$, which is often arbitrarily labelled vertical and horizontal in reference to the surface of the Earth (Canadian Centre for Remote Sensing, 2015; Woodhouse, 2006). As the electric field evolves in space and time, the tip of the electric field vector in this plane traces an ellipse, the shape of which, referred to as the polarization ellipse, can be used to characterize polarization state (Cloude, 2010; Ulaby and van Zyl, 1990). The polarization ellipse (Figure 4.1) allows characterization of all possible polarization states in terms of the orientation angle (Ψ), the ellipticity angle (χ) and the orthogonal components of the electric field (E_{0x} and E_{0y}) at a fixed time.

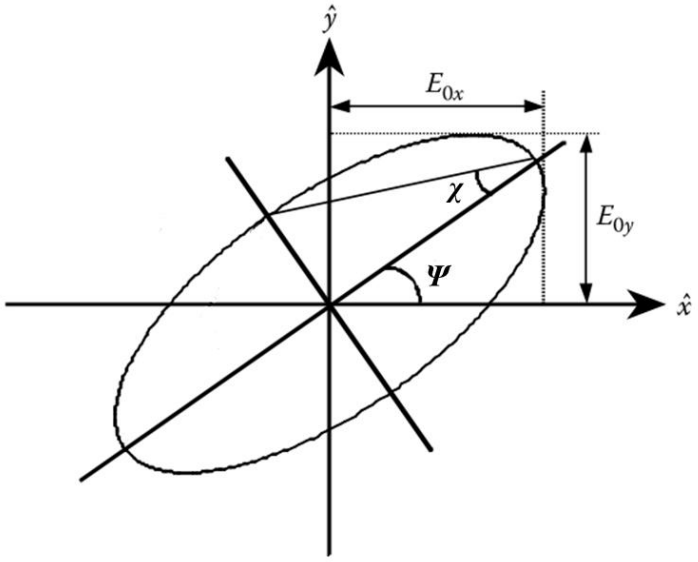

Figure 4-1. Polarization ellipse. Modified from Lee and Pottier, 2009.

The quantity $\chi \in \left[-\frac{\pi}{4}, \frac{\pi}{4}\right]$ describes the shape of the ellipse denoting linear polarization when the phase difference between E_{0x} and E_{0y} (δ) is 0 or π, corresponding with $\chi = 0°$, circular polarization when $\delta = \pm \pi/2$ and $E_{0x} = E_{0y}$, corresponding with $\chi = \pm \pi/4$, and elliptical polarization for values in between (Evans et al., 1988; van Zyl et al., 1987); linear polarization is commonly transmitted and such is the case with UWScat. The handedness of the polarization is indicated by the sign of χ where negative values indicate right-handedness and positive values represent left-handedness (Evans et al., 1988). The quantity $\Psi \in [0, \pi]$ is defined as the angle between the ellipse major axis and a reference direction often chosen as $\hat{x}$ (Cloude, 2010; Ulaby and van Zyl, 1990). It is a measure of the inclination of the major axis of the ellipse and denotes,

for the linear case, horizontal polarization (*H*) when $\Psi = 0 \; or \; \Psi = \pi$ and vertical polarization (*V*) when $\Psi = {}^{\pi}/_{2}$ (Evans et al., 1988; van Zyl et al., 1987). A co-polarized response occurs when the polarization of the scattered wave is the equal to that of the transmitted wave (*VV* or *HH*), while a cross-polarized response occurs when the polarization state of the scattered wave has been modified during interaction with the target (*VH* or *HV*). A fully polarimetric sensor, such as UWScat, can transmit and receive *VV*, *HH*, *VH*, and *HV* polarizations.

Alignment of incident polarization with physical structure of scatterers may result in preferential co-polarized backscattering (Geldsetzer, 2009). Examples of this include preferential *HH* or *VV* backscatter from similarly oriented vegetation (Arii et al., 2010; Yueh et al., 2009) and preferential *VV* backscatter from vertically aligned depth hoar chains (King et al., 2013; King et al. 2015), however, complexity of natural scenes may obscure such preferential scattering. Cross-polarized backscatter results from depolarization within an anisotropic medium which is misaligned with the incident microwaves leading to absorption and re-radiation in the orientation of the individual scatterers (Campbell, 2002). Examples of this may include interaction with forest canopy, driven by volume scattering at Ku-band frequencies (Thompson and Kelly, 2019) although magnitude of depolarization is frequency dependent where less depolarization occurs for larger wavelengths, given the same scattering target (Woodhouse, 2009). Depolarization is often coincident with volume scattering, but they are distinct since volume scattering describes the effect on scattered power, in terms of k_s, of a wave traversing a scattering medium, while depolarization describes the scattering interaction in terms of modification to Ψ and χ of the scattered wave.

4.2 Polarimetric statistics

Complex polarimetric measurements, comprised of amplitude and phase, are described by the scattering matrix (*S*) in (4.1) which characterizes the backscattering properties of a given target and the relationship between transmitted and received waves (Lee and Pottier, 2009).

$$S = \begin{pmatrix} S_{HH} & S_{VH} \\ S_{HV} & S_{VV} \end{pmatrix} \tag{4.1}$$

From *S*, the covariance matrix (*C*) can be derived (4.2) which describes the second-order scattering statistics which statistically relate the channels (Woodhouse, 2006). Ensemble averaging is denoted by $\langle ... \rangle$ and * denotes complex conjugation. For most natural targets reciprocity is assumed where $S_{HV} = S_{VH}$ which allows reduction of *C* from a 4x4 to a 3x3 matrix (Lee and Pottier, 2009; van Zyl et al., 1990). Elements of the main diagonal correspond to the conventional backscatter coefficients while off-diagonal elements describe covariance between co- and cross-polarizations (Park et al., 2014).

$$C = \begin{pmatrix} S_{HH}S_{HH}^* & \sqrt{2}S_{HH}S_{HV}^* & S_{HH}S_{VV}^* \\ \sqrt{2}S_{HV}S_{HH}^* & 2S_{HV}S_{HV}^* & \sqrt{2}S_{HV}S_{VV}^* \\ S_{VV}S_{HH}^* & \sqrt{2}S_{VV}S_{HV}^* & S_{VV}S_{VV}^* \end{pmatrix} \quad (4.2)$$

Polarimetric parameters used to aid analysis and interpretation can be derived from *C*, such as the co-polarization ratio (r_{co}), the depolarization ratio (r_{depol}), and the co-polarized phase difference Φ_{VVHH} shown in (4.3) through (4.5), respectively.

$$r_{co} = \frac{\langle |S_{VV}|^2 \rangle}{\langle |S_{HH}|^2 \rangle} \quad (4.3)$$

$$r_{depol} = \frac{\langle |S_{HV}|^2 \rangle}{\sqrt{\langle |S_{VV}|^2 \rangle \langle |S_{HH}|^2 \rangle}} \quad (4.4)$$

$$\phi_{VVHH} = \tan^{-1}\left[\frac{Im\langle S_{HH}S_{VV}^* \rangle}{Re\langle S_{HH}S_{VV}^* \rangle}\right] \quad (4.5)$$

The second-order statistics contained in *C* also provide a multivariate input for polarimetric decompositions, accounting for the combination of speckle and random scattering effects from surface and volume targets (Cloude and Pottier, 1996). These allow for classification of scattering mechanisms within the FOV and extraction of physical information from observed scattering (van Zyl, 1989). A commonly used polarimetric decomposition method, that is also used in the experimental chapters, will be described in the following section.

4.3 Freeman-Durden three-component decomposition

A common challenge in the analysis of polarimetric radar data is to infer geophysical parameters from a scene which exhibits substantial natural variability of scattering properties (van Zyl, 1993). An understanding of observed scattering properties in terms of known scattering mechanisms is therefore sought (van Zyl et al., 2008). Polarimetric decomposition can provide a means to accomplish both objectives. There are two general categories of decomposition: eigenvector-based and model-based. Eigenvector-based decompositions, introduced by Cloude (1992) provides unique solutions but the methods can be complex, and results can be difficult to interpret in terms of physical scattering mechanisms (van Zyl, 1993). Model-based decompositions, such as the Freeman-Durden three-component model (FD3c herein; Freeman and Durden, 1993; Freeman and Durden, 1998), express the measured covariance matrix as a linear sum of physical scattering mechanisms (Cloude, 2010; van Zyl et al., 2008). The primary advantages of such models are their simplicity, and their physical basis which allows interpretation of results in terms of known scattering mechanisms (Lee and Pottier, 2009). While the underlying physical basis for polarimetric decompositions can be traced to manufactured targets such as metallic spheres, dihedrals and

trihedrals these may not be representative of natural targets (Freeman and Durden, 1998). In this regard, the FD3c demonstrates flexibility with the lack of a strict requirement for orthogonality between scattering components (van Zyl, 1989). Furthermore, FD3c has been found to be more robust than Cloude's decomposition (Lee et al., 2004). For these reasons, the FD3c was implemented in Chapters 5 and 6.

The FD3c, summarized in (4.6), is widely used and has formed the basis for much work (eg. Antropov et al., 2011; Ballester-Berman and Lopez-Sanchez, 2010; Balzter et al., 2017; Freeman, 2007; Lee et al., 2004; Park et al., 2014; Singh et al., 2014; Surendar et al., 2015; Thompson and Kelly, 2019; Thompson and Kelly, 2021b; Trudel et al., 2009; van Zyl et al., 2011; Watanabe et al., 2006; Yamaguchi et al., 2005; Yamaguchi et al., 2011) is a physically-based three-component scattering mechanism model for use over natural, distributed scatterers which describes total backscattered power (**T**) as a linear combination of surface (*fs*), double-bounce (*fd*), and volume (*fv*) scattering components derived from covariance matrix statistics (Freeman and Durden, 1993; Freeman and Durden, 1998). The modeled scattering mechanisms include volume scattering from randomly oriented dipoles, first-order Bragg surface scattering, and a double-bounce mechanism; the term dipole is used to describe a thin, cylindrical object in this case (van Zyl and Kim, 2011).

$$\mathbf{T} = f_{\mathrm{s}}\begin{bmatrix} |\beta^2| & 0 & \beta \\ 0 & 0 & 0 \\ \beta^* & 0 & 1 \end{bmatrix} + f_{\mathrm{d}}\begin{bmatrix} |\alpha^2| & 0 & \alpha \\ 0 & 0 & 0 \\ \alpha^* & 0 & 1 \end{bmatrix} + f_{\mathrm{v}}\begin{bmatrix} 1 & 0 & 1/3 \\ 0 & 1/3 & 0 \\ 1/3 & 0 & 1 \end{bmatrix} \tag{4.6}$$

The term α describes dihedral scattering and it includes horizontal (R_{gh}) and vertical polarized (R_{gv}) Fresnel reflectivity coefficients from the horizontal surface, horizontal (R_{th}) and vertical (R_{tv}) reflection coefficients from the vertical surface, and propagation a term for horizontal (γ_h) and vertical polarization (γ_v) that describes attenuation and phase change through the medium (4.7). The term β is a real number describing first-order Bragg scattering.

$$\alpha = e^{i2(\gamma_h - \gamma_v)}\left(\frac{R_{gh}R_{th}}{R_{gv}R_{tv}}\right) \tag{4.7}$$

From (4.6) and (4.7), the model for total backscatter is derived (4.8).

$$\langle|S_{hh}|^2\rangle = f_s|\beta|^2 + f_d|\alpha|^2 + f_v \tag{4.8a}$$

$$\langle|S_{vv}|^2\rangle = f_s + f_d + f_v \tag{4.8b}$$

$$\langle S_{hh}S_{vv}^*\rangle = f_s\beta + f_d\alpha + {}^{f_v}/_3 \tag{4.8c}$$

$$\langle |S_{hv}|^2 \rangle = {f_v}/{3} \tag{4.8d}$$

$$\langle S_{hh} S_{vv}^* \rangle = \langle S_{hv} S_{hh}^* \rangle = 0 \tag{4.8e}$$

It is assumed that surface and double-bounce scattering components do not contribute to volume scattering, therefore the volume scattering component can be estimated directly from the cross-polarized term and subtracted from the system of equations in (4.8) leaving three equations in four unknowns. Following van Zyl (1989), the value of α or β is fixed based on the sign of $Re(S_{hh}S_{vv}^*)$. If $Re(S_{hh}S_{vv}^*)$ is negative it indicates double-bounce scatter is dominant in the residual and α = -1, otherwise β = 1 and surface scatter is dominant. The system of equations can be solved for the remaining variables and the contribution of surface (P_s), double-bounce (P_d), and volume scattering (P_v) is calculated as in (4.9) where total power (P) is the sum of contribution from each scattering mechanism such that $P = P_s + P_d + P_v$ (Lee and Pottier, 2009).

$$\begin{aligned} P_s &= f_s(1 + |\beta|^2) \\ P_d &= f_d(1 + |\alpha|^2) \\ P_v &= f_v \end{aligned} \tag{4.9}$$

Several important assumptions form a basis for the FD3c. Reflection symmetry is assumed as in (4.8e) which suggests a complete decorrelation between co- and cross-polarized backscatter coefficients (Antropov et al., 2011). The assumption may be violated in urban areas, and heavily sloped terrain (Lee et al., 2004; van Zyl et al., 2011). This is linked to another assumption that all cross-polarized power is attributed to volume scattering. Urban areas and sloped terrain could contribute to cross-polarized power although it may not be due to volume scattering (van Zyl et al., 2011). This may lead to overestimation of volume scattering in such regions (Antropov et al., 2011) although for most terrain this contribution is small (van Zyl et al., 2011). Finally, volume scatterers are represented as a cloud of randomly oriented dipoles. The importance of this assumption varies with target and frequency. Some forest species may not be randomly oriented or symmetrical (Arii et al., 2011) which may be perceptible at longer wavelengths since they will interact with the larger, structural components of trees, however shorter wavelengths will interact with smaller canopy elements and scatterers may appear randomly oriented (Thompson and Kelly, 2019). A limitation of this model, particularly in urban and geometrically complex scenes, is the potential to obtain negative power estimates for surface or double bounce scattering mechanisms due to speckle (An et al., 2010; Antropov et al., 2011; Freeman, 2007; van Zyl et al., 2011), however, this can be mitigated by averaging over more pixels (Freeman, 2007) or negative power can be restricted to zero with proportional adjustments to the remaining scattering mechanisms for total power conservation (Lee et al., 2004).

Although originally developed for discrimination of forest and natural land cover, these methods have also been applied to snow cover. Many studies of polarimetric decomposition of snow make use of model-based decompositions such as FD3c or a derivative (eg. Ma et al., 2020; Park et al., 2014; Singh et al., 2014; Surendar et al., 2015; Thompson and Kelly, 2021; Trudel et al., 2009). However, most of these studies used data from commercially available spaceborne C- and L-band instruments, the frequency and resolution of which may limit sensitivity to physical snow properties and as such, most studies were limited to snow extent and wetness. Thompson and Kelly (2021b) estimated tundra wind slab layer thickness with ground-based, Ku-band observations. The difference in system parameters in terms of frequency and spatial resolution likely resulted in different response to the snowpack than earlier studies and their observed lack of sensitivity to physical snow properties.

Chapter 5
UWScat description

Radar measurements analyzed in Chapters 6 through 8 were made exclusively with UWScat and so a description of the system and associated methods will be provided in this chapter. This will include a description of the specifications and physical components, field deployment methods, calibration, post-processing, near-field correction, and system error, followed by a brief history of deployment.

5.1 System description

UWScat is a portable ground-based frequency modulated, continuous-wave (FMCW) radar scatterometer system consisting of two standalone subsystems which operate in the Ku-band and X-band frequency range with centre frequencies of 17.2 GHz and 9.6 GHz, respectively, and a bandwidth of 500 MHz providing a range resolution of 0.30 m (ProSensing, 2009). UWScat system parameters are provided in Table 5.1.

Table 5-1. UWScat system parameters.

Parameter	Ku-band	X-band
Output frequency (GHz)	16.95–17.45	9.35–9.85
Center frequency (GHz)	17.2	9.6
Transmit power (narrow, flood; dBm)	−8, 3.5	−11.8, 9.5
Transmit bandwidth (MHz)	500	500
Range Resolution (m)	0.3	0.3
Antenna beam width (narrow, flood; °)	5.6, 7.5	4.3, 5.8
Cross-polarization isolation (dB)	>30	>30
Transmit/receive polarizations (linear)	VV, HH, VH, HV	VV, HH, VH, HV
Sensitivity (dB m^2m^{-2})	−50	−50

Each UWScat subsystem is comprised of a radio-frequency (RF) unit, a data acquisition system, a modified Kipp and Zonen 2ap Suntracker (herein referred to as the positioner), and a tripod. The RF unit contains the RF hardware and antennae. In order to stabilize sensitive RF hardware in winter conditions, the RF unit is thermally regulated with a heating circuit to maintain an internal temperature of 35°C. A dual antenna design allows narrow beam operation with a single antenna, limiting parallax, and wide beam operation adding a corrugated flood-beam antenna to improve sensitivity at greater distances while reducing leakage (King et al., 2013). A custom designed waveform generator in each RF unit produces a linear FM chirp which sweeps from 69.58-90.41 MHz, then upconverts to 389.58-410.41 MHz and multiplies by 12 before applying a frequency doubler to generate a linear FM sweep from 9350-9850 MHz at X-band. For Ku-band the 9350-9850 MHz chirp is upconverted to 169750-17450 MHz (ProSensing, 2009). In both systems, the chirp waveform is split evenly by a power divider for use by the transmitter and receiver and a portion of the signal is used to downconvert the received waveform to baseband,

while the other portion is sent to one of four transmit ports. The received signal is filtered, amplified and downconverted to baseband and sent to the data acquisition system along a 10 m double shielded coaxial cable (ProSensing, 2009). The data acquisition system is mounted in a heated, shock-mounted, weather resistant enclosure and includes an uninterruptible power supply, the host computer, and a temperature controller which provides thermal management for the RF unit and the enclosure. A GaGe 1602 digitizer in the host computer receives the baseband signal from the RF unit and processes it. A single sweep of the FM waveform is collected for each transmit-receive polarization combination, along with a calibration loop, and the noise signal resulting in six data blocks which comprise a single record, retained for offline processing (King et al., 2013). The system is mounted with the positioner onto a leveled steel tripod. The positioner allows for operator-controlled 360° azimuth rotation and a 90° range of incidence angle, from 15° to 105° in programmable increments.

5.2 Field deployment

During field deployment UWScat is typically mounted on a portable wooden platform on top of the snowpack to provide stability during measurement (eg. Thompson and Kelly, 2021a; Thompson and Kelly, 2021b; Thompson et al., 2019). During tree canopy measurement, however, additional instrument height is required. This can be accomplished by mounting UWScat on the platform of a stationary tower or a scissor lift (eg. Thompson and Kelly, 2019). Figure 5.1 illustrates ground-level and elevated deployment. Power in remote locations is provided by a generator.

Following assembly, UWScat measurements consist of sweeps through the programmed azimuth rotation, followed by programmed incrementation of incidence angle and an opposite azimuth rotation. The measurement proceeds until rotation through the specified range of azimuth and incidence angles has been accomplished, after which point the azimuth and incidence angle rotation restarts, creating a new measurement. At the beginning of each measurement, an in-scene trihedral calibration target (see left side of Figure 5.1a) is illuminated in the system far field for external calibration to estimate signal distortion and generate a correction matrix used to correct the received voltage at each polarization, following Geldsetzer at al., (2007). Sky observations are made following each measurement in order to characterize system leakage as part of the calibration procedure. Finally, an internal calibration loops quantifies variation in gain to generate correction during post-processing.

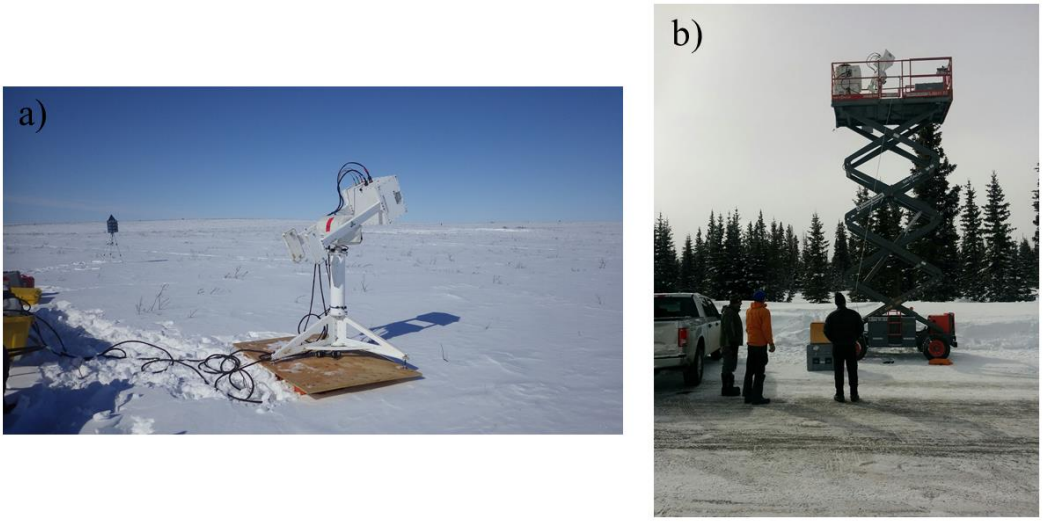

Figure 5-1. Field deployment of UWScat. Typical ground-level installation of UWScat on wooden platform at Trail Valley Creek, NT in April 2017 (a). Deployment on scissor lift to measure tree canopy during NASA's SnowEx campaign at Grand Mesa, CO in February 2017 (b).

5.3 Post-processing

During post-processing, a Hanning window is applied to the raw samples to minimize sidelobes and a range profile is derived from the Fourier transform of the raw data, and the calibration methods described earlier are applied to the data (ProSensing, 2009). Total backscattered power is estimated as the sum of power within a user-defined number of range gates centred on the user-identified peak return in the range profile. The data is averaged into a covariance matrix containing 16 polarimetric cross-products and the calibrated σ° values for each of the principal polarization states are extracted from the real terms along the main diagonal.

The far-field distance (r_f) for the antennae (5.1) describes the range beyond which measurements may be made without near-field correction as a function of is the parabolic antenna diameter (D) and λ. For the narrow beam Ku- and X-band antennae, the far-field distance is about 5.4 m and 17.1 m, respectively.

$$r_f = 2D^2/\lambda \tag{5.1}$$

For targets within this distance, a range-dependent correction factor (Γ_r) must be applied such as (5.2) from Sekelsky (2002) which depends on range-to-target (r_t) and r_f. This is commonly applied to UWScat measurements for ground-level deployments (see Figure 5.1a) for which the target is

generally within the far-field distance. However, from an elevated platform (see Figure 5.1b), the target may be beyond the far-field distance depending on platform elevation and may not require a near-field correction.

$$\Gamma_r = \frac{0.0117 + \left({}^{r_t}/_{r_f}\right)^{2.5}}{5.26 * 10^{-5} + \left({}^{r_t}/_{r_f}\right)^{2.5}} \tag{5.2}$$

An estimate of σ° is determined in (5.3) from the average power profiles and calibration data after Geldsetzer et al. (2007) where h_{ant} is antenna height, σ_c is the radar cross section of the calibration target, R_c is the range to calibration target, and Θ_{3dB} is the one-way half-power beamwidth of the antenna. The quantities P_r and P_{rc} represent recorded power for the scene and calibration target, respectively.

$$\sigma^o = \frac{8\ln(2)\, h_{ant}^2 \sigma_c}{\pi R_c^4 \theta_{3dB}^2 \cos(\theta)} \left(\frac{P_r}{P_{rc}}\right) \tag{5.3}$$

5.4 Error estimation

Total error ($\Delta_{total}^{\pm}$)in UWScat measurements is a function of the number of independent samples (N_{ind}), calibration uncertainty and signal-to-noise ratio (SNR) due to uncertainty in the estimation of observational geometry (King et al., 2013). The $\Delta_{total}^{\pm}$ comprises random error (σ_{ran}), multiplicative bias errors ($\Gamma_{cal}^{\pm}$) and residual multiplicative calibration errors ($\Gamma_{res}^{\pm}$) (Geldsetzer et al., 2007).

Sarabandi et al. (1990) describes σ_{ran} as the standard deviation of the signal power (5.4) which is a function of N_{ind}, the SNR, and the number of noise samples (N_n). The N_{ind} can be estimated by dividing the azimuthal angular width by half of the antenna beam width and multiplying by the number of range gates within the footprint (Geldsetzer et al., 2007). The SNR is determined from the ratio of selected impulse range power to the sky observation power, while N_n represents the number of sky observations used which is assigned a value of 1 since the sky observations are averaged in preprocessing (King, 2014). The expression in (5.4) assumes an independent noise sample has been subtracted from received power when estimating signal power (Geldsetzer et al., 2007).

$$\sigma_{ran} = \sqrt{\frac{1}{N_{ind}}\left(1 + \frac{1}{SNR}\right)^2 + \frac{1}{N_n}\left(\frac{1}{SNR}\right)^2} \tag{5.4}$$

The tripod supporting the corner reflector may cause clutter in the range gate containing the calibration target resulting in calibration bias. The resulting $\Gamma_{cal}^{\pm}$ can be estimated in (5.5) from the signal-to-clutter ratio (SCR) following Geldsetzer et al. (2007) where the positive and negative superscripts indicate out-of-phase error and in-phase error, respectively, providing a worst-case estimate of calibration bias. Estimates of SCR can be produced from observation of the tripod without the calibration target (King, 2014).

$$\Gamma_{cal}^{+} = \frac{1}{\left(1 - \frac{1}{\sqrt{SCR}}\right)^2} \tag{5.5a}$$

$$\Gamma_{cal}^{-} = \frac{1}{\left(1 + \frac{1}{\sqrt{SCR}}\right)^2} \tag{5.5b}$$

Any remaining multiplicative error, including inaccurate estimation of range, footprint, and incidence angle have been aggregated in $\Gamma_{res}^{\pm}$ with an assumed value of ± 0.5 dB (Geldsetzer et al., 2007).

Finally, the $\Delta_{total}^{\pm}$ is determined in (5.6) following Geldsetzer et al. (2007). Estimates of $\Delta_{total}^{\pm}$ for UWScat measurements used in this thesis are around ± 2.0 dB.

$$\Delta_{total}^{+} = \Gamma_{cal}^{+}\Gamma_{res}^{+}(1 + \sigma_{ran}) \tag{5.6a}$$

$$\Delta_{total}^{-} = \Gamma_{cal}^{-}\Gamma_{res}^{-}(1 + \sigma_{ran}) \tag{5.6b}$$

5.5 History of deployment

The portability of UWScat allows for deployment in challenging environments. Since 2009, UWScat has provided data for a number of different studies. During the Canadian CoReH$_2$0 Snow and Ice Experiment (Can-CSI) in 2009-2010 and the Canadian Snow and Ice Experiment (CASIX) in 2010-2011, UWScat was deployed in Churchill, MB to obtain measurements of snow-covered sub-arctic environment (King et al., 2013; King et al., 2015), freshwater ice (Atwood et al., 2015; Gunn et al., 2015a; ; Gunn et al., 2018; Gunn et al., 2015b), and forest canopy (Thompson and Kelly, 2019) in support of the CoReH$_2$0 mission proposal. In 2017, UWScat provided data for NASA's SnowEx campaign in Grand Mesa, CO which focused on understanding the influence of forest canopy on SWE retrieval (Kelly and Thompson, 2018; Thompson and Kelly, 2019). It has been deployed on sea ice in 2012 in Resolute, NU (Nandan et al., 2017) and again during 2019-2020 with the Multidisciplinary drifting Observatory for the Study of Arctic Climate (MOSAiC)

project led by the Alfred Wegener Institute (AWI). It has also been deployed in mid-latitude Ontario (Maryhill, Englehart, and Tobermory) for snow, vegetation and forest canopy observation during the winters spanning 2013-2015 (Thompson and Kelly, 2019; Thompson et al., 2019; Thompson and Kelly, 2021a) and in arctic tundra at Trail Valley Creek, NT in 2017 for snow observation (Thompson and Kelly, 2021b).

Chapter 6
Considerations for Ku-band radar retrieval of snow water equivalent at mid-latitude Ontario agricultural sites

6.1 Introduction

Snow is an important source of freshwater (Barnett et al., 2005; Sturm et al., 2017) which plays critical roles in the global energy balance (Warren, 1982) and other related processes at or near the Earth's surface (eg. Barnett et al., 2005; Flanner et al., 2011) but there is mounting uncertainty, exacerbated by climate change, in terms of its spatio-temporal distribution (Brown and Mote, 2009; Pulliainen et al., 2020), therefore remote, large-scale monitoring of this important resource has become a priority (National Academies of Science, 2019). Radar remote sensing at certain frequencies has demonstrated sensitivity to accumulated snow (eg. Ulaby and Stiles, 1980; Ulaby et al., 1984), however, unlike snow cover extent, we currently lack the ability to make accurate remote measurements of snow water equivalent (SWE) (Bormann et al., 2018).

Radiative transfer models are an important tool to explore the interaction of microwaves with the natural environment. In the forward direction such models can be used to demonstrate physical understanding and evaluate the influence of unknowns (King et al., 2018); They provide a means for retrieving physical properties such as SWE and snow microstructure when inverted. Accurate retrieval of SWE is a common goal that is well-reflected in the research (eg. Cui et al., 2016; Lemmetyinen et al., 2018; Zhu et al., 2018), and its success depends heavily on the understanding of snow grain microstructure (Royer et al., 2017) which also remains a focus (eg. King et al., 2018; Lemmetyinen et al., 2018; Rutter et al., 2019).

Contemporary active microwave modeling studies have used the Microwave Emission Model of Layered Snowpacks adapted for backscattering (MEMLS3&a; Proksch et al., 2015), hereafter referred to as MEMLS (eg. King et al., 2018; Lemmetyinen et al., 2018; Lemmetyinen et al., 2016) while the Dense Media Radiative Transfer (DMRT) family of models, adapted for active mode (Tan et al., 2015; Tsang et al., 2007) has remained equally popular (eg. Tan et al., 2015; Tsang et al., 2007; Zhu et al., 2018). The newly released Snow Microwave Radiative Transfer model (SMRT) provides a uniquely modular approach permitting a choice of microstructure, electromagnetic, and radiative transfer models (Picard et al., 2018; eg. Rutter et al., 2019).

Despite different modeling approaches, no single model has demonstrated superiority (Löwe and Picard; 2015; Picard et al., 2018). Being that DMRT is a physically-based numerical model, its complexity exceeds that of MEMLS which is a semi-empirical model of intermediate complexity (Proksch et al., 2015; Sandells et al., 2017). The microstructural representation varies between these models as well. DMRT-QCA relies on a spherical representation of snow grains defined by a radius and the concept of stickiness which cannot be readily estimated from field

measurements but facilitates numerical solutions of Maxwell's equations (Brucker et al., 2011; Löwe and Picard, 2015; Picard et al., 2018). However, the exponential correlation length, derived from the exponential fit to the spatial autocorrelation function (Mätzler, 2002) and required by the improved Born approximation (IBA) of Mätzler (1998) to compute the scattering coefficient within MEMLS, can be derived from objective field-based measurements (Proksch et al., 2015). Furthermore, Löwe and Picard (2015) demonstrated near-equivalence of DMRT and the IBA. Finally, the flexibility of SMRT was not required. For these reasons, MEMLS was chosen for the research herein. Regardless of model choice, representation of the snowpack microstructure has been identified as among the most influential parameters (Sandells et al., 2017) and in most radiative transfer models, simulation bias is controlled with a microstructure scaling factor accounting for error in model physics and parameterization which arises from different sources in each implementation (Brucker et al., 2011; King et al., 2018; Lemmetyinen et al., 2018; Montpetit et al., 2013; Sandells et al., 2017).

Advancement on the interaction between radar and snow volume, including retrieval efforts, have focused primarily on high-latitude or high-altitude taiga, tundra, and alpine (eg. Cui et al., 2016; King et al., 2018; Lemmetyinen et al., 2018; Lin et al., 2016; Rutter et al., 2019); this also includes large-scale campaigns such as CLPX, CASIX, SARALPS, and SnowEx. Fewer radar studies have considered mid-latitude environments (eg. Thompson et al. 2019), which include 4.2 million ha of agricultural fields in Ontario alone (Ontario Ministry of Agriculture, Food, and Rural Affairs, 2017), although several passive microwave studies have done so (eg. Brucker et al., 2011; Larue et al., 2018; Montpetit et al., 2013; Roy et al., 2013). There are important reasons to consider this region. Firstly, a retrieval scheme established for one region may not be valid in another (Brucker et al., 2011; King et al., 2018; Lemmetyinen et al., 2018), therefore it is important to develop knowledge in regions outside of those most commonly studied. Secondly, mid-latitude sites offer exposure to unique conditions such as ice lenses and vegetation partially buried within the snowpack. Such conditions occur less frequently at high latitudes; this may change as the north continues to warm. Finally, in Ontario alone, with a population exceeding 14 million, and an agriculture sector which contributes $10 billion annually to the Canadian GDP, the mid-latitude region, where snow remains an important source of freshwater, is of immense economic importance (Ontario Ministry of Agriculture, Food, and Rural Affairs, 2020; Statistics Canada, 2020). Snow in this region also contributes to hydropower generation which accounts for about 26% and 61% of total electricity generation in Ontario and Canada, respectively, with much of it occurring at mid-latitude (Canada Energy Regulator, 2021).

Despite the economic importance of the mid-latitude region, a lack of region-specific research may exacerbate risk exposure for those inhabitants dependant on snow as a freshwater resource or sensitive to snowmelt-driven flooding, especially in the face of growing uncertainty

with respect to snow accumulation. Furthermore, results of this research may apply to similar agricultural regions across Canada and the northern United States.

Variation in air temperature, precipitation, and wind speed, produce distinct snowpack characteristics in terms of grain type, microstructure, and density (Colbeck, 1982; Sturm et al., 1995) which have a profound impact on the radar response at certain frequencies (King et al., 2018). Therefore, substantial differences between snowpacks in terms of these characteristics produce potentially distinct radar responses with implications for SWE retrieval (Rutter et al., 2019). The snowpacks in this study are characteristic of the mid-latitudes and most often fit within the maritime snow class described by Sturm et al. (1995), with some exception. It is a product of relatively warm air and soil temperatures commonly resulting in ice features and equilibrium grains. This is in stark contrast to the tundra snow class commonly found at high latitudes which is primarily comprised of depth hoar and wind slab resulting from high wind speed, low precipitation, and cold air temperatures (Derksen et al., 2014). Likewise, the taiga snow class is distinguished from the maritime snow class by cold air temperatures and the development of depth hoar through the season, characterized by poorly defined stratigraphy (Lemmetyinen et al., 2018; Sturm et al., 1995). The difference in snow characteristics between classes suggest distinct radar responses, given the influence of microstructure on radar backscatter (King et al., 2018; Lemmetyinen et al., 2018; Rutter et al., 2019). Along with snow microstructure, soil effects can also influence SWE retrieval accuracy and should therefore be incorporated in the retrieval (King et al., 2018). Soils in the study area are predominately inorganic and may produce a unique signature differing from that of the peat-based organic soils which underlay the snow in many high-latitude study sites.

For these reasons, it is important to improve our understanding of the snow-radar interaction in this under-studied region. To do so, we use MEMLS, which provides the necessary modelling framework. The overall aim of this study is to demonstrate Ku-band radar remote sensing of mid-latitude snow for SWE retrievals. The following four objectives are set out to achieve this:

(1) Demonstrate forward modelling skill by parameterizing MEMLS with *in situ* snow observations from mid-latitude sites and evaluate model output against coincident backscatter observations at 17.2 GHz made with the University of Waterloo Scatterometer (UWScat).
(2) Understand and characterize the influence of mid-latitude snow properties on the radar response at 17.2 GHz.
(3) Account for the effects of background soil scattering in radar data using a soil-subtraction scheme.
(4) Demonstrate the performance of a MEMLS-based SWE retrieval in this environment given the outcomes of objectives 1 through 3.

6.1.1 Site

Alfalfa fields on inorganic soil in Maryhill (80.3798°W, 43.54887°N) and Englehart (79.8354°W, 47.7621°N), Ontario were chosen for this study, providing similar subnivean dielectric and surface roughness characteristics among sites, which constrained background scattering (see Thompson et al. 2019 for full site descriptions). During the first year (2013-2014) four adjacent sites within a plot named the first year Hergot site in Maryhill were visited on four separate dates. In the second year (2014-2015) three Maryhill sites, named the Hergot site, Zinger site, and John's farm, were revisited on multiple occasions throughout the entire season. Three sites in Englehart, named e1(and e1 revisit), e2, and e3, were also observed during the second year. The study site locations are shown in Figure 6.1. UWScat observations and *in situ* observations of snow and soil were made at these sites which will be described in the following section.

Figure 6-1. Study sites in Englehart (L) and Maryhill (R) from Thompson et al. (2019). Sites numbers are: 1) e1, 2) e1 revisit, 3) e2, 4) Zinger, 5) first year Hergot, 6) second year Hergot, and 7) John's farm.

6.1.2 Snowpack, soil, and meteorological observations

Snow pit observations following protocol of Fierz et al. (2009) were coincident with UWScat observations; snow pits were located adjacent to the UWScat field of view (FOV). Snow pit measurements included snow depth, snow density and vertical temperature profile, along with stratigraphy and grain size observations. Snow density was measured with a 100 cm^3 box-style density cutter and electronic scale. From density, the real portion of the complex relative permittivity of snow (ε'_{snow}) was estimated as in Mätzler (1996). The vertical temperature profile was measured at 10 cm intervals with an analog probe thermometer. Grain size was defined as the largest axis of the dominant grain (D_{max}) and was estimated with a hand lens and gridded card with 1 mm grid spacing.

Distributed snow depth measurements were made in transects on each date and at each site during the winter of 2014-2015, excluding March 8, 2015. In order to determine the spatial autocorrelation of snow depth in this environment, semivariograms of snow depth were plotted in Figure 6.2. For the Maryhill sites, the average range of spatial autocorrelation was 26.4 m while the range in Englehart was 25.3 m. This was in good agreement with the 30 m range observed by Shook and Gray (1996) over flat fields with agricultural stubble. Sites for which model fit failed to converge included the Zinger site on January 24 and February 5, and the Hergot site on January 31, 2015 (point clouds plotted for reference).

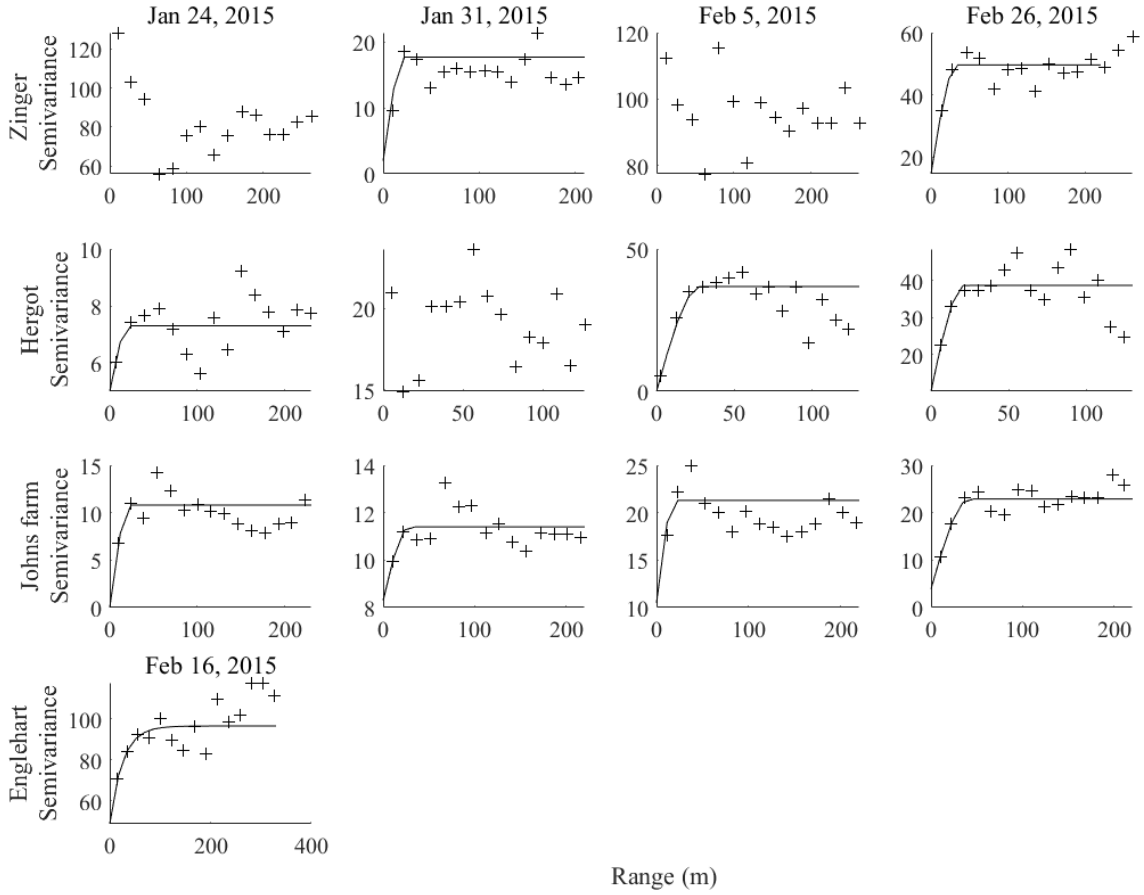

Figure 6-2. Snow depth semivariograms for Maryhill and Englehart sites.

A meteorological station was deployed near the Maryhill sites, while in Englehart meteorological data was obtained from the Earlton-Timiskaming Regional Airport which was 7 km from the study site. Soil properties were measured with Delta-T WET sensors (50 MHz operating frequency; Maryhill sites) installed in the ground before soil freeze-up, and with Stevens HydraProbes (20 MHz operating frequency; Maryhill and Englehart sites); measurements included soil temperature, soil moisture, and the real portion of the complex relative permittivity of soil

(ε'_{soil}). Measurements of the imaginary portion of the complex relative permittivity of soil (ε''_{soil}) were not available. A regression-based correction was applied to HydraProbe measurements to account for operating frequency and measurement technique (refer to Thompson et al. (2019) for full description). A summary of snowpack, soil, and meteorological observations for selected sites is presented in Table 6.1; these sites were used in the optimization and parameterization of forward modelling and the retrieval algorithm since they comprise simple, pure snow.

Table 6-1. Chronological summary of snowpack, soil, and meteorological observations for selected sites. Data represents a subset of that which was presented in Thompson et al. (2019). Temperature measurements were coincident with snow pit and UWScat observations.

Date	Region	Site	Snow depth (cm)	Snow bulk density (kg/m3)	SWE (mm)	# of layers	ε'_{snow}	Air temp (°C)	soil int. temp (°C)	Soil temp (°C)	ε'_{soil}
01/24/15	MH	Zi	21	313	66	4	1.6	-5	-4	na	na
01/31/15	MH	Zi	9	313	28	3	1.6	-8	-8	na	na
02/05/15	MH	He	26	185	48	4	1.3	-11	-4	-2.9	7.1
02/05/15	MH	Zi	29	278	81	7	1.5	-16	-5	-3.8	6
02/16/15	EN	e1	54	262	141	12	1.5	-27	-8	-4.7	6.2
02/17/15	EN	e2	67	286	192	13	1.5	-15	-6	-6.5	5.9
02/19/15	EN	e3	55	250	138	9	1.4	-24	-7	-4.7	6.2
02/19/15	EN	Er	55	250	138	9	1.4	-24	-7	-4.7	6.2
02/26/15	MH	He	30	236	71	5	1.4	-12	-5	-3.4	7.1
02/26/15	MH	Zi	37	258	95	8	1.4	-14	-5	-4.5	5.8

MH = Maryhill; EN = Englehart; Zi = Zinger; He = Hergot; Er = e1 revist

The snowpack at these sites generally included wind slab (except for Jan 31 Zinger and Feb 5 Hergot), depth hoar (except Jan 31 Zinger), and mixed snow; mixed snow primarily comprised rounded snow grains, but also transitional grains and new snow. A discontinuous basal ice layer with a thickness of 0.5 cm was observed at some locations within the e2 site in Englehart. A pictogram of the stratigraphy is provided in Figure 6.3.

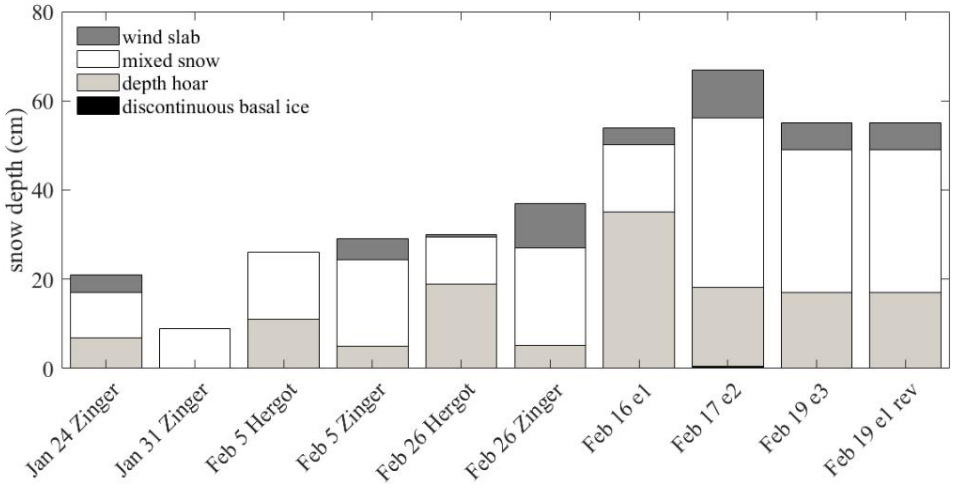

Figure 6-3. Pictogram of snowpack stratigraphy at all sites. Similar layers have been aggregated.

Sites excluded from optimization due to the inclusion of ice lenses and partially buried vegetation are summarized in Table 6.2 and Figure 6.4 (refer to Thompson et al. (2019) for complete descriptions). These conditions are common in mid-latitude environments and will be tested in the retrieval algorithm after it has been optimized with the sites in Table 6.1.

Table 6-2. Summary of sites with ice lenses and vegetation. All sites located in Maryhill.

Date	Site	Snow depth (cm)	snow bulk density (kg/m3)	SWE (mm)	# of layers	ε'_{snow}	Air temp (°C)	snow-soil int. temp (°C)	Soil temp (°C)	ε'_{soil}	Condition
01/31/14	He	41	367	151	11	1.7	-4	-3	-1.0	6.7	mi
02/02/14	He	28	296	83	5	1.5	-7	-3	-1.0	6.7	mi
02/28/14	He	40	413	165	10	1.8	-12	na	-1.4	6.7	mi
01/24/15	He	12	230	28	3	1.4	-4	-4	-2.7	7.3	gv
01/24/15	Jf	12	363	44	3	1.7	-3	-4	-3.0	6.1	gv-bi
01/31/15	He	15	213	32	3	1.4	-7	-4	-4.2	7.1	gv
01/31/15	Jf	13	341	44	4	1.6	-5	-5	-5.6	5.6	gv-bi
02/05/15	Jf	35	305	107	4	1.5	-12	-4	-3.9	5.8	bi
02/26/15	Jf	35	297	104	5	1.5	-12	-6	-5.3	5.8	bi
03/08/15	Zi	50	285	143	10	1.5	-3	-4	-3.4	6.1	si
03/08/15	He	26	225	59	5	1.4	-2	-4	-2.5	7.1	si
03/08/15	Jf	43	328	141	8	1.6	0	-4	-3.6	6.0	si-bi

He = Hergot; Jf = John's farm; Zi = Zinger;
mi = mid-pack ice lens; gv = green veg; bi = basal ice; si = surface ice lens

Mid-pack and basal ice lenses were observed during 2014 in Maryhill while basal ice lenses were observed at John's farm in 2015. A freezing rain event deposited a smooth ice lens at the surface of

the snowpack on March 8, 2015 at the Zinger, Hergot, and John's farm sites. These observations were accompanied by air temperatures reaching 1° C resulting in surface melt of the ice lenses. A dense crop of green alfalfa plants was present early in the 2015 season at the Hergot site and John's farm. The vegetation, partially buried in snow, roughened the snow surface where it protruded from microwells at the air-snow interface, and gradually desiccated from the top down with exposed extents dying first, followed by the snow-covered stems prior to the February 5, 2015. Coarse melt form snow grains from early-season warming events were present near the surface at these sites on January 24 and 31, 2015.

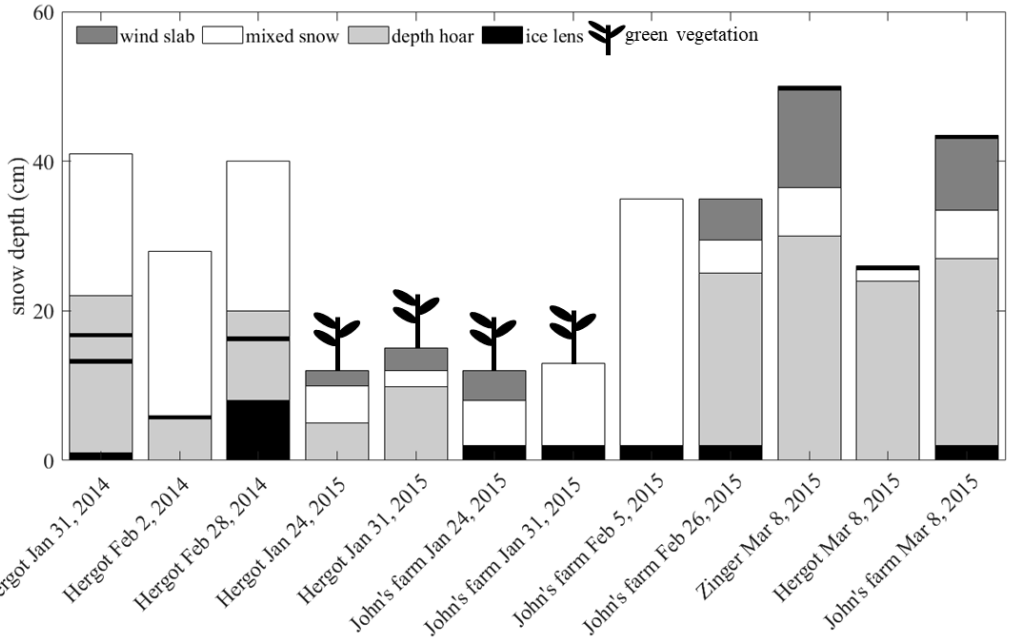

Figure 6-4. Snowpack stratigraphy of special cases. Similar layers have been aggregated. Vegetation not to scale.

When possible, UWScat observations of snow-free, frozen ground were made in order to measure background scattering from the soil. Snow was manually excavated with shovels immediately following observation of the natural snowpack allowing for snow-free observations. While effort was made to minimize modification of conditions at the soil surface during excavation, soil ridges could become broken from shovelling, and residual snow grains could become fractured and compacted in hollows, resulting in a hard, artificially flattened surface. A summary of sites and conditions during the bare ground observations is provided in Table 6.3.

Table 6-3. Summary of conditions during bare ground observations.

Date	Region	Site	Air Temp (°C)	Soil temp (°C)	ε'_{soil}
01/31/14	Maryhill	Year 1 Hergot	-4.1	-1.0	6.7
02/02/14	Maryhill	Year 1 Hergot	-6.7	-1.0	6.7
02/28/14	Maryhill	Year 1 Hergot	-11.6	-1.4	6.7
02/19/15	Englehart	e1	-24.2	-4.8	6.2

6.1.3 UWScat observations

Observations of dry snow were made with UWScat at 17.2 GHz, and VV polarization since this combination has demonstrated superior sensitivity to snow accumulation over HH polarization due in part to vertical orientation of depth hoar (eg. King et al., 2015; Thompson et al., 2019) which was present at most sites, while minimizing influence from horizontal layering structure. Furthermore, the cross-polarized response in MEMLS is simply scaled from the co-polarized response (Proksch et al., 2015), therefore it adds no independent information (King et al., 2018) so it was excluded from the study. UWScat observations consisted of operator-programmed azimuth sweeps with an incremented incidence angle (θ). Observations from each azimuth sweep were averaged, yielding a single measurement per θ, to improve measurement precision and mitigate radar fade. Azimuth sweeps of 40° and an increment of 3° between θ = 35° and θ = 59° were specified; this resulted in a minimum of 28 independent samples at 35° and maximum of 56 independent samples at 59°. Given the ground-based tripod-mounted configuration of UWScat, range-to-target for these observations was within the near-field range of the antenna, requiring application of the near-field gain correction described by Sekelsky (2002). Additional description of UWScat can be found in King et al. (2013), King et al. (2015), Thompson and Kelly (2019), and Thompson et al. (2019). Conditions within the UWScat FOV were assumed to be homogeneous.

6.2 Methods

6.2.1 MEMLS parameterization and optimization

Originally developed to simulate microwave emission from a stack of horizontal snow layers (Mätzler and Wiesmann, 1999; Wiesmann and Mätzler, 1999), MEMLS was modified in 2015 to simulate backscatter (Proksch et al., 2015). This semi-empirical radiative transfer model employs six-flux theory to describe scattering and absorption. The scattering coefficient is analytically determined using the Improved Born Approximation (IBA) of Mätzler (1998). Inputs for each horizontal snow layer include exponential correlation length of snow (p_{ex}), snow density, layer thickness, temperature, water content, and salinity, all of which can be derived from *in situ* measurements (Proksch et al., 2015); salinity and water content were assumed to be zero in the analyses that follow. Snow microstructure is described by p_{ex} since it is considered a more objective and accurate measure than D_{max}, however, it must be scaled before use in MEMLS to

minimize bias (Mätzler, 2002). Background scattering from subnivean soil must be simulated from an external model.

6.2.1.1 Soil modeling

In order to account for background scattering within MEMLS, soil reflectivity (S_o) was simulated using the Rough Bare Soil Reflectivity model of Wegmüller and Mätzler (1999) which derives the H-polarized rough soil reflectivity (S_H) and the V-polarized rough soil reflectivity (S_V) in (6.1) and (6.2). Simulation required wavenumber (k), standard deviation of surface height (h), θ, and calculation of the horizontal Fresnel reflection coefficient (R_H) which also required ε'_{soil}. Given the frozen condition, soil was assumed a low-loss medium (Wegmüller, 1990). Lacking measurements, ε''_{soil} was therefore neglected (eg. Lemmetyinen et al., 2018; Sandells et al., 2017). Snell's law was used to modify θ to account for refraction within the snowpack and k was modified as in Shi and Dozier (2000) to account for shortening of the incident wavelength.

$$S_H = R_H \exp\left(-(kh)^{\sqrt{-0.1\cos\theta}}\right) \tag{6.1}$$

$$S_V = S_H \cos\theta^{0.655} \tag{6.2}$$

Given a lack of distributed soil roughness measurements, h was optimized in MEMLS with a centimetre-thick, single-layer snowpack to mimic snow-free ground (MEMLS requires a snow thickness > 0 cm). The optimization was performed with increments of 0.1 cm for 0.1 cm ≤ h ≤ 5.0 cm at each θ. Simulated backscatter at each θ was compared with the associated snow-free UWScat observation for the corresponding θ. Using (6.3), the RMSE in dB was calculated for each combination of h and θ, where s represents the number of sites (ie. number of rows in Table 6.3). The RMSE was averaged across all θ, yielding $RMSE_{h,avg}$ for each value of h. Finally, h_{opt} was determined as in (6.4). The optimized h (h_{opt}) was found to be 1.4 cm as shown in Figure 6.5. Optimized h ranged from 0.2 cm to 3.9 cm across each incidence angle with a standard deviation of 1.3 cm. Using one standard deviation to bound the model in conjunction with a centimetre-thick snowpack to replicate a snow-free scene, it was found that uncertainty in h accounted for about 2.6 dB of variability on average.

$$RMSE = \sqrt{\frac{\sum_{i=1}^{s}\left(\sigma^0_{sim,i,\theta,h} - \sigma^0_{obs,i,\theta,h}\right)^2}{s}} \tag{6.3}$$

$$h_{opt} = min\left(RMSE_{h,avg}\right) \tag{6.4}$$

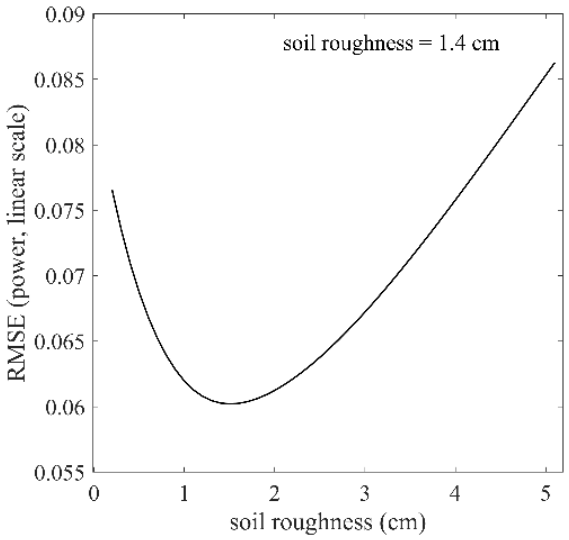

Figure 6-5. Optimization of *h*.

Specular reflection at the snow-soil interface (S_{s0}) is defined in MEMLS as a proportion of S_0. A S_{s0} value of $0.3S_0$ was chosen for this study following Lemmetyinen et al. (2016) although other studies have specified a S_{s0} of $0.75S_0$ (eg. King et al., 2018; Proksch et al., 2015). The effects of S_{s0} are associated with the penetrative capability of incident microwaves within the snowpack and become more apparent in thinner snowpacks and at lower frequencies (Proksch et al., 2015). Greater S_{s0} is associated with smooth ground (Proksch et al., 2005), but the sites in Maryhill and Englehart were estimated to be radar rough (Thompson et al., 2019), therefore $S_{s0} = 0.3S_0$ was deemed appropriate. A comparison of simulated VV-polarized 17.2 GHz backscatter for the sites listed in Table 6.1 was made with $S_{s0} = 0.3S_0$ and $S_{s0} = 0.75S_0$. To characterize the significance of this choice, an increase in S_{s0} from $0.3S_0$ to $0.75S_0$ was associated with a decrease in backscatter of 0.8 dB on average, for these sites.

6.2.1.2 Microstructure scaling and soil-subtraction

Microstructure scaling factors are used in radiative transfer models to effectively adjust measured or modelled microstructure estimates to minimize bias and account for errors in measurement, model parameterization and model physics (King et al., 2018; Lemmetyinen et al., 2018; Lemmetyinen et al., 2016; Montpetit et al., 2013; Sandells et al., 2017). Scaling factors vary widely in the literature from 0.16 (Wiesmann et al., 2000) to 5.3 (Rutter et al., 2014) since a unique scaling factor is required for different models and field measurements, given the different physical association between scattering and microstructure of each (Sandells et al., 2017); for this reason, we sought a unique scaling factor. However, across regions with dissimilar snow, and potentially different dominant metamorphic processes, a further distinction may be required (King et al., 2018; Löwe and Picard, 2015). The Maryhill and Englehart sites were situated in dissimilar snow classes according to the climate-based snow class distribution map by Sturm et al. (1995). Class

membership was verified using the discriminant function of Sturm et al. (1995) based on *in situ* measurements of snow depth, air temperature, snow-soil interface temperature, and snow bulk density; on average, snow at the Maryhill sites was characteristic of the maritime class while snow at the Englehart sites was characteristic of the taiga class. Therefore, the Maryhill and Englehart sites were treated separately in the analyses and a unique scaling factor was determined for each.

In order to minimize the influence of soil in determination of the scaling factor, an effective background scattering observation was generated by averaging the backscatter from each snow-free observation in Table 6.3. This was subtracted from each UWScat observation listed in Table 6.1 to create a soil-subtracted observation which isolated snowpack scattering in the determination of an appropriate scaling factor. This method ensured that the scaling factor would only account for errors in snowpack parameterization and modeling. Validation for the soil-subtraction method is provided in Section 6.4.1. Assumptions of this method include cold, dry snow thus minimizing attenuation. Therefore, this method would not be appropriate for wet snow or that featuring substantial wind slab given the potential increase in attenuation; error may also increase with deep snow accumulation.

Estimates of D_{max} required conversion to p_{ex} for use in MEMLS but to do so, it was first converted to correlation length (p_c), using the linear relationship derived by Royer at al. (2017) and given in (6.5):

$$p_c = 0.1069 D_{max} \tag{6.5}$$

Conversion to p_{ex} exploits an empirical linear relationship given in (6.6), which relates the quantities by a multiplicative scaling parameter (Φ) that varies with snow type (Brucker et al., 2011; Mätzler, 2002).

$$p_{ex} = \Phi p_c \tag{6.6}$$

An optimal Φ (Φ_{opt}) to convert and scale the microstructure parameter was determined by iterating $0.1 \leq \Phi \leq 3.0$, by 0.1, while matching simulated and observed, soil-subtracted backscatter in order to minimize bias, following Brucker et al. (2011).

This was completed for each θ at a given site using an n-layer snowpack parametrization in which each of the *n* snow layers in the snowpack were parameterized, achieving maximum fidelity. Using (6.7), the RMSE was calculated for each combination of Φ and θ, where *s* represents the number of sites. The mean value of the resultant RMSE was averaged across θ for each value of Φ yielding $RMSE_{\Phi,avg}$. Finally, Φ_{opt} was determined as in (6.8). As shown in Figure 6.6, $\Phi_{opt,MH}^{n-layer} = 1.2$ for the

Maryhill sites, while $\phi_{opt,EN}^{n-layer} = 1.5$ for sites in Englehart. Values of $\Phi > 1$ indicated the model was underestimating snowpack scattering. While the scaling factor can account for modeling error, the presence of depth hoar at both sites, particularly Englehart, may contribute to these values since the ratio of p_{ex}/p_c in (6.6) exceeds unity where sufficient depth hoar is present (Mätzler, 2002); it may also explain why $\phi_{opt,EN}^{n-layer} > \phi_{opt,MH}^{n-layer}$ since depth hoar was generally more abundant in Englehart.

$$RMSE = \sqrt{\frac{\sum_{i=1}^{s}\left(\sigma_{sim,i,\theta,\Phi}^{0} - \sigma_{obs,i,\theta,\Phi}^{0}\right)^2}{s}} \tag{6.7}$$

$$\phi_{opt} = min\left(RMSE_{\phi,avg}\right) \tag{6.8}$$

Without relying on field observations in a SWE retrieval, the stratigraphy in a snowpack remains unknown and snowpack parameterization should be simplified for computational efficiency. While results obtained with the original n-layer parameterization provide a benchmark in accuracy, a simplification was sought. The snow at Maryhill and Englehart was composed, in part, of depth hoar and wind slab which have important implications at 17.2 GHz including enhanced scattering and absorption, respectively (King et al., 2018). The remaining snow was characterized as rounded and new snow and aggregated into a single category since they were of a similar intermediate D_{max}.

Parameterizations tested included 1-, 2-, and 3-layer schemes. Parameterizations exceeding 3 layers lacked clear physical meaning and were not considered for the retrievals. In the 1-layer scheme each snowpack was collapsed into a single layer using a layer-thickness weighted averaging scheme. In the 2-layer scheme, depth hoar comprised the bottom layer while remaining snow types, including wind slab, new snow, and rounded snow, comprised the top layer. In the 3-layer scheme depth hoar comprised the bottom layer, wind slab comprised the top layer, and other snow types (new and rounded grains) comprised the middle layer. Similar snow was aggregated using a layer-thickness weighted averaging scheme.

Reusing (7) and (8), Φ_{opt} was determined for the 1-, 2-, and 3-layer parameterizations. The parameterization with Φ_{opt} closest to that of the $\phi_{opt}^{n-layer}$ was selected for the forward simulation and retrievals. The 1-layer parameterization was chosen for Maryhill since $\phi_{opt,MH}^{1-layer} = 1.3$ was closest to $\phi_{opt,MH}^{n-layer}$, suggesting the model was still representing scattering well. The 2-layer parameterization was chosen for the Englehart sites since $\phi_{opt,EN}^{2-layer} = 1.6$ was closest to $\phi_{opt,EN}^{n-layer}$ which suggested similar levels of performance between the n-layer and 2-layer parameterizations. Optimizations of Φ are shown in Figure 6.6.

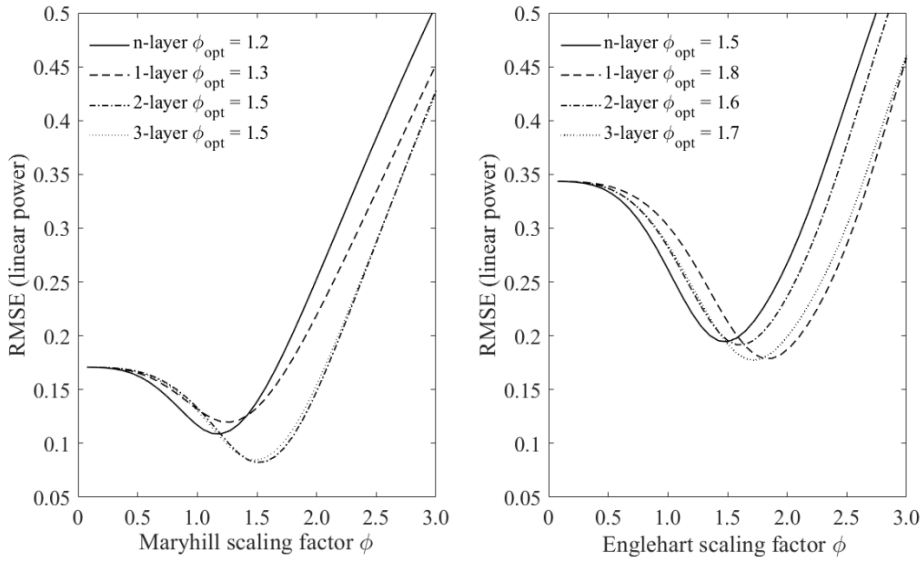

Figure 6-6. Determination of microstructure scaling factor.

6.2.2 MEMLS SWE retrieval

6.2.2.1 Maryhill retrieval

In order to develop a retrieval independent of *in situ* field measurements, snow depth, snow bulk density and p_{ex} were considered free parameters constrained by the range of observations made over two seasons in Maryhill and those made in Englehart. Soil roughness was also treated as a free parameter, constrained by the range of values generated in the *h* optimization process detailed in Section 6.3.1. Each free parameter could either be iterated through a range of values or it could be assigned the mean value of all observations; in order to capture a larger sample, range and mean values were calculated from all 2014-2015 Maryhill sites observed in Thompson et al. (2019) and not just those in Table 6.1. Table 6.4 describes the configurations used in the 1-layer Maryhill parameterization and provides configuration examples. In each configuration either the full range of snow depth was used, or the minimum snow depth was constrained to 10 cm. Since there were four parameters (snow depth, bulk density, p_{ex}, and *h*) each with two possible configurations (eg. range or mean), there was a total of sixteen unique combinations each of which were tested to determine the optimal configuration for the retrieval; Table 6.4 shows five of these combinations. Snow temperature was held constant at 263 K, which was the mean value of all observations. With a standard deviation of 3.6 K there was limited observed variation in snow temperature and observations were consistently below 0°C. Retrieved SWE for each θ at each site ($SWE_{Ret,\theta}$) was determined from snow depth and bulk snow density identified in the cost function.

Table 6-4. Free parameters used in 1-layer Maryhill retrieval and model configuration examples.

Component	snow (1-layer)			substrate
Parameter	snow depth (cm)	density (kg/m^3)	p_{ex} (mm)	h (cm)
Range	1-50; 10-50	226-330	0.16-0.26	0.09-2.7
Increment	1	1	0.01	0.2
Mean	na	278	0.21	1.4*
Rationale	full range of observed values	mean ± 1 std. dev.	mean ± 1 std. dev.	h_{opt} ± 1 std. dev.
Configuration	1	1	1	1
examples by	1	1	1	2
row	1	1	2	1
1 = range	1	2	1	1
2 = mean	1	1	2	2

* h_{opt}

Within an individual site (ie. a single row in Table 6.1), SWE was retrieved for each θ separately, by inverting MEMLS and minimizing a cost function (9) in an iterative scheme, matching simulated and observed backscatter.

$$\left(SWE_{Ret,\theta}\right) = \left[\sigma^{o}_{sim,\theta}(x_1 \dots x_r; c_1 \dots c_r) - \sigma^{o}_{obs,\theta}\right]^2 \tag{9}$$

Simulated backscatter for each θ was denoted as $\sigma^{o}_{sim,\theta}$ while the corresponding backscatter observation for each θ was denoted as $\sigma^{o}_{obs,\theta}$. Free parameters and configuration parameters are denoted as x_r and c_r, respectively. Retrieved SWE for each individual site ($SWE_{Ret,site}$) was then determined by calculating the mean retrieved SWE from each θ. To determine the optimal configuration, the retrieval results of each configuration were compared after aggregating results of each site and minimizing RMSE as in (6.10), where *s* represents the number of sites.

$$optimal\ configuration = min\left[\left(\frac{1}{s}\sqrt{\sum_{n=1}^{s}\left(SWE_{Ret,site} - SWE_{Obs,site}\right)^2}\right)\right] \tag{6.10}$$

6.2.2.2 Englehart retrieval

The Englehart retrieval was functionally similar to the Maryhill retrieval except for the dual-layer parameterization conceptualized as depth hoar and wind slab. The proportion of depth hoar was iterated in increments of 10% from 0% to 100% of total snow depth, while the remainder was wind

slab. Free parameters in each layer consisted of snow density, p_{ex}, and h which were constrained as shown in Table 6.5. Increments of density and h were increased to accelerate computation. With six free parameters (total snow depth, wind slab density and p_{ex}, depth hoar density and p_{ex}, and h) each with two possible configurations (eg. range or mean), there was a total of sixty-four unique combinations, each of which were tested to determine the optimal configuration for the retrieval of SWE; Table 6.5 shows five of these combinations for example.

Table 6-5. Free parameters used in 2-layer Englehart retrieval and model configuration examples.

Component	bulk snowpack	proportion of depth hoar	snow top layer (wind slab)		snow bottom layer (depth hoar)		substrate
Parameter	snow depth (cm)	percentage (%)	density (kg/m^3)	p_{ex} (mm)	density (kg/m^3)	p_{ex} (mm)	h (cm)
Range	1-70; 10-70	0-100	200-283	0.06-0.29	263-328	0.24-0.46	0.09-2.7
Increment	1	10	10	0.01	10	0.01	0.2
Mean	na	na	241	0.18	295	0.35	1.4*****
Rationale	full range of observed values	0% - 100% depth hoar	mean ± 1 std. dev.	mean ± 1 std. dev.	mean ± 1 std. dev.	mean ± 1 std. dev.	hopt ± 1 std. dev.
Configuration examples by row	1	1	1	1	1	1	1
	1	1	1	1	1	1	2
	1	1	1	1	1	2	1
1 = range	1	1	1	1	2	1	1
2 = mean	1	1	1	2	1	1	1

***** h_{opt}

6.2.2.3 Additional tests: fixed depths, vegetation, and ice lenses

Much of the mid-latitude land in Canada is inhabited which means access to consistent snow depth measurements is more practical than in many northern environments; access to such data may improve the accuracy of SWE retrievals. To verify this, snow depth measurements at three distance scales were incorporated into the best-performing retrieval algorithms. At the *in situ* scale, coincident snow depth measurements made adjacent to UWScat were utilized in the retrieval for both Maryhill and Englehart sites. Next, snow depths measured at the local scale by a nearby meteorological station in Maryhill were used. The station was situated 1 km from the Hergot site and 1.5 km from the Zinger site. At the regional scale, snow depths recorded at the Region of Waterloo International Airport were used in the retrieval (ECCC, 2020); the airport was situated 10 km from the Hergot site and 10.5 km from the Zinger site. Local and regional measurements were not available in Englehart. Snow depths measured at *in situ*, local, and regional scales are listed in Table 6.6. Finally, the sites in Table 6.2 were tested in the best-performing retrieval algorithm to

determine the influence of ice lenses and partially buried vegetation on retrievals. This was repeated using *in situ* snow depths.

Table 6-6. Snow depths from in situ measurements, nearby meteorological station, and airport.

Date	Region	Site	*in situ* (cm)	Met station (cm)	Airport (cm)
01/24/15	Maryhill	Zinger	21	4.9	4
01/31/15	Maryhill	Zinger	9	5.7	9
02/05/15	Maryhill	Hergot	26	12.8	32
02/05/15	Maryhill	Zinger	29	12.8	32
02/16/15	Englehart	e1	54	na	na
02/17/15	Englehart	e2	67	na	na
02/19/15	Englehart	e3	55	na	na
02/19/15	Englehart	e1 revisit	55	na	na
02/26/15	Maryhill	Hergot	30	16.4	32
02/26/15	Maryhill	Zinger	37	16.4	32

6.2.2.4 Retrieval evaluation

Overall RMSE for each SWE retrieval configuration incorporated retrieval accuracy from each date and site. All SWE retrievals were evaluated against an accuracy benchmark of 30 mm (eg. ESA, 2012). The configuration of the retrieval with the lowest overall RMSE was selected as the optimal configuration in each case.

6.3 Results

6.3.1 Optimization of forward modeling

Results of forward modelling with the n-layer configuration are shown in Figure 6.7 representing a baseline measure of how well the model can simulate the UWScat observations. Correlations between simulated and observed backscatter were strongest for mid-range θ while RMSE was greatest for larger θ. The strongest correlation was R=0.82 when θ=44° while the minimum RMSE of 1.47 dB occurred when θ=41°. Across all angles, the average correlation (± 1 standard deviation, used herein) was R_{avg}= 0.69 ± 0.09 and the average RMSE was $RMSE_{avg}$ = 2.27 ± 0.81 dB. The average range of observed backscatter was 6.7 dB while the average sensitivity of model estimates was only 3 dB.

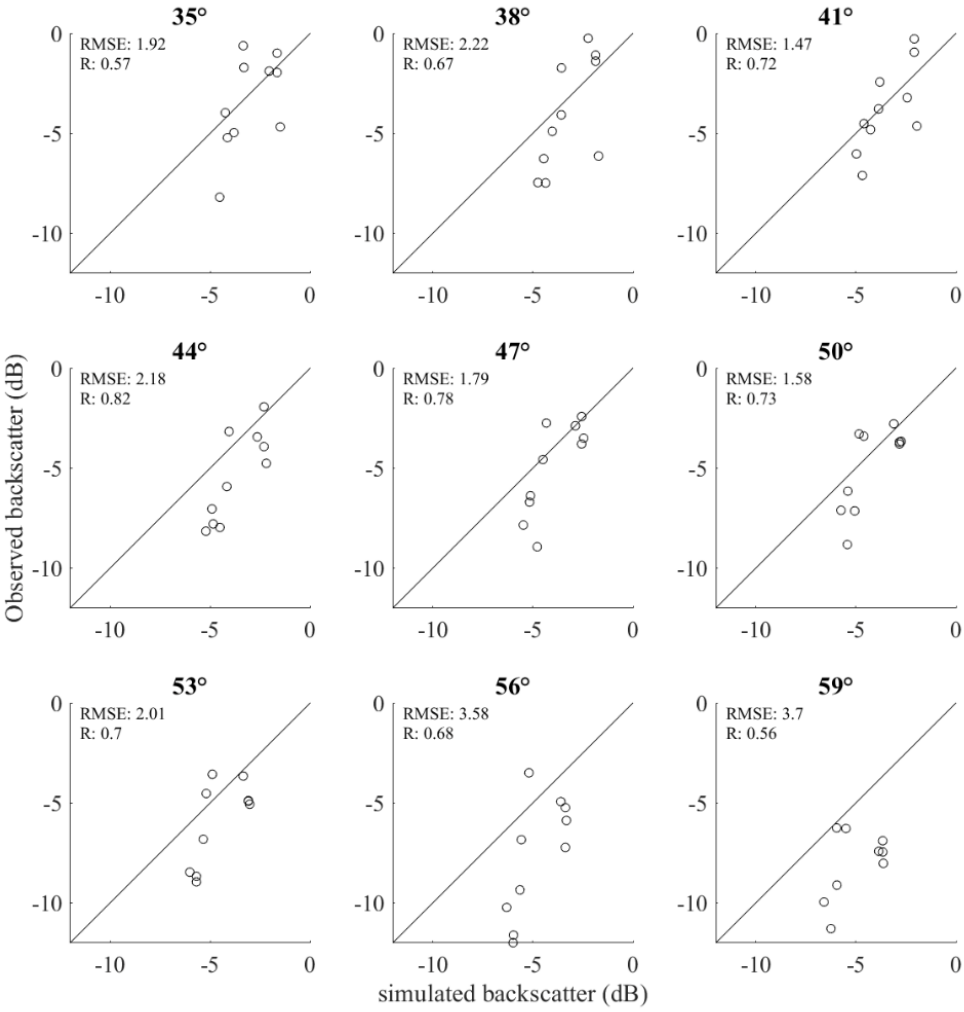

Figure 6-7. Results of forward modeling with n-layer configuration.

6.3.2 SWE retrieval

Optimal retrieval performance for Maryhill was achieved with density constrained to its mean value of 278.1 kg/m^3 and with h and p_{ex} constrained free parameters (refer to Table 6.4 for Maryhill parameter constraints). Minimum snow depth was constrained to 10 cm. This yielded overall RMSE values of 21.9 mm of SWE and 5.2 cm of snow depth, besting the 30 mm target by more than 8 mm. Figure 6.8 illustrates the Maryhill SWE and snow depth retrieval results.

The largest error occurred at the Hergot site on February 5, 2015, where SWE was overestimated by about 45 mm, more than twice the overall RMSE. The same date and site also yielded the greatest error in snow depth, overestimating by 8 cm. A negative bias was observed in both SWE and snow depth retrievals where wind slab was present except at the Hergot site on February 26, 2015, with a wind slab layer of 0.6 cm, associated with a positive snow depth retrieval bias of 1 cm.

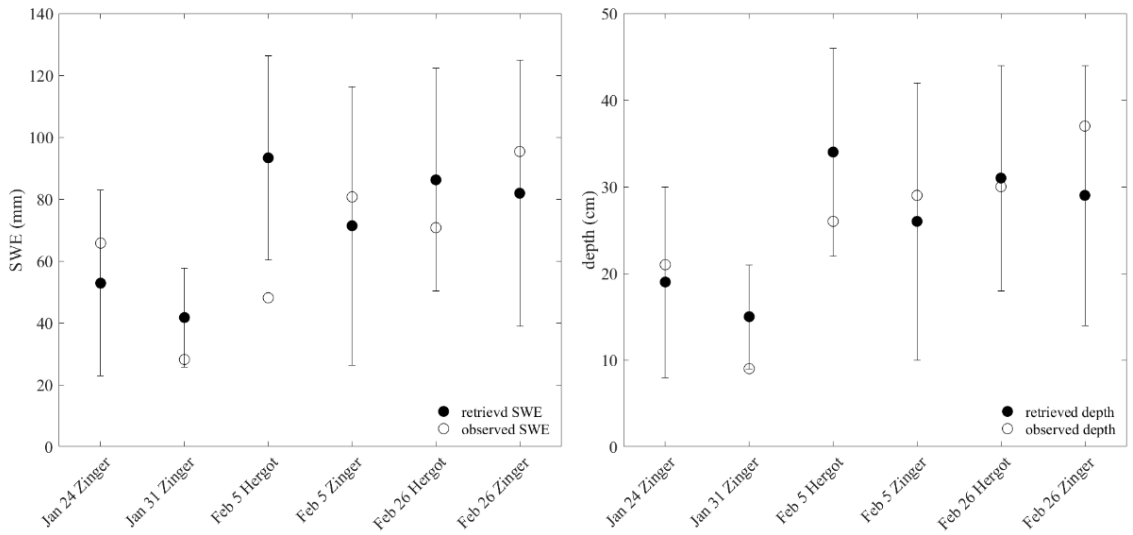

Figure 6-8. Maryhill SWE (left) and snow depth (right) retrieval results. Error bars represent one standard deviation based on the average retrieved SWE and depth over all incidence angles.

For the Englehart sites, optimal retrieval performance was achieved with wind slab p_{ex} a constrained free parameter and all other parameters constrained to their mean values (refer to Table 6.5 for Englehart parameter constraints). No improvement was observed when minimum snow depth was constrained to 10 cm. Overall RMSE values for SWE and snow depth retrievals were within the 30 mm accuracy target at 24.6 mm and 7.8 cm, respectively. Figure 6.9 illustrates the Englehart SWE and snow depth retrieval results. The largest error for both SWE and snow depth occurred for site e2 on February 17, 2015; SWE was underestimated by 46 mm while snow depth was underestimated by 13 cm. Negative bias was observed at all sites in the snow depth retrieval.

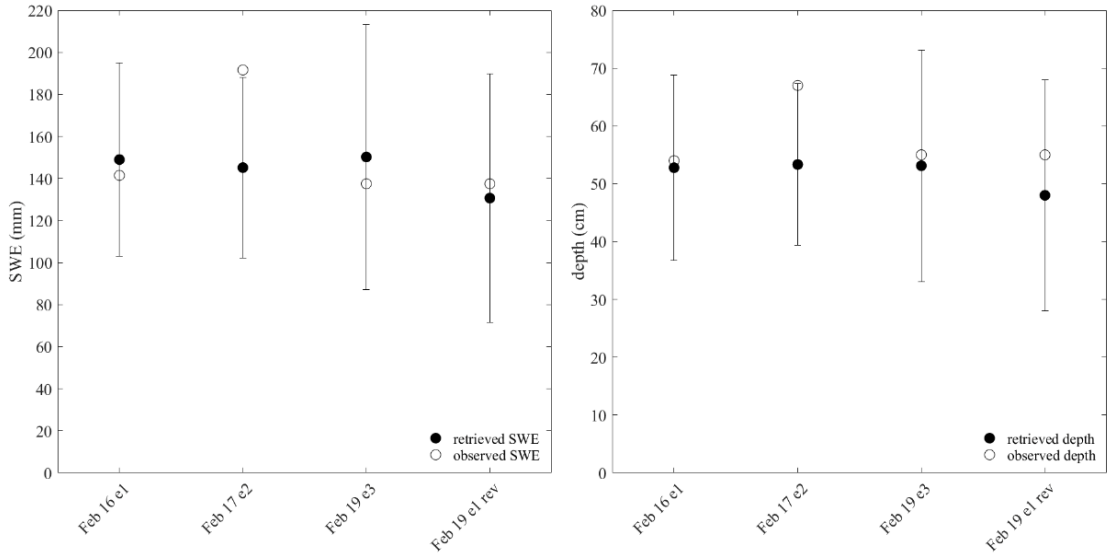

Figure 6-9. Englehart SWE (left) and snow depth (right) retrieval results. Error bars represent one standard deviation as described in Figure 6.8 caption.

Retrieval accuracy improved when *in situ* snow depths were used, as shown in Figure 6.10. For the Maryhill sites, overall RMSE = 12.0 mm SWE and for the Englehart sites overall RMSE =10.9 mm SWE. Using local scale snow depths (Maryhill only), accuracy decreased with overall RMSE = 36.9 mm, which failed to meet the 30 mm threshold. Substituting regional scale snow depths (Maryhill only) resulted in an overall RMSE = 29.8 mm SWE, just meeting the 30 mm threshold.

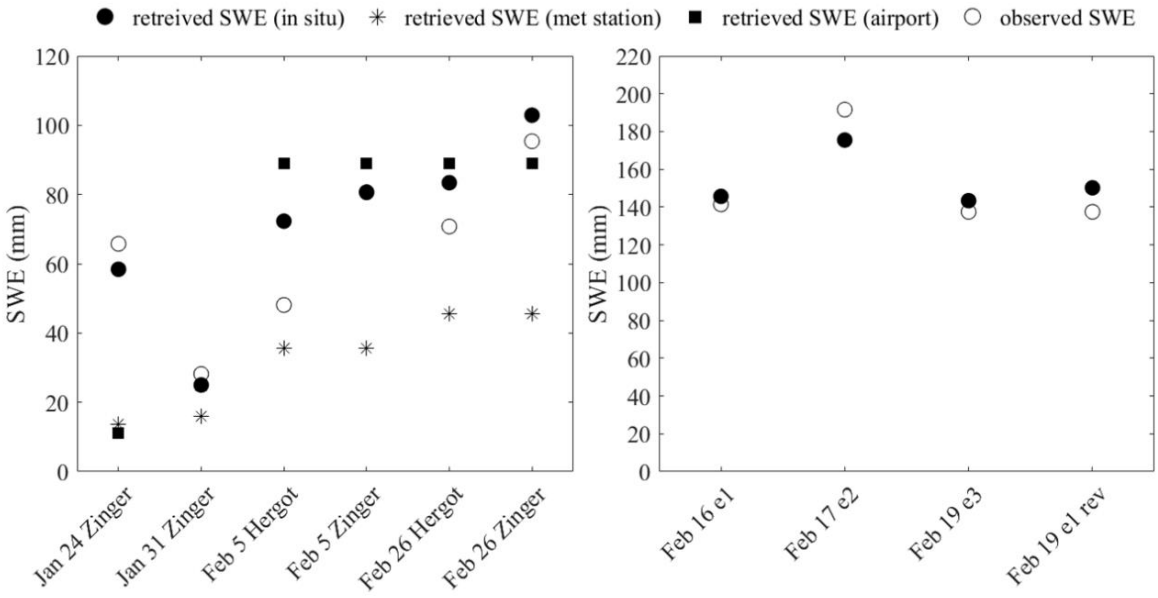

Figure 6-10. Retrieval results for Maryhill (left) using snow depths from in situ measurements, meteorological station, and airport. Englehart retrieval results (right) using in situ snow depths. Retrieved SWE using in situ depth is equal to that using airport depth on Jan 31 at the Zinger site. Retrieved SWE using in situ depth is equal to observed SWE on Feb 5 at the Zinger site.

Retrieval results for sites with ice lenses and partially buried vegetation are shown in Figure 6.11. Overall accuracies of RMSE = 17.9 cm and 60.4 mm were noted for snow depth and SWE respectively. The most accurate snow depth retrievals were for the 2014 Hergot sites (mid-pack ice layers), and John's farm on January 24 and 31, 2015 (combination of partially buried vegetation and basal ice), with error not exceeding 8 cm. The SWE retrievals performed best for John's farm on January 24 and 31, 2015 (combination of partially buried vegetation and basal ice) where retrieved SWE was within 5 mm of observed SWE.

Overall retrieval accuracy improved with the use of *in situ* snow depths yielding an overall RMSE = 21.1 mm SWE. The largest improvements in SWE retrieval accuracy occurred for John's farm on March 8, 2015 (surface ice), and the Hergot site on January 24, 2015 (partially buried vegetation). An improvement of about 91 mm SWE occurred in both cases. Substantial improvements were also made at the Hergot site on January 31, 2015 (partially buried vegetation),

and at the Zinger and Hergot sites on March 8, 2015 (surface ice), with improvements of 65.5 mm, 60.0 mm, and 44.5 mm, respectively. The use of *in situ* snow depths reduced the accuracy of SWE retrievals for John's farm on January 24 and 31, 2015 by up to 6 mm.

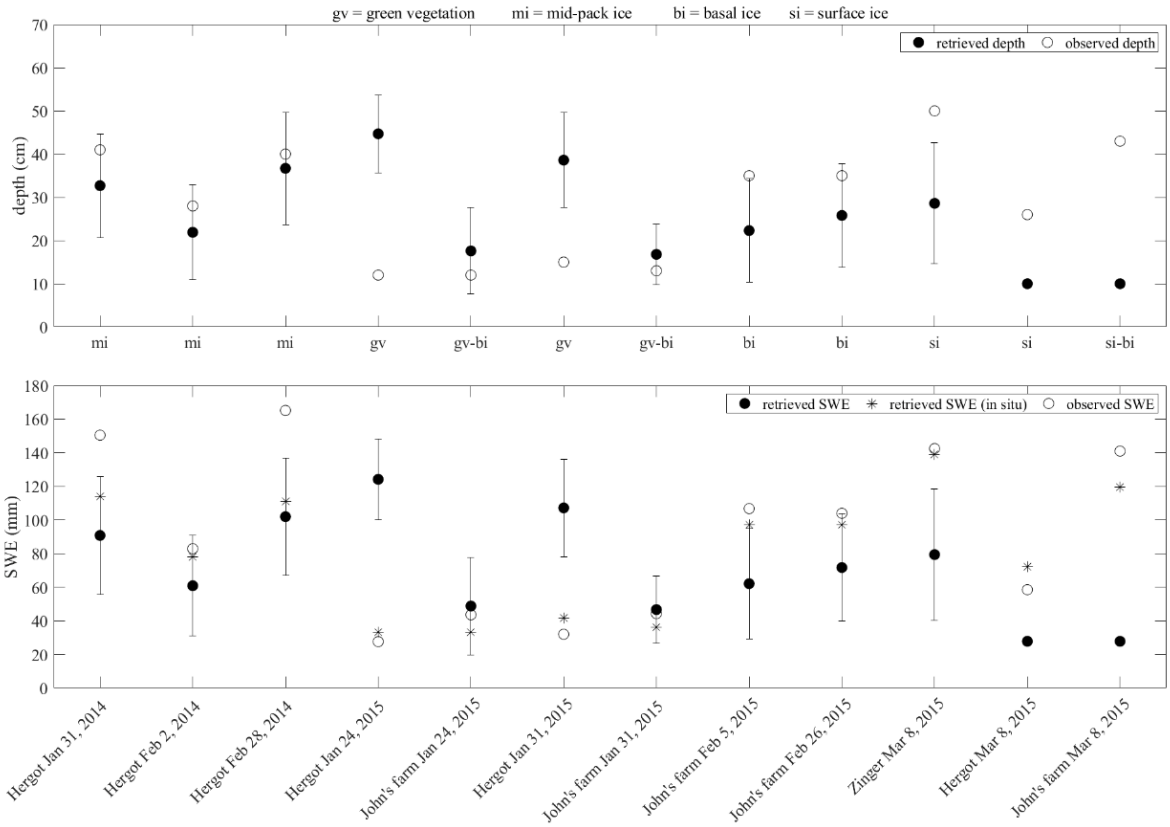

Figure 6-11. Snow depth (top) and SWE retrieval (bottom) of special cases including ice lenses and partially buried vegetation. Bottom panel includes SWE retrieval incorporating in situ snow depth measurements. Error bars represent one standard deviation as described in Figure 6.8 caption.

6.4 Discussion

6.4.1 Validation of the soil-subtraction method

Successful forward modelling and retrieval was dependent on appropriate determination of Φ_{opt} since it has profound control over simulation results. To validate the soil-subtraction method used in Φ optimization described in Section 3.1.2, forward modelling and the retrievals were repeated without the soil-subtraction method. A summary of results is provided in Table 6.7.

Table 6-7. Effects of soil-subtraction method in terms of forward modelled accuracy and retrieval performance.

Soil-subtraction (yes/no)		yes	no
Forward modelling	R_{avg}	0.69	0.75
	$RMSE_{avg}$ (dB)	2.27	1.94
Maryhill retrieval RMSE	SWE (mm)	21.9	27.5
	depth (cm)	5.2	8.3
Englehart retrieval RMSE	SWE (mm)	24.6	30.9
	depth (cm)	7.8	10.8
Maryhill Φopt	n-layer	1.2	1.0
	1-layer	1.3	1.1
Englehart Φopt	n-layer	1.5	1.5
	2-layer	1.6	1.7

Forward accuracy improved without soil-subtraction, yielding R_{avg} = 0.75 ± 0.10 and an $RMSE_{avg}$ = 1.94 ± 0.75 dB whilst retrieval accuracy decreased. When soil-subtraction was implemented, RMSE for the SWE and snow depth retrievals improved by 5.6 mm and 3.1 cm in Maryhill, and by 6.3 mm and 3.0 cm in Englehart. Without soil-subtraction, Φ was allowed to compensate for errors in soil parameterization along with snowpack parameterization. However, when soil-subtraction was used, Φ was restricted to compensating for errors in snowpack parameterization thereby providing more appropriate scaling of the microstructure parameter; this improved retrieval accuracy at the expense of forward skill, while demonstrating the importance of acquiring snow-free, frozen-ground observations.

For the Maryhill sites, Φ_{opt} = 1.0, in the forward n-layer parameterization without soil-subtraction, which indicated an apparent perfect agreement between simulated and observed scattering while Φ_{opt} = 1.2 with the soil-subtraction method, suggesting an underestimation in simulated scattering. If snowpack scattering was underestimated in Maryhill, in order to achieve Φ_{opt} of unity in the forward n-layer parameterization, the soil scattering must have been proportionally overestimated in compensation. A difference in Φ_{opt} of 0.2 was also noted for the 1-layer Maryhill parameterizations. It was unclear how much of the overestimation of soil backscattering could be attributed to the model, *in situ* observations, or the optimization of *h*. For the Englehart sites, the snow accumulation apparently masked much of the background scattering since Φ_{opt} = 1.5 in the forward n-layer parameterization with and without soil-subtraction. Given the limited effects of background scattering, a difference in Φ_{opt} of 0.1 for the Englehart 2-layer parameterization was therefore attributed to the snowpack parameterization and not an overestimation of background scattering. Variation in Φ_{opt} with and without soil-subtraction therefore helped to explain why the optimum retrieval configuration in Maryhill retained *h* as a free parameter, where it had more influence, whilst in Englehart *h* was assigned the optimized value of 1.4 cm. Overestimation of soil scattering at the Maryhill sites also accounted for the limited

sensitivity in forward model simulation noted in Figure 6.7. This may, in part, be due to neglecting ε''_{soil} in the calculation of soil reflectivity in (1) and (2).

6.4.2 Snowpack parameterization

Optimal snowpack parameterization schemes provide insight into the drivers of snowpack scattering at the Maryhill and Englehart sites. Although numerous and varied snow layers were observed at the Maryhill sites, a single-layer parameterization scheme provided the nearest match in terms of Φ_{opt} to the n-layer scheme. A difference in Φ_{opt} of 0.1 indicated little difference in simulated scattering between the n-layer and 1-layer schemes. This provided evidence of minimal radar sensitivity to physical and radiometric dissimilarity between snow layers at these sites. Although Maryhill snow pits featured an average of 6 layers, they were not sufficiently distinct to affect the radar response. Two- and three-layer schemes both resulted in $\Phi_{opt} = 1.5$ which meant that additional layers failed to improve the simulation. Single-layer parameterizations have been used where there was insufficient stratigraphic definition in the snowpack (eg. Lemmetyinen et al., 2018).

The single-layer scheme performed the poorest for the Englehart sites which suggested a layer response in the signal. The dual-layer scheme performed best, followed by the three-layer scheme. The dual-layer scheme was conceptualized to represent depth hoar and wind slab since these have a distinct and contrasting radar response wherein depth hoar enhances scattering while wind slab attenuates it (King et al.2018; Rutter et al., 2019); other snow types have a less-distinct response and were aggregated with wind slab in the optimization. Dual-layer parameterizations have been successfully used in Tundra environments where distinct differences between depth hoar and wind slab exist (King et al 2018). In the taiga snow class, limited distinction between layers is common (Lemmetyinen et al 2018) however taiga snow is generally found amidst forest, sheltered from aeolian processes (Sturm et al., 1995). Despite the taiga classification, Englehart sites were exposed and developed wind slab, so a dual-layer scheme was appropriate. The three-layer scheme performed slightly worse while adding retrieval complexity, so it was not selected.

6.4.3 Retrieval configuration and limitations

The optimal Maryhill retrieval configuration retained h and p_{ex} as constrained free parameters while constraining bulk snow density to its mean value. From the Φ optimization it was apparent that background scattering influenced the radar response in Maryhill. This interpretation was further supported by the inclusion of h as a free parameter in the optimal Maryhill retrieval, allowing adjustment of background scattering. It was unsurprising that p_{ex} was retained as a free parameter in the retrieval since microstructure has been identified as a strong contributor to snowpack scattering (Chang et al., 2014; Tsang et al., 2007) and, along with snow density, is among the most influential input parameters in MEMLS (Proksch et al., 2015). Despite the importance of density

in MEMLS, it varies conservatively in southern Canada (Brown, 2000) therefore constraining it to its mean value for the retrieval was reasonable.

The optimal Englehart retrieval configuration retained mean values for each parameter except p_{ex} of the wind slab layer. The retention of mean values in the retrieval was realistic since the Englehart observations occurred over four consecutive days; substantial deviance from mean values was neither expected nor was it observed. Retention of wind slab p_{ex} as a free parameter emphasized the relative importance of microwave attenuation in wind slab at 17.2 GHz. The retrieval was therefore driven by wind slab p_{ex}, which effectively moderated scattering from the depth hoar layer.

Optimal Maryhill retrieval performance was achieved when minimum snow depth was constrained to 10 cm. The overestimation of soil scattering discussed in Section 5.1 provided a plausible explanation. At shallower snow depths there was insufficient snow volume to mask the background contribution so, without the constraint, the retrieval algorithm minimized snow depth in compensation for excessive background scattering, which resulted in underestimation of snow depth and SWE. This tendency diminished with snow accumulation and was particularly apparent for the Maryhill sites which included early-season and low-accumulation observations. Similar results would likely occur for early-season Englehart sites too, however, with the observed snow depths exceeding 50 cm, the snow accumulation was sufficient to mask background scattering, explaining why the constraint was ineffective at Englehart sites. Constraining minimum snow depth to 10 cm mitigated overestimation of soil scattering in Maryhill, but it would contribute its own error for snow depths less than 10 cm. Assuming mean snow density in Tables 6.4 and 6.5, this method would produce a maximum error of about 28 mm and 27 mm SWE for Maryhill and Englehart, respectively, for snow depths less than 10 cm.

Uncertainty in the parameterization of p_{ex} in both Maryhill and Englehart retrievals was attributed to the subjective nature of the D_{max} observations used in this study and the conversion from D_{max} to p_c. It has been established that D_{max} observations may be unreliable (Mätzler, 2002), however, the retrievals had sufficient flexibility to partially accommodate for these errors. Use of an Ice Cube or snow micropenetrometer to make objective, repeatable, and accurate estimations of p_c would improve confidence in microstructure constraints and potentially improve retrieval results.

Mitigation of errors that influenced the retrieval of h in Maryhill sites was a concern. Errors included dissimilarity in soil surface structure between sites, and treatment of the soil surface during snow excavation. While snow-free UWScat observations were made at several sites, these might not have been fully representative of all sites. This effect was mitigated to some extent by similarity in crop and soil treatment, however, it was likely that differences existed between sites. During snow excavation, field technicians worked in the radar FOV for several hours while removing snow with shovels. This fractured snow grains and compacted residual snow into a hard layer filling in natural hollows and furrows in the soil surface. Shovelling also modified the soil structure by

breaking tops of ridges in the soil resulting in a relatively flat, hard-packed surface. This could have modified the apparent roughness of the soil surface but was unavoidable.

6.4.4 Retrieval error

The SWE retrieval error for each Maryhill datapoint fell within the 30 mm limit except for the February 5, 2015, Hergot datapoint where SWE was overestimated by 45 mm (refer to Figure 6.8); an associated error was not apparent in the snow depth retrieval. The identified cause was that alfalfa stems were captured in the density cutter causing a loss of snow sample resulting in an underfilled density cutter, and therefore an underestimated snow density. A snow density of 185 kg/m^3 was recorded for the site which undermeasured the mean observed snow density (278 ± 52 kg/m3) by nearly two standard deviations. Using the mean observed snow density in place of the *in situ* density for the February 5, 2015, Hergot datapoint (Figure 6.12) improved overall accuracy of the Maryhill sites from an RMSE of 21.9 mm to 14.7 mm SWE. Incorporating this correction with *in situ* snow depths in the retrieval resulted in an RMSE of 6.8 mm SWE.

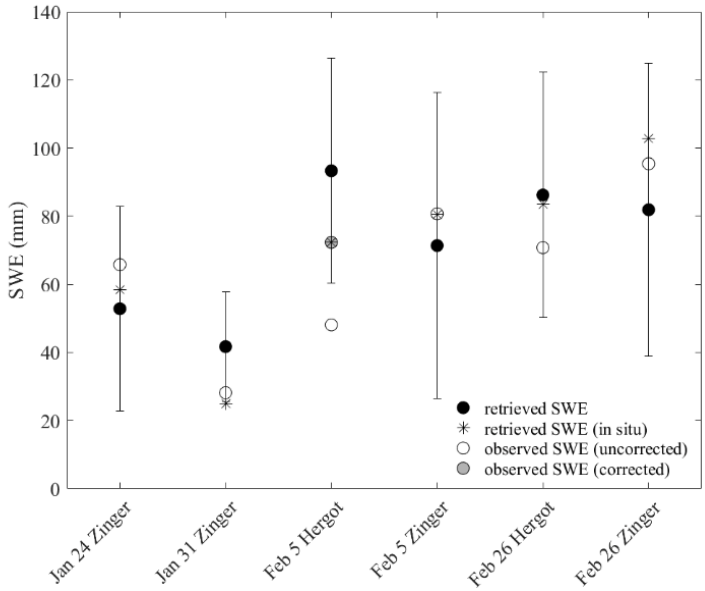

Figure 6-12. Improved Maryhill retrieval accuracy by using mean snow density in place of anomalously low in situ density measurement at the Hergot site on February 5. Error bars represent one standard deviation as described in Figure 6.8 caption.

Underestimation of SWE and snow depth was noted for site e2 on February 17, 2015, in Englehart (refer to Figure 6.9). This datapoint coincided with the greatest snow depth and SWE of the study, 67 cm, and 192 mm, respectively which suggested a potential loss of sensitivity. Wind slab was present at the Englehart sites, and its attenuating effects may help explain the apparent reduction in microwave sensitivity at some sites to increasing snow depth and SWE. Accretion in the form of wind slab can mask increases of SWE in the radar signal (King et al., 2018), thereby

resulting in a negative bias of the snow depth retrievals for those sites where wind slab was present. However, negative bias in the Englehart SWE retrievals was inconsistent. Uncertainty in density sampling may account for this since field notes from Englehart consistently described cohesionless depth hoar which can lead to less accurate measurements (Vargel et al., 2020); excluding site e2 on February 17, maximum bias of the Englehart SWE retrievals was less than 13 mm SWE.

Mid-pack and basal ice layers were associated with an underestimation of depth and SWE, which was corrected using *in situ* depth measurements, except for January 31, 2014, and February 28, 2014. These dates featured the greatest *in situ* bulk density of all sites tested in the retrieval at 367 kg/m^3 and 413 kg/m^3, respectively. A density of 917 kg/m^3 was assigned to ice layers where ice was identified in field measurements but could not be sampled with the density cutter, which resulted in elevated bulk snow densities particularly at these two sites which featured multiple ice lenses; this contributed to a substantial mismatch between ground-referenced SWE and retrieved SWE. Excluding ice in the calculation of bulk snow density in ground-referenced field observations improved overall accuracy for sites with ice lenses and partially buried vegetation from an RMSE of 60.4 mm to 52.2 mm SWE. Incorporating this correction with *in situ* snow depths in the retrieval resulted in an RMSE of 12.4 mm SWE. This correction is shown in Figure 6.13.

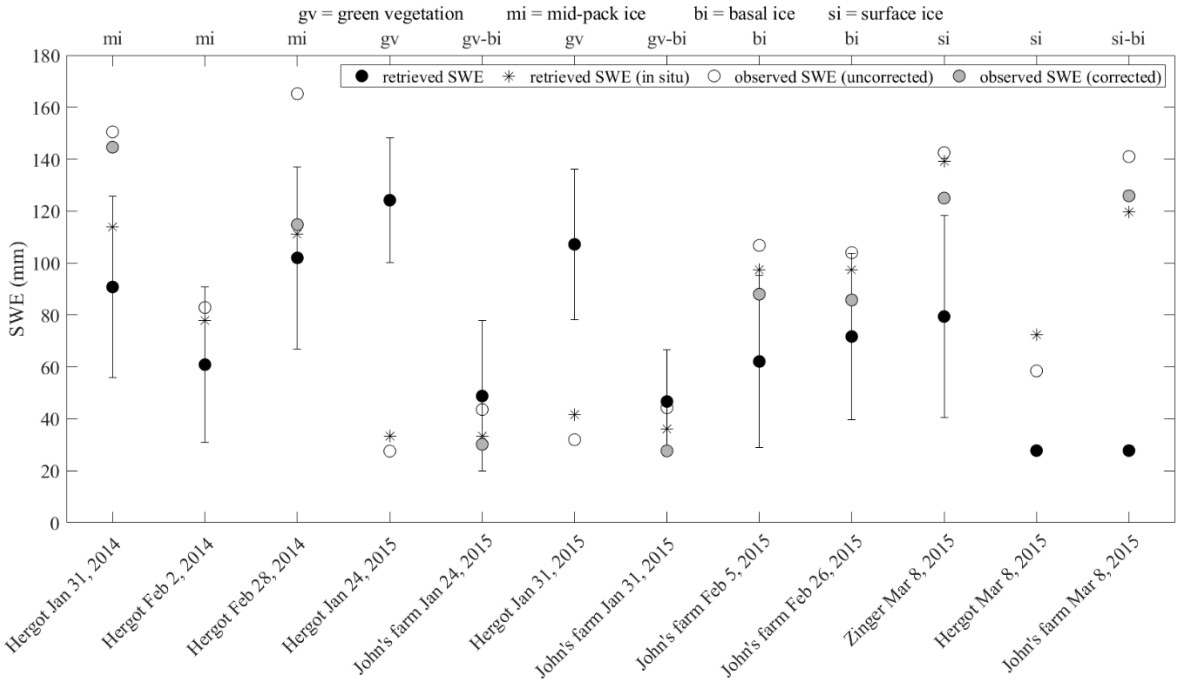

Figure 6-13. SWE retrieval of special cases with ice lenses, where present, excluded from bulk snow density calculations of ground-referenced field observations used to evaluate retrieval accuracy. Error bars represent one standard deviation as described in Figure 6.8 caption.

A combination of partially buried vegetation and basal ice lenses resulted in good accuracy in both depth and SWE retrievals at John's farm on January 24, 2015, and January 31, 2015.

Enhanced backscatter from the partially buried vegetation at the site likely countered the effects of the backscatter reduction associated with ice lenses, resulting in parity between retrieved and observed SWE, however, this was coincidental.

These errors highlight the importance of robust *in situ* measurements and underscore the importance of effective model constraints. Given that sampling occurred across a spatial and temporal gradient and observations were located within metres of the radar FOV, this generally provided confidence in the constraint of retrieval parameters.

Although noise was observed across the range of incidence angles (refer to error bars in Figures 6.8 through 6.11) an angular response was not observed in the SWE retrieval results at most sites, including those with vegetation. Noise in the retrieval results was driven in part by UWScat system noise and in-scene variability of snow and soil properties but the contribution of each was not clear. The Mann-Kendal test identified significant angular influence on retrieved SWE at the Zinger site on 01/31/2015 and at John's farm on 01/24/2015 as shown in Figure 6.14. It is not clear what controlled the angular response observed at the Zinger site as other sites with similar levels of SWE did not generate a similar response; this may be attributed to a non-visible feature within the soil or snow present in the FOV. The angular response at John's farm on 01/24/08 was attributed to forward scattering at the snow-ice interface. This effect was present with 12 cm of snow accumulation, but it diminished with further accumulation at this site on later dates. Although vegetation was present at this site it was partially covered by the basal ice layer and did not inflate retrieved SWE to the same extent observed on this date at the Hergot site. Wet surface ice lenses produced an invariant response as shown in Figure 6.14 for the Hergot site and John's farm on 03/08/2015. This supports the assertion that specular reflection at the air-ice interface resulted in forward scattering, minimizing the signal received by the antenna. The energy that was backscattered was insufficient to drive the retrieval beyond the minimum snow depth constraint of 10 cm implemented in the Maryhill retrieval scheme; noise in the retrieval was eliminated by minimum snow depth constraint. A similar response was not observed at the Zinger site on this date despite the presence of a surface ice lens. The Zinger site measurement occurred in the morning when air temperatures were colder and the ice surface appeared drier, with less observable melt thereby limiting specular reflection at the ice-air interface. Instrument noise is unavoidable while in-scene variability at the scale of a ground-based instrument with a finer spatial resolution may have less impact once aggregated in a space-borne retrieval scheme with coarser spatial resolution.

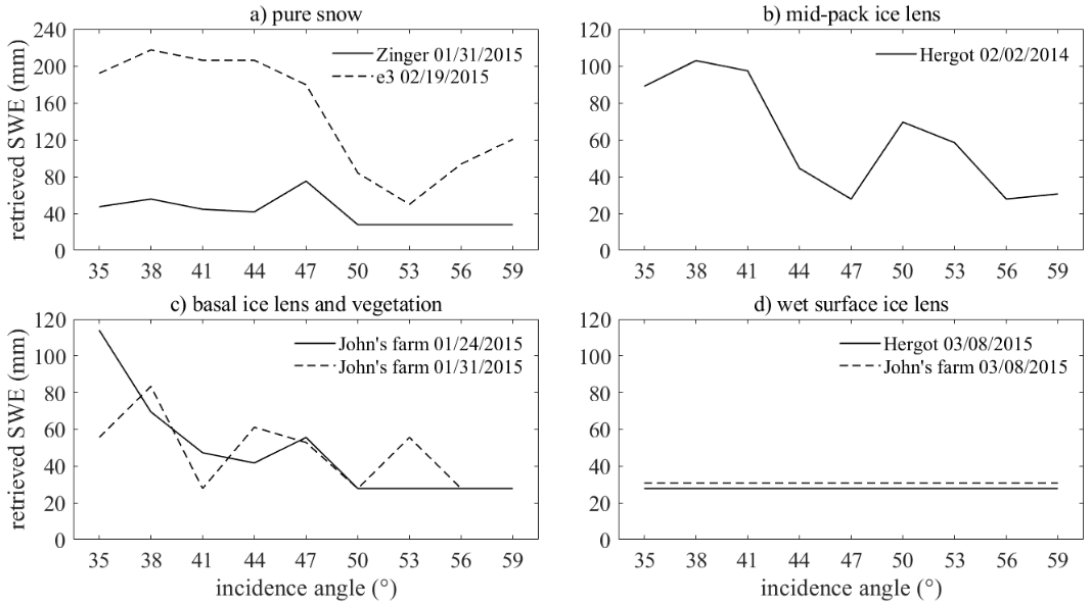

Figure 6-14. Effects of incidence angle on retrieved SWE for selected sites. Trends were detected in a), b), and c). Invariant response shown in d).

6.4.5 Improvements and implementation

It was expected that retrieval accuracy would improve when *in situ* snow depths were used to constrain model parameterizations, given that field measurements were made within metres of the UWScat FOV. Given the snow depth correlation length of around 26 m, it was not surprising that snow depths measured at the local and regional scales reduced accuracy. This is an important consideration for airborne and spaceborne applications since ground referencing strategy must match the spatial resolution of the radar instrument with the correlation length of snow properties. Ground referenced data beyond this range should be avoided.

The similarity in snow depth correlation length at Maryhill and Englehart sites was due, in part, to the similarity in physical characteristics of the sites. The soil had been managed in a similar fashion with the same crop at a similar stage of desiccation. The rectilinear fields were bounded by trees, hedges, ditches, and buildings which comprised the landscape that contributed to snow parameter constraint. For this reason, the methods contained herein should be applied with caution outside of mid-latitude agricultural fields since these landscapes produce constraints unique to an agricultural environment and are likely more consistent than those found in a natural environment.

While ground-based instruments with fine spatial resolution would be sensitive to variation of snow depth over short distances, a space-borne instrument would likely feature much coarser resolution, so it may not be possible resolve spatial variation in snow depth at a scale approaching the observed correlation length of snow depth at these sites. Therefore, the effect of the spatial variability of snow depth on space-borne retrievals would depend on the spatial resolution of the instrument. The microwave response to snow depth would thus be an aggregation of response to

sub-resolution snow depth variability. However, given the replication of snow depth and its spatial variability across different fields (refer to Figure 6.2), a space-borne retrieval may retrieve similar levels of SWE for similar fields in areas subject to the same meteorological inputs which may provide some constraint on retrieved SWE.

Study of snow property distribution (ie. snow depth, density and p_{ex}) in mid-latitude agricultural fields should be continued. This will improve confidence in parameter constraints leading to improvement in retrieval accuracy. Combining snow models with land surface models may provide additional confidence in model constraints, especially in regions where *in situ* measurement is impractical. Furthermore, this should be completed at a scale appropriate for airborne and spaceborne implementation.

A more robust characterization of *h* in agricultural fields must be incorporated in future studies. With a limited dataset, we found that *h* contributed around 2.6 dB of uncertainty while the model demonstrated only 3 dB of sensitivity. Distributed *in situ* measurements of soil roughness would better constrain *h* and minimize uncertainty. Leveraging spatio-temporal consistency in agricultural soil management for different crop types could provide a means to estimate *h* over large distance scales, especially useful for spaceborne retrievals. Incorporating the soil subtraction method discussed in this paper, where snow-free observations of frozen ground are available, will also help mitigate uncertainty in *h* since the influence of soil is subtracted from both the observation and the model prediction in the optimization of an appropriate Φ.

It is important to recognize that typical radiative transfer models of snow do not account for the effects of partially buried vegetation or contiguous ice lenses in their predictions. The results in Figure 6.11 illustrate the influence of these confounding factors. The effects of partially buried vegetation are a concern early in the season before the vegetation has desiccated and plant height exceeds snow accumulation, particularly in the presence of a roughened snow surface and coarse melt-form snow grains. The combination of a rough surface, larger snow grains, and green vegetation can enhance backscatter resulting in overestimation of snow depth and SWE, although it was unclear which condition had the greatest influence. Mid-pack and basal ice lenses result from rain and melt-refreeze events which may occur throughout the season and were associated with an underestimation of SWE. Freezing rain is most common in the early- and late-season, however, it may occur throughout the winter in mid-latitude regions. Melting surface ice layers were associated with a decrease in backscatter likely due to enhanced specular reflection (Thompson et al., 2019) which resulted in an underestimation of snow depth in the retrieval. With increased likelihood of rain-on-snow events at high latitudes (Liston and Hiemstra, 2011), this could have important implications for northern retrievals.

Operationalizing these retrieval schemes will require identification of these unique features in order to determine appropriate parameter constraints in the retrieval. *In situ* measurements are an obvious way to constrain the retrieval parameter ranges but with clear limitations on practicality at

the global scale. Other methods may also be applicable in this regard. For example, polarimetric tools such as polarization signatures, pedestal heights, phase difference, and decompositions (eg. McNairn et al., 2002; Thompson et al., 2019; Thompson and Kelly, 2019) may be able to identify green vegetation which tends to depolarize incident microwaves. Passive microwave remote sensing could be used to identify surface ice lenses by monitoring changes in H-polarized brightness temperature associated with their presence (eg. Rees et al., 2010); weather data could be used to corroborate. Models such as SNOWPACK or CROCUS may be able to predict ice lenses in limited situations (Bartelt and Lehning, 2002; Brun et al., 1992, Langlois et al., 2009).

6.4.6 Influence of incidence angle on retrieved SWE

The SWE retrieval algorithm was driven primarily by the observed power response of UWScat. Elevated backscatter generally yielded elevated values of retrieved SWE while reduced backscatter yielded reduced SWE. This was true whether the change in backscatter was due to snow accumulation, inclusions, or random system noise. These features generated variability in retrieved SWE across all incidence angles for most sites as indicated by the error bars in Figures 6.8 through 6.12. Trends within the variability could indicate influence on retrieved SWE from incidence angle. To test for significant trends, we used a modified Mann-Kendall test following Hamed and Rao (1998) which accounted for autocorrelated data. At most sites, there was no apparent trend between retrieved SWE and incidence angle. Those sites where a trend was detected are identified in Figures 6.14a, b, and c.

The only pure snow sites to exhibit a trend were the Zinger site (January 31, 2015) and e3 (February 19, 2015) shown in Figure 6.14a, corresponding with snow depths of 9 cm and 55 cm, respectively. With no observed vegetation, ice lenses or other abnormalities, causation at both sites was unclear. The relative lack of variability in retrieved SWE at these sites suggested a physical influence that diminished with increasing incidence angle, instead of instrument noise. The weaker trend at the Zinger site, which featured shallow snow, suggested an unknown but limited, subnivean influence. The deeper snow at e3, which featured the largest standard deviation of retrieved SWE in the study (refer to Figure 6.9), suggested a stronger influence within the snowpack. The shape of the e3 response was similar to that of other scenes with buried ice lens (eg. Figure 6.14b and c) so it seemed plausible that an unobserved ice lens was present in the FOV at e3.

The Hergot site on February 2, 2014 (Figure 6.14b) featured a mid-pack ice lens at 6 cm within a 28 cm snowpack (refer to Figure 6.4). Mid-pack ice layers were also present at Hergot sites on January 31, 2014, and February 28, 2014, but neither of these sites exhibited a similar trend in retrieved SWE. However, these sites featured snow depths of 41 cm and 40 cm, respectively, suggesting snow accumulation eliminated the effect. The response at John's farm (Figure 6.14c) became noisier, with a less apparent trend, as accumulation increased from 12 cm on January 24, 2015, to 13 cm on January 31, 2015. By February 5, with 35 cm of snow depth, the trend was no

longer detectable. Although vegetation was present at John's farm, the angular response seemed to be dominated by the ice lens since no trends were apparent at other sites with similar vegetation but no ice lenses. The reason for this is not known, however, different vegetation conditions may have contributed. Vegetation was less dense at John's farm, where much of the smaller green growth was suppressed by the ice lens; vegetation remained unrestricted at the Hergot site. The similar shape of the responses in Figures 6.14b and 6.14c and relatively low snow accumulation suggested an association with buried ice lenses, which were present at each of these sites and may have contributed to forward scattering as the incidence angle increased. This effect seemed to diminish with further snow accumulation while increased variability in retrieved SWE across all incidence angles became more apparent.

Wet surface ice lenses produced an invariant response as shown in Figure 6.14d for the Hergot site and John's farm on March 8, 2015 (sites have identical retrieved SWE but curves have been vertically offset for clarity). This supported the assertion that specular reflection at the air-ice interface resulted in forward scattering, thus minimizing the signal received by the antenna. Low levels of backscatter were insufficient to drive the retrieval beyond the minimum snow depth constraint of 10 cm implemented in the Maryhill retrieval scheme which resulted in a retrieved depth of 10 cm at both sites and eliminated variability from the retrieval. This was reflected in large underestimations of SWE at these sites (refer to Figure 6.11). A similar response was not observed at the Zinger site on this date despite the presence of a surface ice lens and a notable underestimation of SWE in Figure 6.11. The Zinger site measurement occurred in the morning when air temperatures were colder and the ice surface appeared drier, with less observable melt apparently reducing the specular reflection at the ice-air interface.

While In-scene variability at the scale of a ground-based instrument with fine spatial resolution had a demonstrable impact on SWE retrieval accuracy. The impact of such features may be dampened once aggregated in a space-borne retrieval scheme where the scale of the physical phenomena is less than the spatial resolution of the instrument. However, buried ice lenses could produce moderate effects in space-borne retrievals if the phenomena were large relative to spatial resolution although their effect seemed to diminish as snow accumulated. Widespread wet surface ice lenses, such as those following a regional freezing rain event, could produce a strong effect and should be avoided while wet, and until sufficient snow accumulation has buried the ice. Vegetation at these sites produced no observed effect on the relationship between retrieved SWE and incidence angles.

6.5 Conclusion

Radar observations of snow at 17.2 GHz in mid-latitude agricultural fields were combined with coincident *in situ* snowpack observations to successfully demonstrate forward modelling skill using MEMLS. Separate retrieval algorithms were developed for Maryhill and Englehart. The optimal

Maryhill SWE retrieval achieved an RMSE of 21.9 mm SWE and was accomplished with a single layer parameterization in which bulk snowpack density was assigned the mean value observed in Maryhill and p_{ex} and h were free parameters constrained by the first standard deviation of all Maryhill observations. Minimum snow depth was constrained to 10 cm due to apparent overestimation of soil scattering. The success of the single layer parameterization provided evidence that the snowpack layers in Maryhill were not radiometrically distinct since they could be simulated with a single layer. The optimal Englehart SWE retrieval achieved an RMSE of 24.6 mm SWE with a dual-layer parameterization in which the only free parameter was wind slab p_{ex}, constrained by the first standard deviation of all observations. Remaining parameters were assigned the mean value of all observations. Constraint on minimum snow depth provided no benefit given snow depths > 50 cm. The wind slab layer moderated backscatter from the underlying depth hoar layer through variation in p_{ex}, which illustrated the radiometric significance of the upper layers of snow in Englehart.

Soil-subtraction improved retrieval results by restricting Φ_{opt} from accounting for soil effects. RMSE improved by as much as 6.3 mm SWE and 3.1 cm snow depth at the expense of forward modelling accuracy. This demonstrated and quantified the efficacy of soil-subtraction and the importance of acquiring radar observations of snow-free, frozen ground in order to constrain background scattering.

The importance of constraining sensitive parameters for retrievals was demonstrated, particularly where ice lenses and partially buried vegetation were present. Using *in situ* snow depths further improved retrieval accuracy for both Maryhill and Englehart, yielding average RMSE values of 12.0 mm SWE and 10.9 mm SWE, respectively; the optimal use of *in situ* data to constrain the retrievals should include measurements made no further from the instrument FOV than the range of spatial autocorrelation. Surface ice lenses and partially buried vegetation had the largest impact on retrieval accuracy, resulting in large under- and over-estimations of SWE, respectively; improved representation of these features in the models is needed. Retrieval accuracy of complex scenes improved using *in situ* snow depths. The largest correction of about 91 mm SWE occurred in the presence of a surface ice lens and partially buried vegetation.

To improve retrieval accuracy, advancement must be made to models and their parameterization in order to accommodate complex scenes. Models must account for pure snow in the simplest case, but they must also be able to account for ice-layered snow and the effects of partially buried vegetation, common in mid-latitude environments. In the meantime, identifying the presence of these features would allow us to better constrain the retrievals. This could be achieved through application of polarimetry, passive microwave remote sensing, and land surface modelling with robust snowpack energy balance representations. In some regions, *in situ* data could better prescribe these constraints but this is a local-scale fix, not a global one.

6.6 Acknowledgements

The authors would like to thank John Nederland and John Vanthof who allowed access to their land for this study. The authors would also like to thank Grant Gunn, Andrew Kasurak, Qinghuan Li, and Vicky Vanthof for their contributions to field data collection.

Chapter 7
Estimating wind slab thickness in a tundra snowpack using Ku-band scatterometer observations

7.1 Introduction

The northern high latitudes have warmed at a rate twice that of the global average (Meredith et al., 2019) and changes to spatiotemporal patterns of snow accumulation are among the ways in which it manifests (Brown and Mote, 2009; Pulliainen et al., 2020). Monitoring of these changes is important from a climate perspective but also from ecological and human survival perspectives as well (Bokhorst et al., 2016). The arctic tundra is characterized in part by exposure to strong winds and cold air temperatures which drive aeolian and thermodynamic snowpack processes resulting in its signature wind slab and depth hoar composition (Sturm et al., 1995). Wind slab consists of small, wind-fractured fragments in a hard-packed, high-density layer while depth hoar underlays and is composed of large, faceted grains whose growth is driven by strong vertical temperature gradients (Colbeck, 1982). Overall, the snowpack is relatively thin, and its depth is largely controlled by topography and vegetation (Derksen et al., 2014).

Radar remote sensing in the Ku-band frequency range has shown promise in the remote estimation of snow water equivalent (SWE), however, recent work in Trail Valley Creek, NT, has found that slab dominated accumulation in tundra snow environments and drift features can diminish sensitivity to SWE at 17.2 GHz (King et al., 2018). The wind slab in this environment was found to have a median density of around 316 kg m-3, a median specific surface area (SSA) of 24 m2 kg-1, and median layer thickness of 22 cm with an overall snow depth of 65 cm (Rutter et al., 2019). Furthermore, a disproportionately large amount of SWE is retained in snow drifts, with as much as 30% of SWE observed over just 8% of the land area in Trail Valley Creek (Pomeroy et al., 1997; Sturm et al., 2001) which poses a substantial challenge to the accuracy of arctic SWE retrievals.

Constraining wind slab thickness in an arctic SWE retrieval would provide a means to mitigate this challenge which is important since understanding layer variability is critical in the characterization of uncertainty in radar-based SWE retrievals (Rutter et al., 2019). To address this need, thirteen fully polarimetric radar measurements were made at 17.2 GHz with the University of Waterloo Scatterometer (UWScat) of tundra snow at Trail Valley Creek during April 2017 and were processed with the Freeman-Durden polarimetric decomposition to isolate the influence of tundra wind slab on double-bounce scattering. Therefore, the objective of this research letter is to introduce and describe the relationship between double-bounce scattering and tundra wind slab thickness, defined as its maximum vertical extent, which can then be used to constrain wind slab thickness in radar-based SWE retrievals in order to improve their accuracy.

7.2 Datasets and methods

UWScat is a fully polarimetric scatterometer with centre-frequencies of 9.6 and 17.2 GHz. The system operates over a series of programmable sweeps in azimuth and incidence angle allowing a customizable field of view. Observations of individual azimuth sweeps are averaged to improve measurement precision and mitigate radar fade. Given the geometry of the observations, range-to-target was within the near-field range of the antenna therefore the near-field gain correction of Sekelsky (2002) was applied. An in-scene reference target and sky observation were used in calibration to characterize system leakage and noise, with total uncertainty estimated to be around ±2 dB following Geldsetzter et al. (2007). UWScat returns backscattered power as a function of incidence angle and slant range for each pairwise combination of send-receive vertical (V) and horizontal (H) polarization (VV, HH, VH, HV) with a range resolution of 30 cm. A covariance matrix is generated from cross-products of the scattering matrix for each incidence angle providing input for the polarimetric decomposition. Further description of the UWScat system can be found in King et al. (2013).

Each UWScat measurement comprised azimuth sweeps of 60° with incidence angles ranging from 25° to 61° in 3° increments. Between April 11 and April 29, 2017, thirteen UWScat measurements were made of the natural tundra snowpack and 5 UWScat measurements were made of bare ground after the snow was manually removed with shovels from the FOV, in order to characterize the background signal.

Where possible, sites were chosen that excluded substantial vegetation from measurement FOV. Sites where plant, shrub and tree heights exceeded snow depth were avoided.

To test for microwave attenuation within the tundra snowpack, a corner reflector (30 cm edge) was systematically observed at a range of depths within a 94 cm snowpack in order to determine at what depth, if any, the corner reflector could no longer be identified. A snow pit was excavated in the FOV which allowed placement of the corner reflector at various depths in the pit face. The snow pit was approached from the side opposite UWScat along a dedicated path to minimize disturbance to surrounding snow. At each position in the snowpack, a measurement spanning the full range of azimuth and incidence angles was made to ensure the manually aligned corner reflector was illuminated. The corner reflector was first placed on the surface of the air-snow interface to demonstrate the maximum power, and then at depths of 60 cm, 30 cm, and 0 cm (ie. the snow-soil interface). Finally, a measurement was made without the corner reflector present. The experiment setup is shown in Figure 7.1.

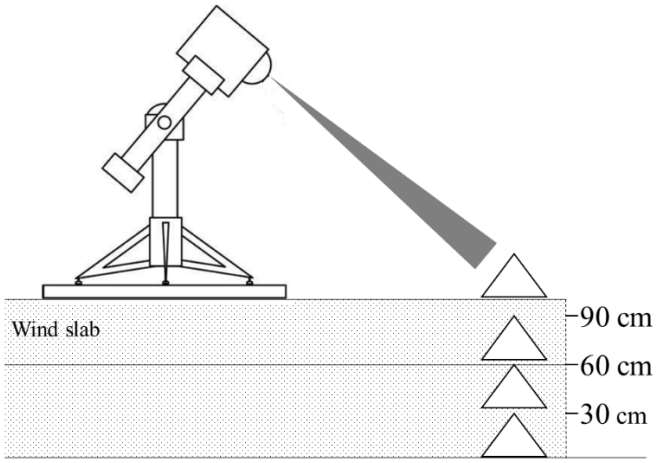

Figure 7-1. Sketch of buried corner reflector experiment. Drawing not to scale.

Coincident and co-located snowpack observations accompanied each UWScat measurement including the buried corner reflector experiment. Following Fierz et al. (2009), snow pit observations included snow depth, density, vertical temperature profile, stratigraphy, and grain size. Snow density was measured with a 100 cm^3 box-type cutter and electronic scale. Real permittivity (ε') of snow was estimated from snow density following Mätzler (1996). Grain size was estimated using a loupe and crystal card with a millimetre grid. The specific surface area (SSA) of snow was also estimated in vertical profiles at each snow pit. The infrared reflectance of snow samples was measured with the Dual Frequency Infrared Integrating Sphere for Snow SSA measurement (DUFISSS; see Gallet et al., 2009) at 1310 nm and was used to derive SSA following the empirical relationships proposed by Gallet et al. (2009). Calibrations were performed with reference targets prior to measurement at each snow pit. Environmental conditions were measured at a nearby meteorological station. It was assumed that the subnivean soil layer was frozen and that its condition remained constant throughout the observation period.

The Freeman-Durden three-component decomposition (FD3c hereafter) given in (1), following from the 3 x 3 covariance matrix, is a physically based polarimetric decomposition developed for use over natural environments, which incorporates elements of the covariance matrix to describe total backscattered power (**T**) as the linear combination of surface (f_s), double-bounce (f_d), and volume (f_v) scattering components (Freeman and Durden, 1998). In (1), * denotes complex conjugation. The resultant system of equations is presented in (2) where <…> indicates ensemble averaging. Terms on the left-hand side are provided from the covariance matrix and represent the real power terms for each polarization (S_{HH}, S_{VV}, and S_{VH}), and the complex HH-VV correlation ($S_{HH}S_{VV}^*$).

$$\mathbf{T} = f_s \begin{bmatrix} |\beta^2| & 0 & \beta \\ 0 & 0 & 0 \\ \beta^* & 0 & 1 \end{bmatrix} + f_d \begin{bmatrix} |\alpha^2| & 0 & \alpha \\ 0 & 0 & 0 \\ \alpha^* & 0 & 1 \end{bmatrix} + f_v \begin{bmatrix} 1 & 0 & 1/3 \\ 0 & 1/3 & 0 \\ 1/3 & 0 & 1 \end{bmatrix} \quad (7.1)$$

$$\langle |S_{HH}|^2 \rangle = f_s|\beta|^2 + f_d|\alpha|^2 + f_v$$

$$\langle |S_{VV}|^2 \rangle = f_s + f_d + f_v$$

$$\langle S_{HH} S_{VV}^* \rangle = f_s\beta + f_d\alpha + {}^{f_v}/_3$$

$$\langle |S_{HV}|^2 \rangle = {}^{f_v}/_3 \quad (7.2)$$

Volume scattering is estimated from f_v which is then subtracted from each equation in (2). The dihedral scattering parameter (α) and the Bragg scattering parameter (β) are assigned based on the residual co-polarized phase indicating dominance of surface or double-bounce scattering; if $\mathrm{Re}(S_{HH}S_{VV}^*) > 0$, surface scatter is dominant and $\alpha = 1$, otherwise double-bounce scattering is dominant and $\beta = 1$ (Freeman and Durden, 1998). The system of equations is solved for remaining parameters. Finally, the contribution of the double-bounce scattering component (P_d) is estimated in (3) and total power is equal to the sum of surface, double-bounce, and volume scattering components.

$$P_d = f_d(1 + |\alpha|^2) \quad (7.3)$$

For further detail on the decomposition method, readers are directed to the source paper (see Freeman and Durden, 1998). Reflection symmetry is assumed, and volume scattering is modelled by a cloud of randomly oriented dipoles. Phase difference between VV and HH terms, used to distinguish double-bounce scattering, is not restricted to ± π, and is therefore better suited to natural targets that characteristically exhibit geometric variability exceeding that of manufactured dihedral reflectors on which double-bounce scattering is modelled (Freeman and Durden, 1998). In order to amplify the double-bounce response, given the reflection symmetry assumption, only the VH term of the cross-polarized scattering contribution was included in the input covariance matrix. FD3c was computed for each UWScat measurement, at all incidence angles, and the results were normalized, expressing each scattering mechanism as a proportion of total power.

7.3 Results and discussion

Averaging *in situ* measurements across all sites, wind slab layers were found to be 18 ±12 cm thick with a density of 380 ±42 kg m-3, comprised of fine snow grains with an SSA of 25 ±8 m2 kg-1. Average snowpack depth was 50 ±23 cm. Despite covering a smaller domain within Trail Valley

Creek, these conditions compared favourably with recently published snowpack measurements from 2013 and 2018 (see Rutter et al., 2019). This demonstrated the current stability of snowpack conditions year over year in this region and confirmed the following results were acquired over typical winter conditions.

Figure 7.2 illustrates positive linear relationships, significant at the 0.05 level, between wind slab thickness and the proportion of double-bounce scattering (p_{double}) for incidence angles ≥ 46°, with a maximum correlation of r=0.88 at 61°. At incidence angles <46° relationships lacked significance and strength, with r <0.60. Correlation generally increased with incidence angle. Using the linear relationships generated at each incidence angle in Figure 7.2, slab thickness was estimated from p_{double} and compared to observed values. The RMSE from wind slab thickness estimates are given in Figure 7.2 and ranged from 6.0 cm at 61° to 10.15 cm at 46°. The most accurate estimation occurred at 61°, and is given in (7.4) where ϵ denotes uncertainty:

$$\text{wind slab thickness} = 0.6506(p_{\text{double}}) + 4.1854 + \epsilon \tag{7.4}$$

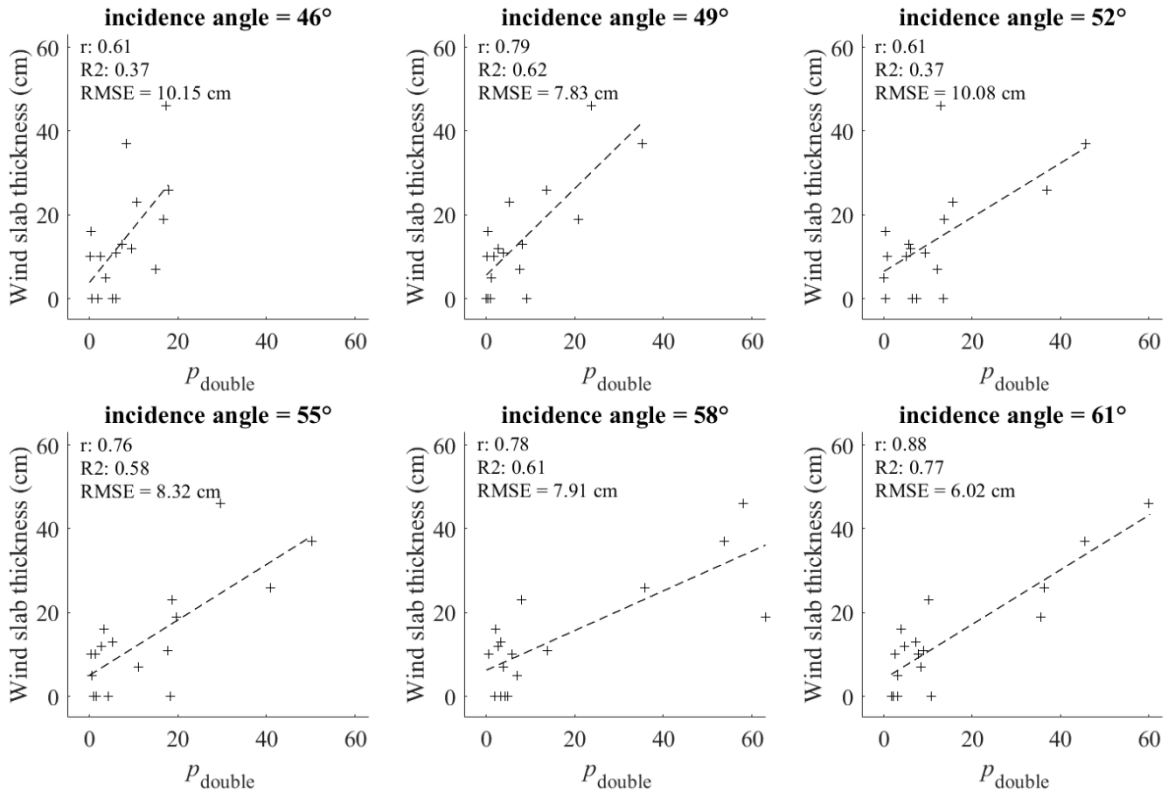

Figure 7-2. Linear relationship between wind slab thickness and pdouble. The values of r, the coefficient of determination (R2), and RMSE are for the estimates of the wind slab thickness derived from the value of p_{double}.

Figure 7.3 illustrates an association between wind slab thickness and p_{double} across all incidence angles. Where wind slab thickness ≤ 16 cm, and for snow free observations, a weak p_{double}

response was observed, however, where slab thickness ≥ 19 cm, p_{double} increased in a similar manner to observations in Figure 7.2. Double-bounce scattering appears to increase approximately at the expense of surface scattering which suggests a conversion from surface scattering at the wind slab-depth hoar interface in thicker wind slab layers. No trend was evident in volume scattering across incidence angles.

The apparent influence of both incidence angle and slab thickness on p_{double} indicated a path length response; path length through a layer is measured as slant range and increases with incidence angle and layer thickness. Indeed, the greatest path length through a wind slab layer without an observed p_{double} response (16-cm slab at 61°, ε'=1.7) was 21.6 cm while the shortest path length through a wind slab layer yielding a p_{double} response (19-cm slab at 46°, ε'=1.7) was 22.8 cm; the lack of overlap between these path lengths is not surprising. For this particular snow environment, an apparent path length threshold existed between a wind slab layer thickness of 16 cm and 19 cm beyond which a stronger, incidence angle-dependent p_{double} response was observed. We attribute this threshold to the ability of UWScat to resolve the wind slab layer with limited influence from subordinate snow and soil layers.

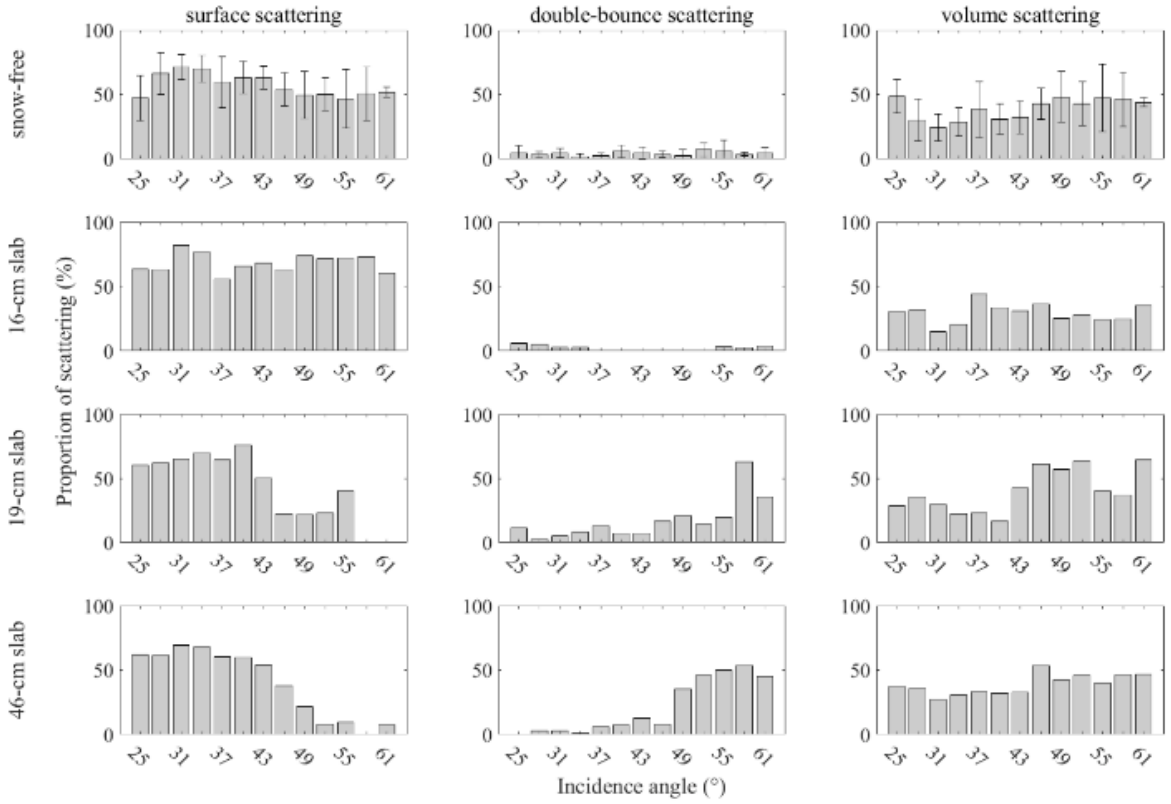

Figure 7-3. FD3c results for snow-free ground, 16-cm slab, 19-cm slab, and 46-cm slab from top to bottom. Surface, double-bounce, and volume scattering from left to right. Error bars on snow-free results are ± 1 standard deviation over four averaged snow free observations.

The ranging capability of UWScat was used to assess the relationship between primary radar response and snowpack stratigraphy. At smaller incidence angles, the primary response

occurred at or near the snow-soil interface. As incidence angle increased, particularly for thicker snowpacks, the primary response shifted upwards in the snowpack towards the air-snow interface. Figure 7.4 illustrates the combination of wind slab thickness and the initial incidence angle for which the primary response emanated from wind slab. This located the primary response within the wind slab layer at incidence angles as small as 34° for sites where wind slab was 46 cm thick. Thus, the p_{double} response can be isolated to within the upper region of the snowpack for the combinations of incidence angle and wind slab thickness indicated in Figure 7.4.

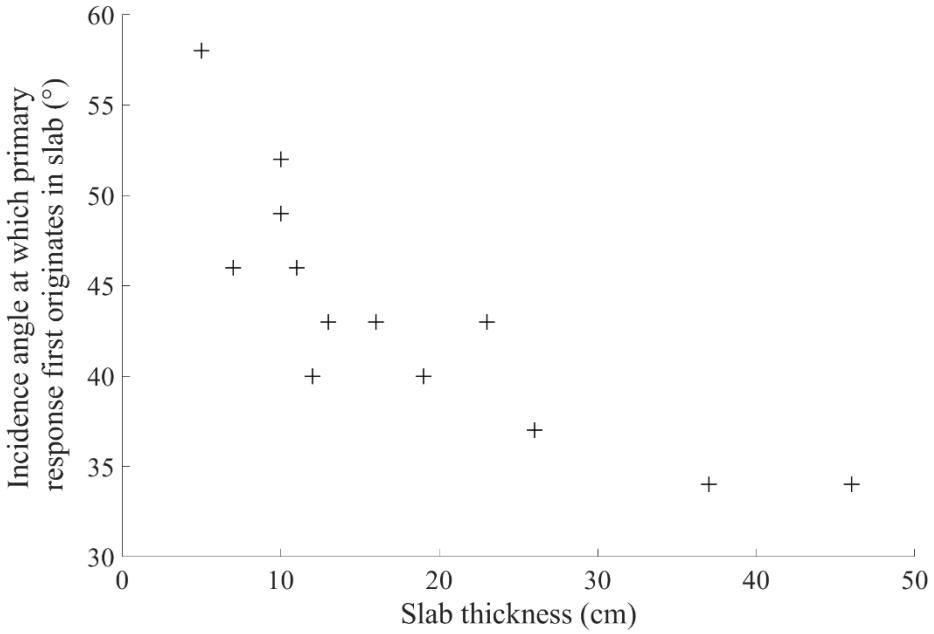

Figure 7-4. Incidence angle at which the primary response first originates in wind slab for a given wind slab thickness.

The buried corner reflector experiment supported the assertion that the primary response, particularly for thicker wind slab layers and at greater incidence angles, emanated from the upper region of the snowpack, near the wind slab layer. At 17.2 GHz, there was insufficient penetration to locate the corner reflector at the base of the 94 cm-thick snowpack with an estimated 43° incidence angle (refer to Figure 7.5). This correlated to a path length of about 94 cm from the air-snow interface to the vertical midpoint of the corner reflector located at the base of the snowpack. Considering the estimated path lengths through each layer of the same snowpack, given in Table 7.1, the 17.2 GHz signal would have been unable to fully penetrate this snowpack at incidence angles ≥ 43° since the distance to the snow-soil interface exceeded 94 cm at these incidence angles. An incidence angle < 43° would have been required to fully penetrate this snowpack although it was unclear from this experiment which specific geometry would have been necessary to do so. Furthermore, microwave energy would not have reached the depth hoar layer at incidence angles ≥ 49°. It was likely that wind slab layers were fully penetrated at each incidence angle, while

sensitivity to subordinate layers diminished with increasing incidence angle as the requisite path length to fully penetrate those layers would have exceeded the observed penetration capabilities. This result also demonstrated that for thicker wind slab and larger incidence angles, there was diminished contribution from subordinate snow and soil layers which improved model performance. As a consequence, in such conditions the relationship is mostly independent of depth hoar layer thickness and therefore overall snowpack depth since the response originates primarily in the wind slab.

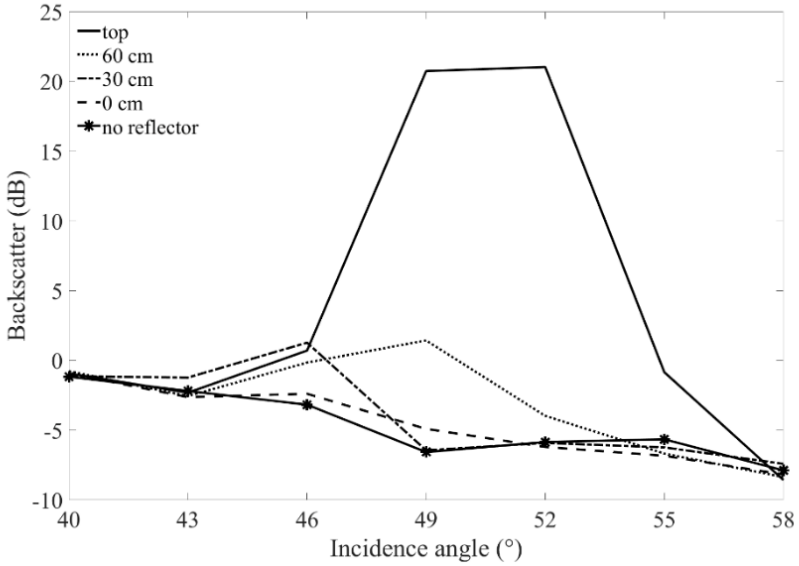

Figure 7-5. Buried corner reflector response in a 94 cm-thick snowpack. Divergence between the 0 cm and no reflector lines was attributed to UWScat measurement uncertainty.

Table 7-1. Calculated slant range distances (cm) of complete layer penetration at each incidence angle. Vertical extent of each layer provided under pos. Distances ≤ 94 cm can be fully penetrated at 17.2 GHz.

incidence angle	new/rounded layer (75 cm - 94 cm)	wind slab layer (41 cm - 75 cm)	rounded layer (18 cm - 41 cm)	depth hoar layer (0 cm - 18 cm)
25°	20	56	81	100
28°	21	57	82	101
31°	21	58	83	103
34°	21	59	85	105
37°	22	60	86	107
40°	22	61	88	110
43°	23	63	90	112
46°	23	64	93	115
49°	24	66	95	118
52°	25	68	97	121
55°	25	69	100	125
58°	26	71	103	128
61°	27	73	106	132

Our interpretation of the scattering interactions for a snowpack exceeding 19 cm in depth, with an existent depth hoar layer, is illustrated in Figure 7.6. Where the primary radar response originates from wind slab layers, we interpret these results to indicate greater likelihood that a second scattering event is encountered, following a surface-bounce at the wind slab-depth hoar interface, thus converting to double-bounce scattering (*b* in Figure 7.6). As shown in Figure 7.3, these interactions are relatively sparse compared to the surface (*a* and *d* in Figure 7.6) and volume scattering mechanisms (*c* in Figure 7.6). Where deeper penetration encounters depth hoar (*c* in Figure 7.6) higher-order volume scattering is likely to occur (King et al., 2015), thereby making a negligible contribution to the double-bounce tally. Likewise, single-bounce scattering at the air-snow interface (*d* in Figure 7.6) will not encounter a second scattering event mid-air and will therefore not contribute to double-bounce scattering. Ground interaction is not depicted in Figure 7.6 since microwave energy reaching the ground must transit the depth hoar layer twice, thus converting most of surface or double-bounce scattering occurring at the snow-soil interface to volume scattering within the depth hoar layer.

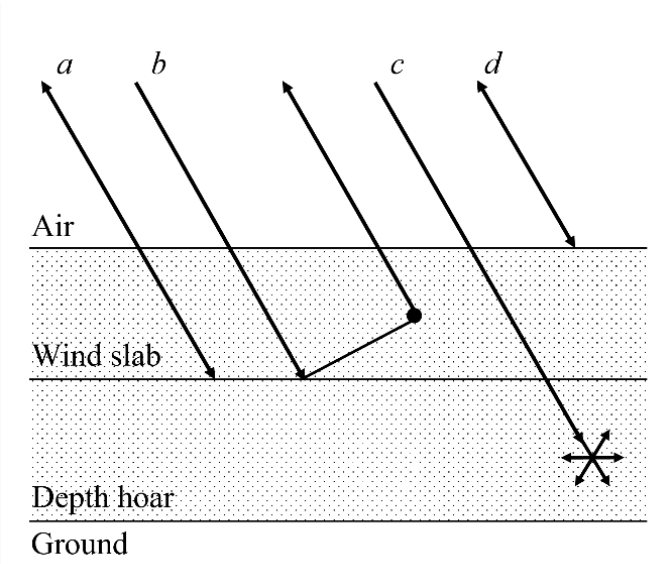

Figure 7-6. Schematic of scattering mechanisms. Surface scatter from wind slab-depth hoar interface (a), double-bounce from wind slab-depth hoar interface and wind slab (b), volume scatter from depth hoar (c), and surface scatter from air-snow interface (d).

The accuracy of the wind slab thickness estimates at 61° was encouraging. Although there is no established accuracy requirement for the estimation of snowpack layer thickness, the RMSE given in Figure 7.2 was comparable to the decimetre-scale accuracies of airborne LiDAR snow depth measurements (Deems et al., 2013) including those over Trail Valley Creek in 2013 (see King et al., 2018). To test applicability in a SWE retrieval context, SWE for each wind slab layer was calculated using *in situ* thickness and density measurements and compared to SWE calculated from

estimated wind slab thickness and mean *in situ* wind slab density, resulting in RMSE = 5.5 mm. This compared favourably with the common 30 mm SWE retrieval accuracy benchmarked in retrievals from entire snowpacks (ESA, 2012).

Double-bounce scattering was detected in snow-free measurements (refer to Figure 7.3) which could result in non-zero wind slab thickness estimates contributing to ϵ especially in shallow snowpack estimations. To mitigate uncertainty, this method is therefore recommended for use on snowpacks where depth hoar has developed since subnivean double-bounce responses will be masked by higher-order scattering as the microwaves transit depth hoar layers. Snowpack modelling could be used to identify the presence of depth hoar where *in situ* knowledge was unavailable, otherwise early-season observations should be avoided. Depth hoar chains, featuring dominant vertical orientation, may also contribute to ϵ due to violation of the random orientation assumption where present, however, snow grains demonstrate limited structural anisotropy and seldom reach extremes in orientation (Leinss et al., 2020). This uncertainty can be mitigated by using larger incidence angles (refer to Figure 7.4) to target wind slab layers whose grains characteristically demonstrate lower levels of structural anisotropy than depth hoar grains, in better accord with the random orientation assumption. Finally, regional calibration may be required for the relationship between wind slab thickness and p_{double} as variation in wind slab density and microstructure may contribute to estimation uncertainty.

Future work should aim to define the limits of this method. A maximum detectable wind slab thickness may exist, beyond which additional within-slab scattering events occur, converting double-bounce into higher-order scattering thus negating this method. Furthermore, additional measurements of wind slab ≥ 19 cm thick should be made in order to strengthen confidence in the relationship. Logistical constraints prevented the collection of more than five such data points during the observation period since the acquisition of snow-free measurements required up to two days for the complete excavation of snow at sites with the deepest snowpack. Further research should quantify the relationship between wind slab accumulation and its attenuating effects in a SWE retrieval context.

7.4 Conclusion

A positive linear relationship between wind slab thickness and double-bounce scattering was demonstrated using the Freeman-Durden polarimetric decomposition with 17.2 GHz UWScat measurements of a tundra snowpack near Trail Valley Creek, NT in 2017. This relationship was strongest at incidence angles ≥ 46° and wind slab with thickness ≥ 19 cm. Best results were acquired at a 61° incidence angle, where wind slab thickness estimation resulted in an RMSE of 6.0 cm while wind slab layer SWE estimation resulted in an RMSE of 5.5 mm in comparison with *in situ* measurements. Larger incidence angle and thicker wind slab resulted in a longer path length through

the wind slab layer while diminishing the effects of subordinate snow layers and underlying soil. Wind slab layers are characterized by small, wind-fractured snow grains and high, wind-driven density. This results in less scattering than in depth hoar, however, scattering still occurs, becoming more likely as path length through the wind slab layer increases; this was observed as an increase in double-bounce scattering associated with an increase in wind slab thickness and incidence angle. Furthermore, limitations in snowpack penetration were explored which provided further evidence that double-bounce scattering occurred near wind slab layers.

We have introduced a novel relationship that can be used to constrain wind slab thickness in radar-based SWE retrievals of tundra environments, especially for thicker snowpacks where the signal from subordinate layers may be decoupled from that of the slab. This is particularly important as wind slab has been shown to limit radar response to snow accumulation in a tundra environment where aeolian processes exert strong control on accumulation (King et al. 2018). This relationship is recommended for use in a tundra environment featuring depth hoar which masks double-bounce contribution from subnivean material, and which becomes especially important in a thinner snowpack, below the 19 cm snow depth threshold, where a response from subnivean material may be possible. To improve confidence in this relationship, its limits should be probed by testing on more sites where wind slab thickness ≥ 19 cm and by determining the maximum detectable wind slab thickness.

7.5 Acknowledgements

The authors wish to thank the Polar Continental Shelf Program for support in kind, and the Aurora Research Institute for logistical support. The authors also thank P. Marsh and B. Walker who facilitated the campaign in TVC. Special thanks are given to V. Vanthof for significant efforts in the field.

Chapter 8
Observations of coniferous forest at 9.6 and 17.2 GHz: Implications for SWE retrievals

8.1 Introduction

Snow is a critical component to the Earth's hydrologic cycle and energy balance as well as a source of fresh water for human consumption (Sturm et al., 2017). More than one-sixth of the global population depends on this water, but its availability is changing with changes to our climate (Barnett et al., 2005). Given the importance of snow and the predicted changes in its accumulation (Brown et al., 2017; Derksen and Brown, 2012; Derksen et al., 2012; Kunkel et al., 2016), it is important to monitor, yet understanding these changes is difficult due to inter-annual variability, inadequate remote sensing products, and poor snow records throughout most of the world (Sturm et al., 2017); the last two points are unequivocally linked.

Remote sensing approaches to estimate regional to global snow accumulation at a high level of accuracy are not available from satellites or from routine airborne observations. However, radar observations have the potential to provide snowpack information, especially snow water equivalent (SWE), globally and in a timely manner for effective water resource management, although this approach has yet to be proven. In situ and limited airborne Ku-band observations of snow have demonstrated sensitivity to SWE at the local scale with Ku-band backscatter sensitivity to SWE showing strong signature sensitivity in different environments with applicability for the modeling of radar response (Chang et al., 2014; King et al., 2013; King et al., 2015; Rott et al., 2010). Synthetic aperture radar (SAR) imaging can provide wintertime landscape observations at spatial resolutions <100 m which makes it an attractive proposition for snow mapping.

Current methods for estimating SWE at Ku- and X-band frequencies focus on moderate to shallow snow, and include those proposed by (Rott et al., 2010) for the CoReH20 mission and (Leinss et al., 2015) which uses an interferometric approach; other recent work has been done by (Cui et al., 2016; Xiong, et al., 2014; Zhu et al., 2018). However, these studies exclude forested regions and therefore neglect sub-canopy SWE. This is unsurprising since forested regions are among the most challenging environments for remote sensing of snow (Sturm et al., 2015). Of particular relevance in Canada, the boreal forest, dominated by coniferous species and situated in the circumpolar northern high latitudes, covers 270 million ha, or about 30% of the landscape (Brandt et al., 2013). Globally, boreal forest covers 1.1 billion ha and is the Earth's largest terrestrial ecosystem (Sturm et al., 2015). Given the northern locale and the intersection of the boreal zone with snow covered landscapes (Sturm et al., 1995) it is important that the estimation of SWE accounts for forest attenuation of the snow backscatter signal.

Recent studies on SWE retrieval from boreal environments typically rely on ancillary data, allometric relationships or forest modelling to delineate forested areas and provide the necessary parameters, such as forest cover fraction (*FF*) and transmissivity (Cohen et al., 2015; Macelloni et al. 2012; Macelloni et al., 2014; Montomoli et al., 2016; Montomoli et al., 2015). However ancillary data becomes quickly outdated, allometric relationships tend to be regionally specific, and forest models add complexity to SWE retrieval. Moreover, forestry applications of radar typically utilize C-, L- and P-band radar (eg. Dobson et al., 1992a; Le Toan et al., 1992; Ulaby et al., 1990) for their penetration capabilities with respect to biomass retrieval while there are limited forest studies focused on X-band and fewer focusing on Ku-band, so questions remain as to the influence of forest, particularly in the context of SWE retrieval. Therefore, in this study the Ku- and X-band radar signature from coniferous forest (herein referred to as forest) in a terrestrial snow accumulation environment was explored to quantify its effect on the radar response at Ku- and X-band frequencies. Three questions are addressed. First, what is the polarimetric radar response to forest vegetation in a snow accumulation environment, second, is there a distinctive Ku-band and X-band radar response that can distinguish a forested terrain, and third, how could these observations be applied to improve current SAR retrieval of SWE in a forested environment? In addressing these objectives, this study uses the Freeman-Durden three-component decomposition on scatterometer observations to interpret the Ku- (17.2 GHz) and X-band (9.6 GHz) radar response from a terrestrial snow accumulation environment.

8.2 Radar response to forest

The inhomogeneous, anisotropic nature of forest canopy adds complexity to the interpretation of microwave scattering which, as shown in Figure 8.1, consists of different mechanisms: 1) scattering direct from underlying ground, 2) specular scattering from ground-trunk interactions, 3) scattering from the canopy, and 4) ground-canopy interactions, where all terms may be attenuated from transmission through upper layers (Dobson et al., 1992b; Le Toan et al, 1992; Ulaby et al., 1990). Scattering of wavelengths at C-band or higher frequencies (X- or Ku-band) is dominated by the canopy and consists of scattering from canopy elements such as needles, twigs, and branches (Dobson et al., 1992a; Le Toan et al., 1992).

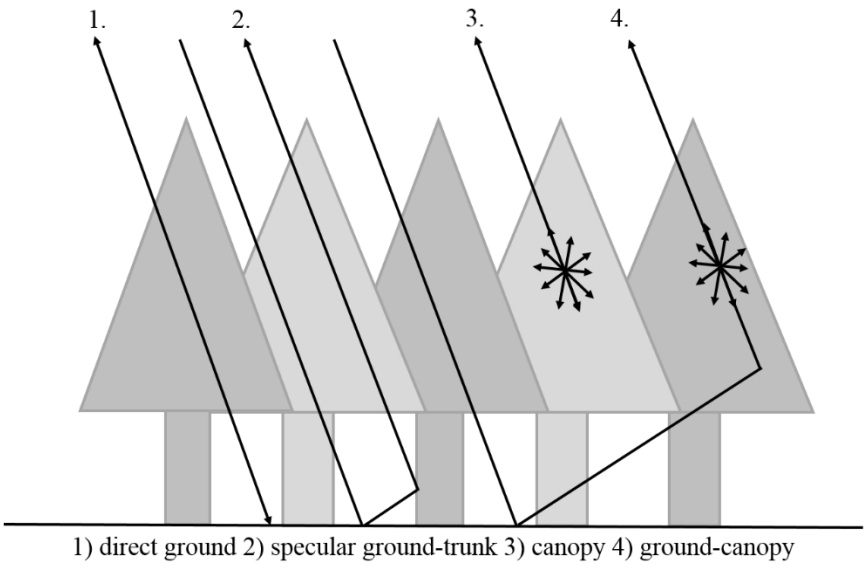

Figure 8-1. Scattering mechanisms of forests.

Radar backscatter is primarily controlled by structural attributes of the forest and tends to saturate at levels of biomass that scale with wavelength (Dobson et al., 1995). For this reason, longer wavelengths, such as L and P-band are preferred in biomass studies and have been used to successfully delineate forested landscapes (eg. Antropov et al., 2011; Arii et al., 2011; Dobson et al., 1992b; Durden et al., 1989). These frequencies also have sensitivity to biomass from the entire tree, and not just the canopy. However, they are not sensitive to terrestrial snow accumulation, unlike Ku- and X-band. Yet Ku- and X-band have weaker penetration capabilities in forested environments losing sensitivity at much lower levels of biomass with the response originating primarily from upper canopy elements; Montomoli et al. (2016) found that 83% and 39% of the Ku- and X-band response to a coniferous canopy originated from the needles. Despite the limited penetration capabilities of these frequencies, this study aims to demonstrate how Ku- and X- band radar scatterometer observations can be used to distinguish forested from non-forested landscapes and can provide biomass-related information for SWE retrievals.

8.3 SWE retrievals in forested landscapes

Recent radar-based SWE retrieval algorithms for use in forested regions have been developed through the CoReH20 framework of Rott et al. (2010) (eg. Cohen et al., 2015; Macelloni et al., 2012; Magagi et al., 2002; Montomoli et al., 2016). These models rely on parameters linked to biomass such as *FF* and two-way transmissivity to scale backscatter from the sub-canopy environment. Such parameters are sourced from a priori ancillary information (e.g., traditional forest inventories, active and passive optical datasets), modelled estimates, and allometric relationships, but there are considerable limitations associated with these approaches. A priori information, such as forest inventories, can quickly become outdated due to growth and abrupt

landscape change, or be unavailable as Le Toan et al. (1992) found. Allometry is regional in nature necessitating local relationships (Dobson et al., 1995) which may be unavailable, especially in remote regions. Modelled estimates can be prohibitive due to their complexity, the number of inputs required (eg. geometrical description of leaves, branches, trunks, density, and *FF*) and the mismatch of required inputs and available data (Montomoli, 2016). The inversion of such models is often impossible given the large number of inputs required, and the limited outputs in the forward model (Freeman and Durden, 1998). Furthermore, estimates of *FF* and transmissivity are sensitive to incidence angle and forest architecture which necessitate a detailed geometrical description of the canopy. This is challenging on a local scale, and impractical on a global one. A final drawback of using *FF* in this application is that it is based on optical scattering yet is intended for use in a microwave scattering model and so it provides a less appropriate description of the forest canopy. A simpler method is proposed that uses the volume scattering proportion (V_{FD}) from the Freeman-Durden three-component decomposition and does not require ancillary data, forest models, or allometric relationships, yet is sensitive to the influence of incidence angle and forest architecture. A number of studies have employed model-based polarimetric decompositions, such as the Freeman Durden three-component decomposition to identify the dominant scattering mechanisms of complex natural and artificial targets. Such studies have often aimed to distinguish land cover types and have demonstrated sensitivity to forested landscapes (An et al., 2010; Antropov et al., 2011; Freeman, 2007; Freeman and Durden, 1998; Hajnsek et al., 2009; van Zyl et al., 2011; Yamaguchi et al., 2005), however these studies employed C-, L- and P-band data.

8.4 Study location and site description

The observations in this study were collected from 22 sites, spanning four field campaigns and seven years. Forested and non-forested sites were observed on Grand Mesa, CO in February 2017, as part of the NASA SnowEx 2017 field campaign (Kelly and Thompson, 2018), and from Trail Valley Creek (TVC), NT in April 2017. Forested sites were observed in Churchill, MB during the winter of 2010/2011, as part of the Canadian Snow and Ice Experiment (CASIX), and in Tobermory, ON during the winter of 2013/2014. See Figure 8.2 for site locations and Figure 8.3 for photographs of each forested site.

Grand Mesa is a large flat-topped mountain located in western Colorado with a yearly average maximum air temperature of 7.8 °C and an annual snowfall of over 9 m (Western Regional Climate Center, 2018). The study sites were situated at about 39.0395°N, 107.9417°W with an elevation of 3176 m above sea level (a.s.l.). The non-forested sites were primarily flat, grassy meadowland while the forested site was comprised of Englemann spruce ranging in height from 1 m to 9 m. Soils consisted of gravelly loam over bedrock (United States Department of Agriculture, 2018). Forested observations were made from an elevated platform.

TVC is located 50 km north of Inuvik, NT at 68.7462°N, 133.5022°W and 50-180 m a.s.l.. The annual average air temperature is -8.2 °C, and it receives about 159 cm of snowfall annually (Environment and Climate Change Canada, 2018a). Vegetation is primarily grass, lichens and mosses with alder, birch, willow, and black spruce found on hillslopes and in valley bottoms (Marsh et al., 1996). The terrain is hummocky, and soils consist of peat, and silty clay soil over permafrost (Pohl et al., 2005). Non-forested sites consisted of open tundra, while the forested site consisted of black spruce ranging from 0.6 to 3m in height. All observations were ground-based.

Churchill is situated on the western shore of Hudson Bay near the Churchill River. The yearly average air temperature is -6.5 °C and it receives about 201 cm of snowfall annually (Environment and Climate Change Canada, 2018b). The study site is located at approximately 58.7299°N, 93.8203°W and 29 m a.s.l. near the tree line on organic soils over permafrost (Kershaw et al., 2007; King et al., 2015). The radar observations were made, from an elevated platform, of a black spruce forest and taiga snow environment; trees ranged in height to a maximum of about 15 m.

Tobermory is situated on the Niagara Escarpment, at the northern edge of the Bruce Peninsula, at about 45.2573°N, 81.6561°W and 213.4 m a.s.l.. The region has a yearly average air temperature of 6.6 °C and receives about 405 cm of snowfall annually (Environment and Climate Change Canada, 2018c). Radar observations were made from an observation tower over a mature mixed species forest which included eastern white cedar, white spruce, and white birch. Tree height was approximately 15 m. Soils consist of sandy loam over exposed bedrock (Canadian Soil Information Service, 2018).

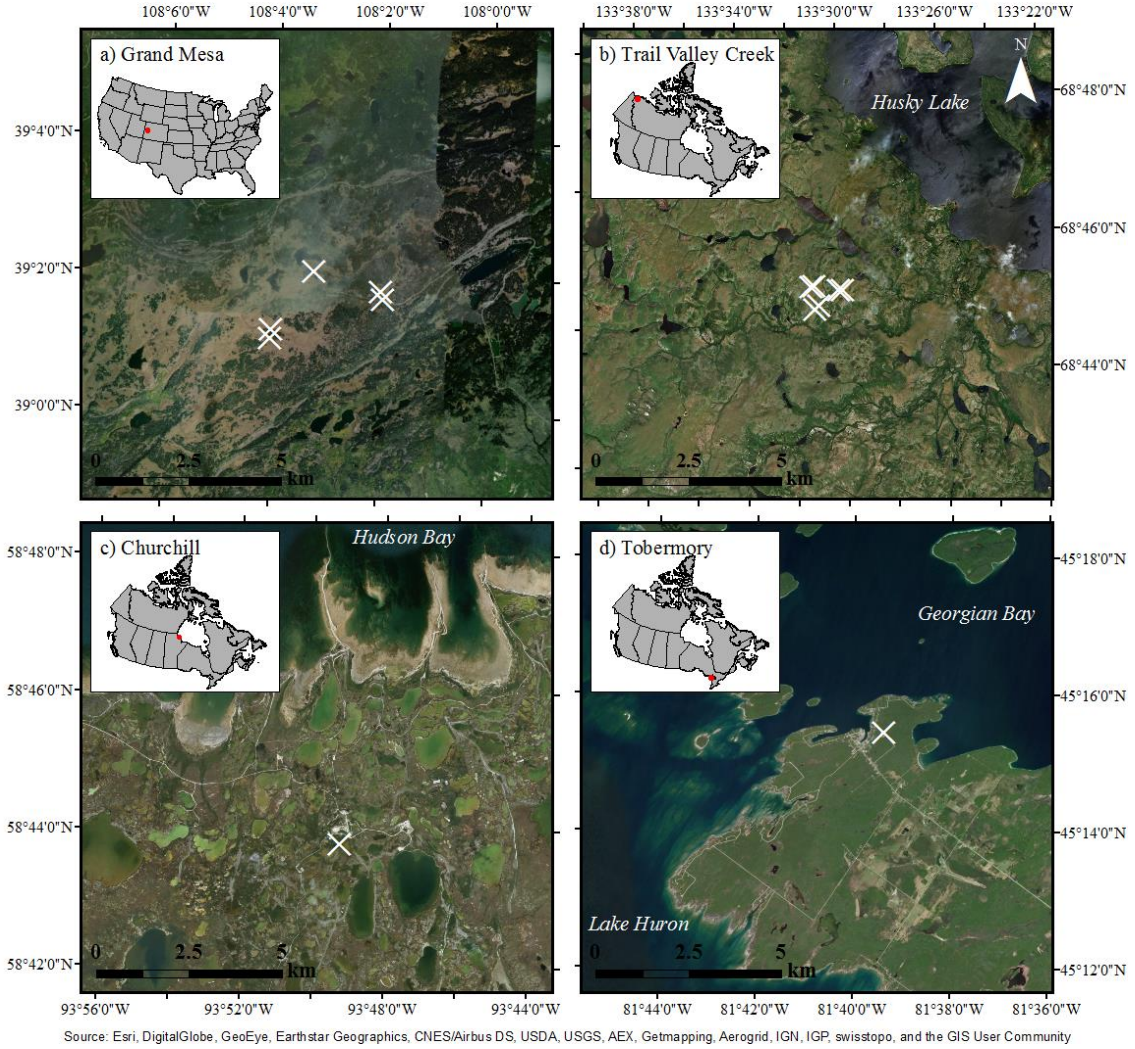

Figure 8-2. Site locations at (a) Grand Mesa, Colorado, (b) Trail Valley Creek, Northwest Territories (c) Churchill, Manitoba and (d) Tobermory, Ontario.

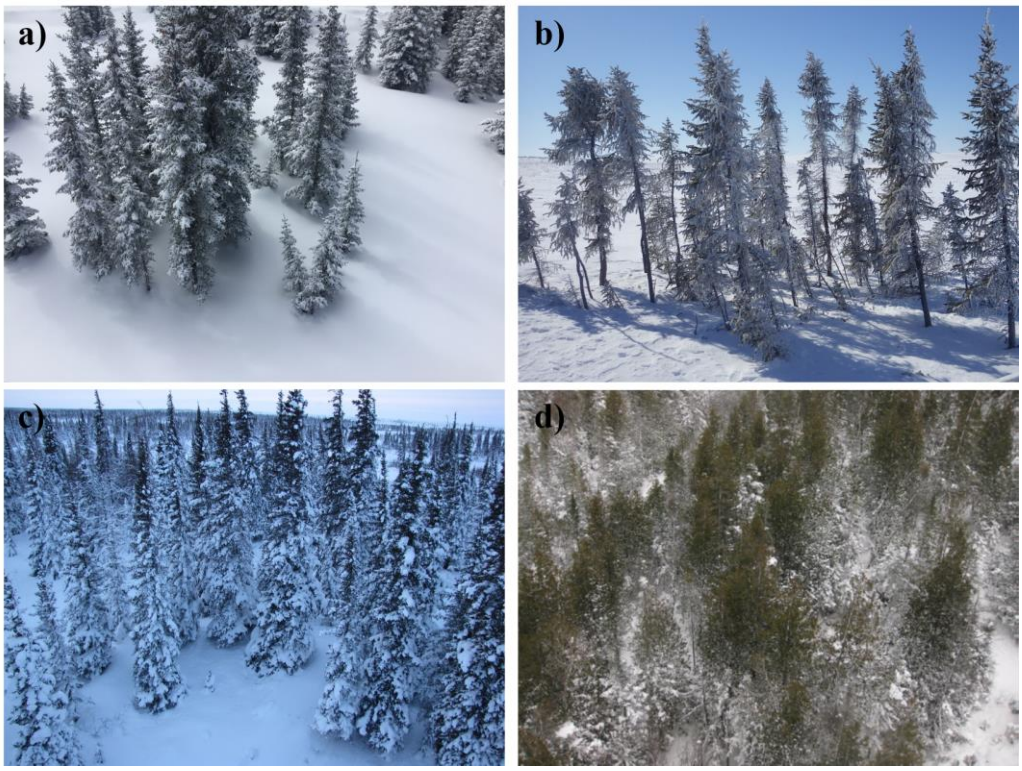

Figure 8-3. Forested sites at (a) Grand Mesa, (b) Trail Valley Creek, (c) Churchill and (d) Tobermory.

Air temperatures during acquisition periods at each site are provided in Figure 8.4. Observations were generally made during periods of cold, dry weather with the exception of those made in Tobermory on March 31, May 7, and May 22 (sites 18, 19 and 22) during which time air temperatures were above 0 °C.

A summary description of each observation site is provided in Table 8.1 and includes bulk snowpack properties. Snow depth in non-forested sites ranged from 33 cm to 205 cm corresponding to SWE values of 121 mm to 675 mm. Snow depth in forested sites ranged from 21 cm to 83 cm corresponding to SWE values of 38 mm to 202 mm although *in situ* measurements of snow were not made within forested sites on Grand Mesa where the deepest non-forested snow was found; it is expected the forested sites on Grand Mesa (sites 14 & 15) had depths at least as great as the adjacent non-forested site (site 5). Snow density ranged from 159 kg/m3 in the taiga forests of Churchill to 416 kg/m3 in the wind slab dominated tundra drifts of TVC.

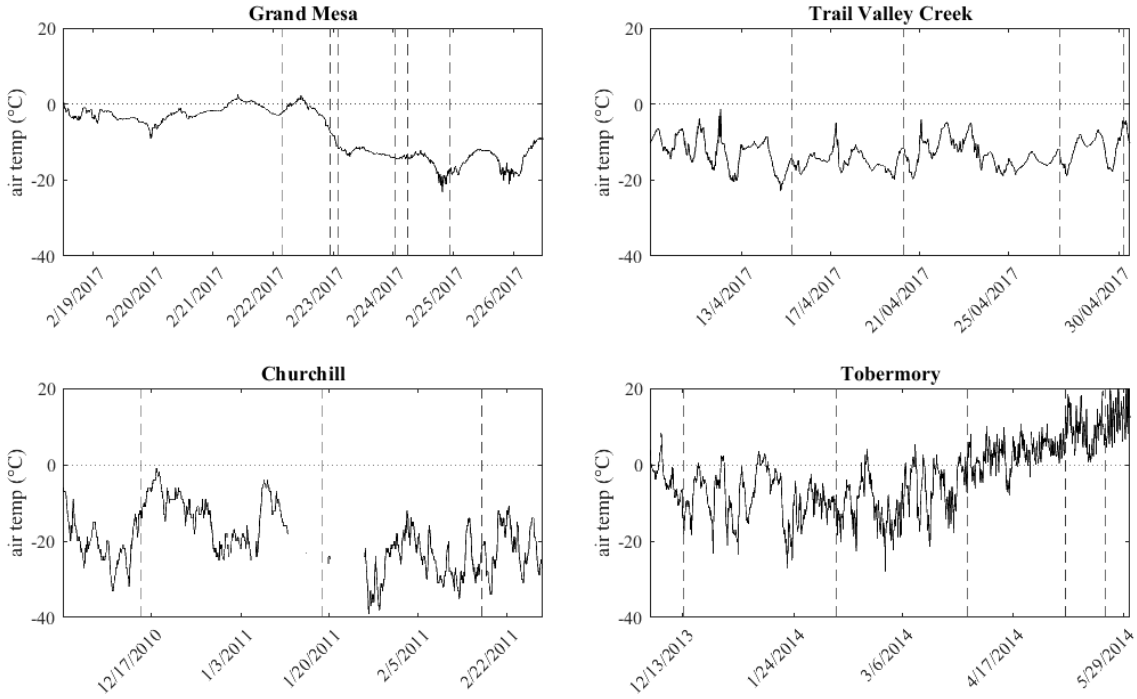

Figure 8-4. Air temperatures during observation periods. Vertical lines denote observations.

Table 8-1. Summary of UWScat observation parameters and bulk snowpack properties.

Site Description				UWScat Observation Parameters				Bulk Snowpack Properties					
Site no.	Class	Site	Date	Azimuth sweep	Incidence angle range	Incidence angle step	Antenna height[a] (m)	Depth (cm)	Density (kg/m^3)	SWE (mm)	Depth hoar (%)	Wind slab (%)	Notes
1	non-forest	Grand Mesa	22/02/17	30°, −30°	25°, 62°	3°	2.1	178	319	568	na	na	
2	non-forest	Grand Mesa	23/02/17	30°, −30°	25°, 62°	3°	2.1	162	331	536	0	0	high wind
3	non-forest	Grand Mesa	23/02/17	30°, −30°	25°, 62°	3°	2.1	na	na	na	na	na	
4	non-forest	Grand Mesa	24/02/17	30°, −30°	25°, 62°	3°	2.0	180	300	540	0	0	
5	non-forest	Grand Mesa	25/02/17	−10°, −40°	25°, 65°	3°	9.5	205	329	675	3	0	Skyjack, trees within FOV
6[d]	non-forest	Trail Valley	15/04/17	20°, 80°	25°, 62°	3°	2.1	62	308	110	35	37	gap in snowpack below 17 cm
7	non-forest	Trail Valley	20/04/17	30°, 90°	25°, 62°	3°	2.1	92	416	137	27	53	drift, large alder shrub buried in FOV
8	non-forest	Trail Valley	20/04/17	30°, −30°	25°, 62°	3°	2.1	90	356	192	18	54	drift, adjacent to 7
9	non-forest	Trail Valley	27/04/17	20°, 80°	25°, 62°	3°	2.1	0	0	0	0	0	same as 6, all snow removed from FOV
10	non-forest	Trail Valley	30/04/17	30°, −30°	25°, 62°	3°	2.0	33	368	55	42	24	
11	forested	Churchill	15/12/10	30°, −30°	21°, 81°	3°	10.2	21	183	28	58	0	Skyjack
12	forested	Churchill	18/01/11	30°, −30°	21°, 81°	3°	10.2	28	159	33	38	0	Skyjack
13	forested	Churchill	17/02/11	30°, −30°	21°, 81°	3°	10.2	39	174	67	45	0	Skyjack
14	forested	Grand Mesa	24/02/17	30°, −30°	25°, 65°	3°	9.9	na	na	na	na	na	Skyjack
15	forested	Grand Mesa	25/02/17	20°, −10°	25°, 65°	3°	9.5	na	na	na	na	na	Skyjack
16	forested	Tobermory	13/12/13	30°, −30°	35°, 70°	5°	22.2	21	na	66	na	na	observation platform
17[e]	forested	Tobermory	09/02/14	30°, −30°	35°, 70°	5°	22.2	50	246	118	0	0	observation platform
18	forested	Tobermory	31/03/14	30°, −30°	35°, 70°	5°	22.2	46	na	115	na	na	observation platform
19	forested	Tobermory	22/05/14	30°, −30°	35°, 60°	5°	22.2	0	0	0	0	0	observation platform
20[d]	forested	Trail Valley	15/04/17	20°, −40°	25°, 62°	3°	2.1	83	284	145	36	10	adjacent to 6, branch gaps in snowpack
21[b]	forested	Trail Valley	27/04/17	20°, −40°	25°, 62°	3°	3.0	0	0	0	0	0	same as 20, snow removed from FOV
22[c]	forested	Tobermory	07/05/14	30°, −30°	35°, 60°	5°	22.2	0	0	0	0	0	observation platform

[a]antenna height at full vertical extension equivalent to a 90° incidence angle; [b]instrument mounted on top of a 0.9-m snowpack observing a snow-excavated field of view (FOV) giving an antenna height of 3.0 m; [c]X-band only; [d]snowpit completed on 25/04/17; [e]snowpit completed on 27/01/14. SWE: snow water equivalent.

8.5 Field observations & methods

UWScat is a dual frequency Ku- and X- band scatterometer system operating at center frequencies of 17.2 GHz and 9.6 GHz, respectively. King et al. (2013) provides a full description of the system and Table 8.2 shows the principal system parameters. Scatterometer calibration was achieved with an internal procedure which uses a delay line calibration loop to account for gain variations due to temperature fluctuation, and an external procedure using an in-scene trihedral calibration target to generate the transmitter distortion matrix. An unobstructed sky observation was employed to characterize transmitter leakage and a near-field gain correction described by (Sekelsky et al., 2002) was applied when the target was within the antenna's far-field distance (< 5.4 m at 17.2 GHz, and < 17.1 m at 9.6 GHz). The instrument is tripod-mounted with the antenna positioned ~2 m above the snow surface for near-ground deployments, at ~ 10 m above ground on a Skyjack platform, and ~22 m above ground on an observation tower. Radar observations in Churchill and Tobermory were taken from the same position over different dates. Efforts were made to ensure the positional accuracy was maintained on each deployment. This revisit scheme was necessitated by logistical constraints which limited the opportunities to deploy UWScat at elevations above the forest canopy in these particular environments. Similarly, forested sites on Grand Mesa were also revisited (see sites 14 and 15 in Table 8.1) although these observations were azimuthally offset by 10° and therefore capture a different perspective of the same forest. At TVC, only sites 6 and 9 were revisited (see sites 20 and 21 in Table 8.1), but the snow was removed before the second set of radar observations. The observation parameters employed in this study were variable and are summarized in Table 8.1 along with bulk snowpack properties for all observations. In all cases, except sites 9, 19, 21, and 22, there was snow accumulation present. Sites 19 and 22 were observed in May so no snow was present and air temperatures were warm. In each case, the normalized radar cross section (σ°) and polarimetric parameters were derived by averaging the independent samples within each azimuth sweep over a homogeneous target. This procedure improves measurement precision and minimizes the effects of radar fade.

Table 8-2. UWScat system parameters.

Parameter	Ku	X
Output frequency (GHz)	16.95–17.45	9.35–9.85
Center frequency (GHz)	17.2	9.6
Transmit power, narrow beam (dBm)	−8	−11.8
Transmit bandwidth (MHz)	500	500
Range Resolution (m)	0.3	0.3
Antenna beam width, narrow/flood (°)	5.6/7.5	4.3/5.8
Cross-polarization isolation (dB)	>30	>30
Transmit/receive polarizations (linear)	VV, HH, VH, HV	VV, HH, VH, HV
Sensitivity (dB m^2m^{-2})	−50	−50

The power response of the forested and non-forested classes was compared across all elevation angles for sites 6 and 20, and 9 and 21. These particular pairings were chosen because they allowed us to observe a forested site immediately adjacent to a non-forested site from one location, under similar conditions. Sites 9 and 21 are the same as sites 6 and 20 however the snow had been carefully removed from the FOV allowing a comparison of both sites with and without snow.

In order to distinguish between the forested and non-forested class within the FOV, a comparison was made of range profiles across a subset of incidence angles (34°, 40°, 46°, 49°, 55°, and 61°). Due to differing observation parameters, incidence angles of Churchill observations were offset by -1° from those of Grand Mesa and TVC. Similarly, incidence angles of Tobermory observations included 34°, 40°, 45°, 49°, 55° and 60°. These angles were chosen because they were common among all forested observations. Range profiles, which describe the power response as a function of range from the antenna were used to distinguish the forested from non-forested class by comparing the number of inflection points in each profile. The target profile was manually identified for each elevation angle in order to exclude system leakage which occurs at near range, and random noise which follows the target signal with power levels at or below -50 dB. An algorithm comparing the slope of the line between each successive pairs of points was then used to identify inflection points along the target profile. The initial and final inflection points, as the range profile transitioned from system leakage to target signal, and from target signal back to noise, were excluded from the tally therefore the minimum possible number of inflection points was 1. Figure 8.5 provides an example of range profiles for the forested and non-forested classes to illustrate this method.

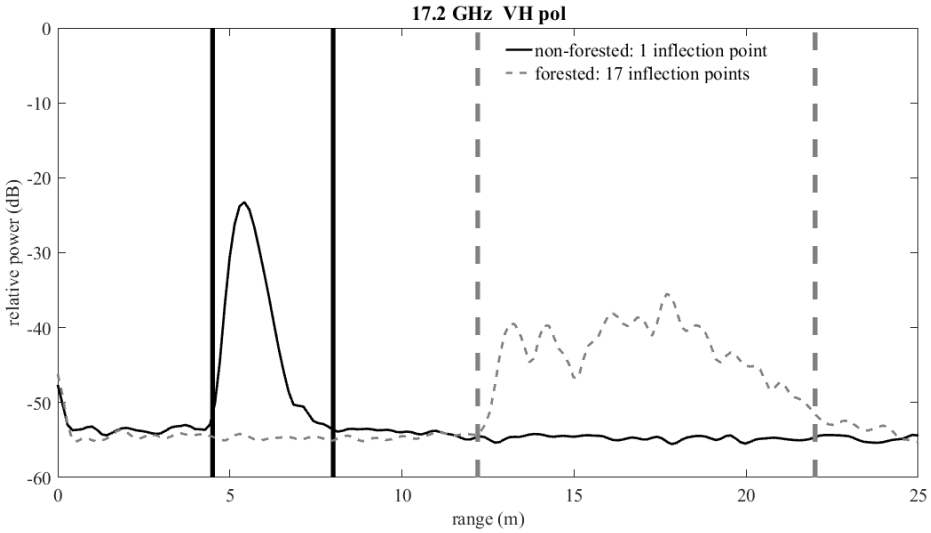

Figure 8-5. Typical range profiles of non-forested (left) and forested sites (right). Vertical bars bound target profiles, between which inflection points were tallied.

In order to analyze the results of the power response, the Freeman-Durden three-component decomposition (Freeman and Durden, 1998) was performed on each incidence angle of each scan. The Freeman-Durden three-component decomposition was one of the first model-based decompositions and remains among the simplest therefore it was chosen for this study. The model incorporates the measured covariance matrix as a linear combination of three scattering mechanisms: volume scatter from a cloud of randomly oriented dipoles, double-bounce scatter from two orthogonal surfaces, and Bragg scatter from a moderately rough surface (Arii et al., 2011; Freeman and Durden, 1998; Freeman and Durden, 1993). Assumptions of the model include reciprocity, reflection symmetry, and the representation of volume scatterers as a cloud of randomly oriented dipoles (Antropov et al., 2011; Freeman and Durden 1998; Yamaguchi et al., 2005). These assumptions are of greater significance at longer wavelengths such as C-, L-, and P-band since these will interact with the larger structural components of the forest, such as trunks and large branches, which are neither randomly oriented nor truly symmetrical (Arii et al., 2011). At 17.2 GHz and 9.6 GHz, since scattering originates almost entirely from the smaller canopy elements, these assumptions are acceptable. The results of the decomposition were normalized by total power therefore each scattering mechanism was described as a proportion of the total power for each elevation angle. This provided greater separation between scattering mechanisms and negated the effects of the decrease in backscattered power with increasing elevation angles typically observed as compared to the standard Freeman-Durden output, which provides a measure of power for each

scattering mechanism. For each site, V was aggregated into forested and non-forested classes for comparison.

For each of the forested sites, *FF* was compared with V_{FD}. *FF* was derived from pixel counts of air photos or satellite imagery of forested and non-forested regions within the scatterometer FOV resulting from image classification. Estimates were calculated for a rectangular area in the FOV of approximately similar size to that scanned with the scatterometer. While images were not coincident with radar observations, efforts were made to acquire suitable images as close to the radar observation dates as possible. Images for Churchill and Grand Mesa were acquired from Google Earth and dated July 2014 and June 2016, respectively. An aerial photograph of Tobermory was sourced from the Southwestern Ontario Orthophotography Project (SWOOP) dated April/May 2010. The TVC image was sourced from drone photography in April 2018.

The *in situ* field measurements included standard snow pit observations such as snow depth, density, stratigraphy, and temperature profiles (Elder et al., 2018), and microstructural observations including specific surface area (Rutter et al., 2018) and penetration force (Derksen et al., 2017). Such measurements were necessary in order to understand the microwave response in terms of the physical properties of the target on the ground. Whenever possible, snow pits were located adjacent to the radar FOV. Nearby weather stations monitored local weather conditions including air temperature as shown in Figure 8.4 (Environment and Climate Change Canada, 2018d; NASA, 2017).

8.6 Results and analysis

8.6.1 Angular backscatter response from forested and non-forested sites

Minimal difference in backscatter was observed between forested (S20) and non-forested (S6) sites with snow in Figure 8.6a, while a greater difference, up to 4.5 dB and 6 dB for co- and cross-polarized backscatter, was observed between forested (S21) and non-forested (S9) sites without snow in Figure 8.6b; the larger cross-polarized difference was a result of enhanced volume scattering in the forest canopy. Since the SWE at S20 was 48 mm greater than at S6, greater backscatter would be expected at the forested site, especially given the larger proportion of wind slab present in the non-forested site which would have reduced sensitivity to SWE (King et al., 2018), but this wasn't the case. This indicated that the forest canopy partially attenuated the signal from the snow beneath. A greater difference in backscatter between snow-on and snow-off conditions was observed at the non-forested site, in Figure 8.6d, than at the forested site, in Figure 8.6c, once again demonstrating attenuation of the

snow signal by the forest canopy. Montomoli et al. (2016) also found forests to diminish the sensitivity to SWE. A stronger backscatter response would therefore be expected from the 202 mm of SWE at the forested site (site 20) if the trees were not present, thus leading to a potential underestimation of SWE which supports the need for a SWE scaling factor in retrievals over forested landscapes.

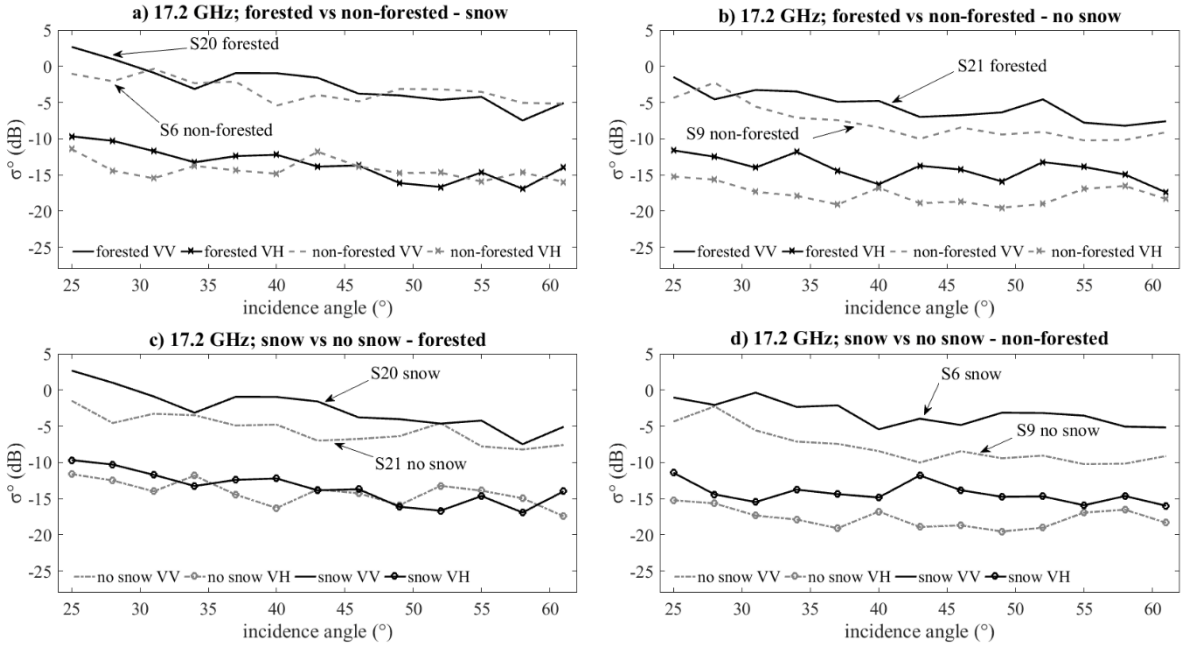

Figure 8-6. Comparison of 17.2 GHz backscatter response (VV and VH) as a function of incidence angle at TVC and Grand Mesa sites. TVC sites 6 (non-forested [S6]) and 20 (forested [S20]), and sites 9 (non-forested [S9]) and 21 (forested [S21]). The figures compare the 17.2 GHz responses between forested and non-forested sites for snow (a) and no snow (b) cases. Also shown are the 17.2 GHz responses between snow and no snow sites for forested (c) and non-forested (d) cases at TVC.

A comparison of the angular response of forested and non-forested sites at 9.6 GHz is shown, with snow, in Figure 8.7a and without snow, in Figure 8.7b. Across all elevation angles and polarizations, the 9.6 GHz backscatter of the forested site was consistently greater than that of the non-forested site both with and without snow. The greater difference observed in the cross-polarized response once again suggested a volume response from the canopy. Figures 8.7c and 8.7d show the response at 9.6 GHz to the removal of snow in forested and non-forested sites. Minimal sensitivity to the presence of snow accumulation was observed at both sites. Overall, the observations in Figure 8.7 show little sensitivity to sub-canopy snow accumulation for this particular forest at 9.6 GHz.

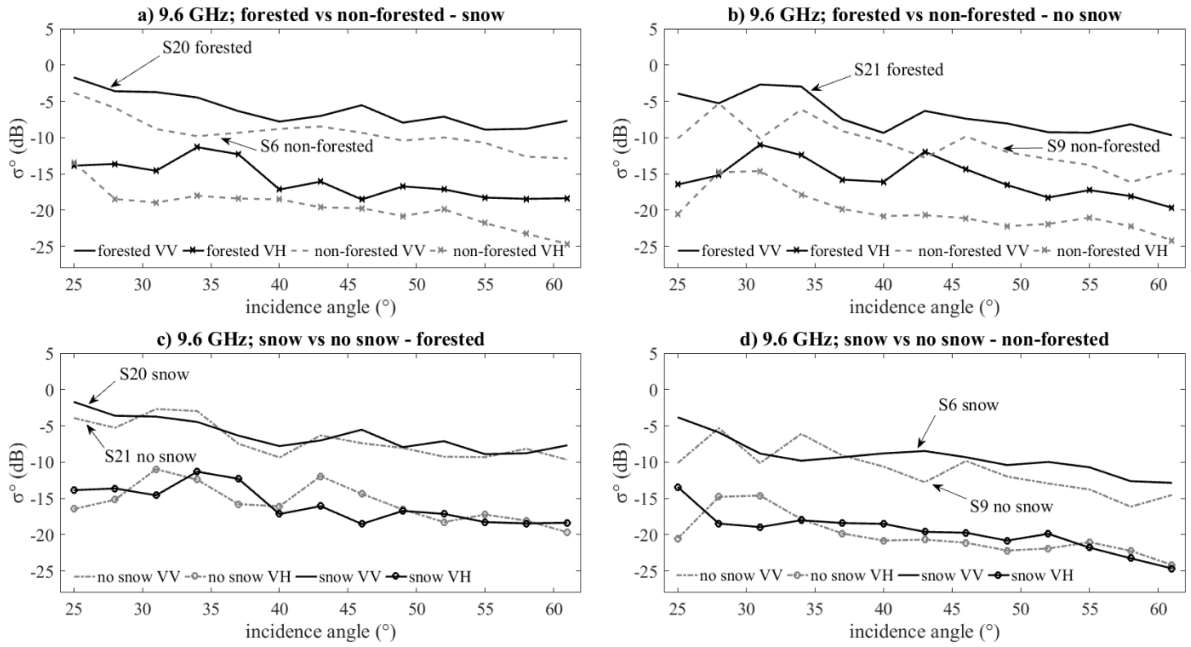

Figure 8-7. Comparison of 9.6 GHz backscatter response (VV and VH) as a function of incidence angle at TVC and Grand Mesa sites. TVC sites 6 (non-forested [S6]) and 20 (forested [S20]), and sites 9 (non-forested [S9]) and 21 (forested [S21]). The figures compare the 9.6 GHz responses between forested and non-forested sites for snow (a) and no snow (b) cases. Also shown are the 9.6 GHz responses between snow and no snow sites for forested (c) and non-forested (d) cases at TVC.

These results are important because they illustrate the non-trivial influence of forest on SWE estimates particularly at 17.2 GHz and highlight the importance of identifying forested areas and accounting for them in SWE retrievals. As such, the presence of even sparse forest could contribute error to SWE estimates if left unaccounted.

8.6.2 Range profile analysis

The mean number of inflection points and the standard deviations are provided for range profiles of all sites and elevation angles in Table 8.3. The mean number of inflection points was significantly greater in the forested than in the non-forested class, for every combination of frequency, polarization, and elevation angle (significance level = 0.05); across all observations, the range profiles of the forested class had a mean of 18 inflection points, while that of the non-forested class had a mean of 4 inflection points. The large number of inflection points observed in the forested class indicates higher-order

scattering associated with the canopy response at both 17.2 GHz and 9.6 GHz. The forested class also had a larger standard deviation in most cases which was attributed to variation in tree size and canopy density. These results have two important implications: 1) this information could be used to distinguish forested from non-forested environments, and 2) it suggests a useful link between canopy volume and microwave scattering. Site 6, a non-forested site, was excluded from this analysis due to the inclusion of forest near the edge of the FOV, particularly evident at high incidence angles.

Table 8-3. Mean number of inflection points from range profiles. All sites included in calculations. Standard deviation given in brackets.

	Incidence Angle	17.2 GHz			9.6 GHz		
		VV	HH	VH	VV	HH	VH
Forested	34°	17.2 (12.1)	14.7 (8.7)	16.8 (12.1)	18.4 (12.3)	18.5 (13.3)	18.4 (12.5)
	40°	16.4 (12.5)	16.9 (11.1)	15.8 (11.3)	20.3 (13.3)	21.3 (14.1)	20.7 (13.6)
	46°	15.0 (9.1)	16.5 (9.7)	15.5 (12.1)	19.3 (13.6)	19.4 (14.6)	18.3 (13.6)
	49°	14.2 (6.9)	15.0 (8.6)	14.5 (7.7)	18.0 (11.4)	19.5 (10.7)	18.1 (12.5)
	55°	17.3 (7.5)	17.5 (7.8)	18.3 (8.3)	20.7 (8.1)	19.3 (8.3)	19.6 (9.1)
	61°	16.5 (6.6)	16.6 (6.2)	17.8 (6.8)	21.0 (7.5)	19.6 (7.3)	21.3 (8.8)
Non-forested	34°	4.9 (2.3)	5.6 (1.3)	4.3 (2.3)	4.2 (2.0)	4.8 (2.2)	3.4 (1.7)
	40°	4.7 (1.0)	5.3 (1.0)	3.4 (2.4)	4.4 (1.9)	4.6 (2.9)	2.8 (1.6)
	46°	4.1 (1.5)	4.0 (1.8)	3.3 (1.7)	3.4 (1.8)	4.0 (1.7)	3.2 (1.9)
	49°	4.1 (2.4)	4.0 (1.5)	3.3 (1.4)	3.8 (2.2)	3.6 (2.1)	3.1 (2.2)
	55°	3.6 (2.1)	4.8 (1.9)	3.3 (2.6)	3.8 (2.7)	3.8 (2.2)	2.6 (1.9)
	61°	3.8 (2.4)	3.5 (2.8)	3.4 (2.2)	3.3 (2.4)	3.5 (2.5)	2.9 (2.5)

8.6.3 Freeman-Durden three-component decomposition

Figure 8.8 shows a comparison of the volume scattering proportion of the decomposition aggregated into forested and non-forested classes. Volume scattering dominated the forest response, and the difference was found to be significant at both frequencies and all elevation angles (significance level = 0.05). This is in agreement with the range profile observations which suggested elevated levels of volume scattering by way of a significantly greater number of inflection points for the forested class. The forested class showed a larger spread in V_{FD} which reflects the variety of forest observed, ranging from a sparse plot of 3 m black spruce to a dense plot of 15 m white spruce and white cedar. Site 6 was once again excluded from this analysis due to the inclusion of forest within the FOV.

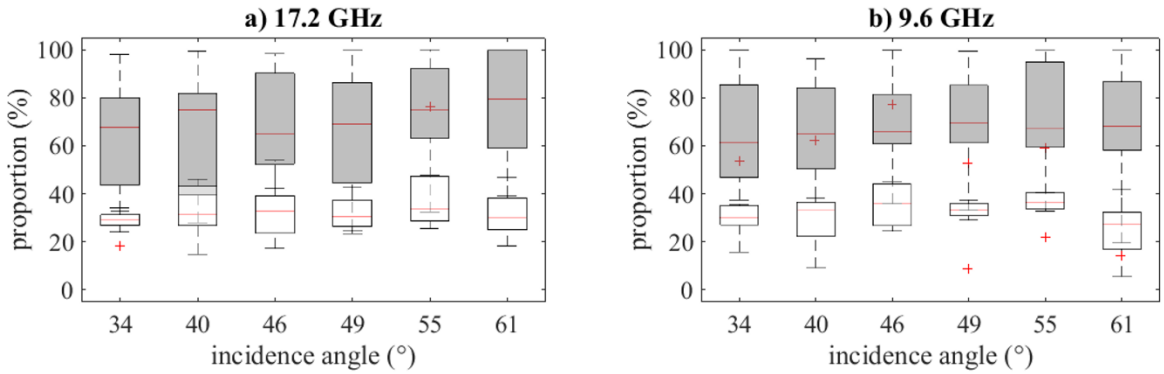

Figure 8-8. Comparison of volume scattering proportion for forested (shaded) and non-forested (white) sites at (a) 17.2 GHz, and (b) 9.6 GHz.

8.6.4 Correlation between forest fraction and volume scattering

The results of the *FF* calculation for each forested site are presented in Table 8.4. The Tobermory scene had the highest *FF* at 84%, followed by Churchill, Grand Mesa, and TVC with *FF* of 48%, 39%, and 16%. All of the optical images used in calculating *FF* except for the TVC image were acquired in snow-free periods. Area sampled was a function of radar antenna height in Tobermory and Churchill where the forested extent was much larger than the radar FOV, and of forest stand dimensions in Grand Mesa and TVC, where the radar FOV was matched to the forested extent.

Figures 8.9 and 8.10 show the comparison between *FF* and V_{FD} of forested sites at 17.2 GHz and 9.6 GHz, respectively. There was strong correlation between *FF* and V_{FD} particularly at higher elevation angles where R = 0.93 at 17.2 GHz (61°) and R = 0.88 at 9.6 GHz (55°). All correlations were significant at the 0.05 level. The strength of correlation increased with incidence angle because at low angles, the radar footprint encountered a treeless gap between the scatterometer and the forest edge at all sites except Tobermory and so regardless of *FF*, the microwaves encountered only a small portion of canopy vegetation. As the incidence angle increased, the microwaves interacted more fully with the canopy. Variation in volume scattering at each site was due to changes in tree geometry brought about by wind, snow loading and other factors that occurred between acquisition dates. Although there was a strong correlation between *FF* and volume scattering at these frequencies, it is important to remember that *FF* is a generalized bulk forest property based on the surface scattering of optical radiation and is not directly linked to the volume of biomass but rather to the surfaces exposed to the sensor. However, V_{FD} is a direct result of microwave interaction with the three-dimensional forest canopy elements, not just its surface. Therefore, V_{FD} provides a more robust representation of the scattering elements than

FF in a microwave application. This explains why there was greater variation in V_{FD} than in *FF*. In this way, V_{FD} accounts for incidence angle and tree geometry and does not require ancillary information or canopy modelling.

Table 8-4. Results of the forest cover fraction (*FF*) calculation.

Site	Photo Date	Area Sampled (m^2)	# of Forest Pixels	# of Non-Forest Pixels	*FF* (%)
Tobermory	May 2010	918	19720	3739	84
Churchill	July 2014	450	4338	4638	48
Grand Mesa	June 2016	252	21424	33153	39
TVC	April 2018	25	4123	22185	16

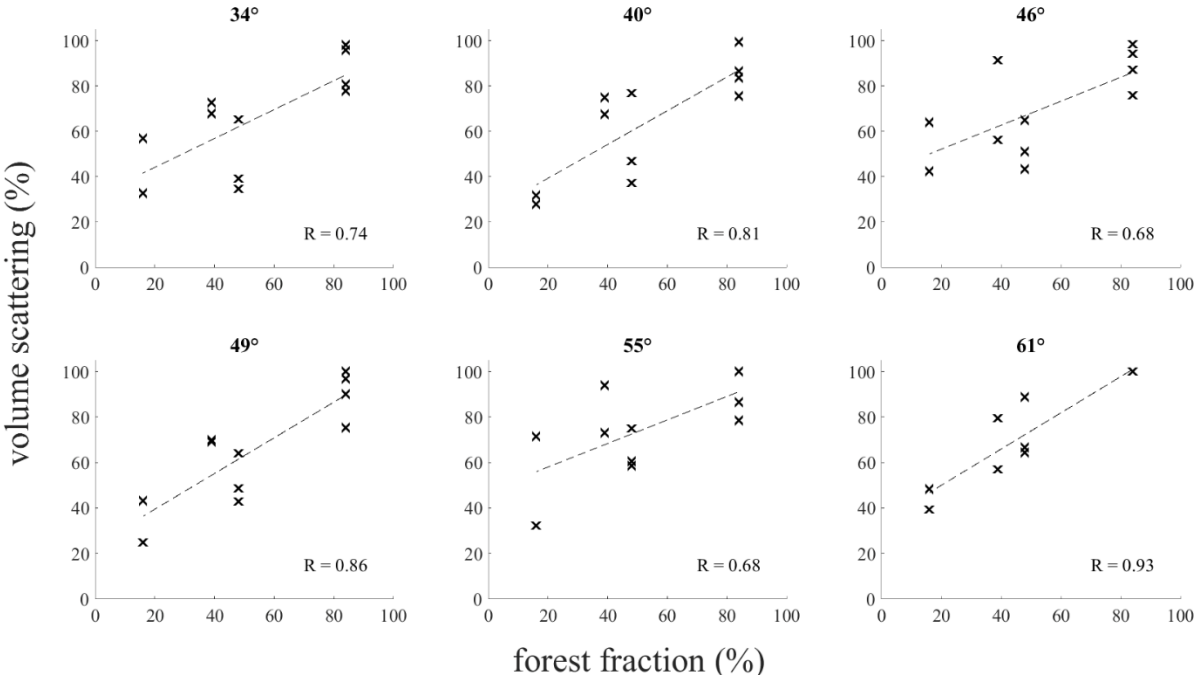

Figure 8-9. Volume scattering at 17.2 GHz vs *FF* for forested sites at each incidence angle. Line of best fit is for illustrative purposes only.

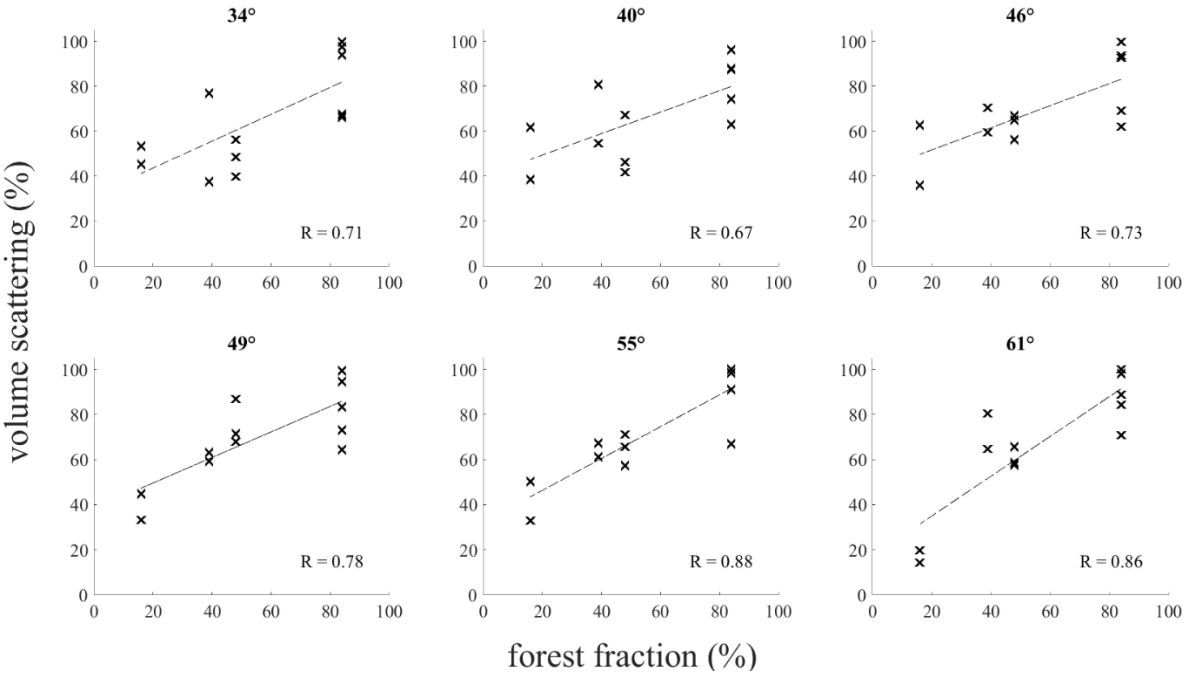

Figure 8-10. Volume scattering at 9.6 GHz vs *FF* for forested sites at each incidence angle. Line of best fit is for illustrative purposes only.

8.7 Implications for SAR-based SWE retrievals in forest-covered landscapes

The scatterometer observations in Sections 4.2 and 4.3 demonstrate the ability to distinguish forested from non-forested landscapes and either the range profiles or the decomposition results could be used to identify forest. However, the range profile data is not available from a SAR so only the decomposition results are included in this discussion. For the decomposition approach to be effective, a threshold must be identified, above which, the landscape can be unambiguously identified as forest. Leveraging the strong volume response observed in forest canopies at both frequencies in Section 4.3, a threshold of $V_{FD} \geq 50\%$ for forested landscape and $V_{FD} < 50\%$ for non-forested landscape was applied. This simple threshold yields good agreement between observation and classification of the forested and non-forested classes with overall accuracies of 87% and 88% at 17.2 GHz and 9.6 GHz. Errors in the classification primarily occurred in the low-density stands of TVC which indicates that with an *FF* of 16% or less forests may be undetectable at these frequencies. Error also occurred at low incidence angles in Churchill where gaps were present in the near range of the FOV due to the spacing of trees. This error was associated with the 30 cm range resolution of UWScat in that the system is sensitive to the presence and absence of individual trees.

Given the strength of correlation between *FF* and V_{FD}, it is apparent these terms contain related information about forest biomass structure. The performance of V_{FD}, when used within the active-microwave model (8.1) proposed by Cohen et al. (2015) in place of *FF*, was evaluated for its ability to retrieve sub-canopy backscatter determined from numerical inversion (8.2) in which the cost function was minimized in a least squares scheme. Backscatter observations σ^o_{obs} at 17.2 GHz from sites 20 and 15 were used to iteratively fit the model against free parameters in the optimization in order to retrieve the sub-canopy signal ($\sigma^o_{snow,FP}$). Free parameters in the model include the forest canopy backscatter (σ^o_{canopy}), the effective canopy extinction coefficient (K'_e), and ($\sigma^o_{snow,FP}$). Two-way transmissivity ($t_{two\text{-}way}$) is given in (8.3), as defined by Montomoli et al. (2015), where K'_e is equivalent to the extinction coefficient (K_e) divided by the cosine of the incidence angle and FP describes the forest parameter used in the model (V_{FD} or *FF*, in this case). The model's skill at retrieving ($\sigma^o_{snow,FP}$) was evaluated, using both V_{FD} and *FF* as the forest parameter, by comparison with coincident observations of adjacent non-forested land (sites 5 & 6) which served as estimates of the true value of sub-canopy backscatter ($\sigma^o_{obs,snow}$).

$$\sigma^o_{total} = t_{two-way}\sigma^o_{snow,FP} + \left(1 - t_{two-way}\right)\sigma^o_{canopy} \tag{8.1}$$

$$min\left\{\sum\left[\sigma^o_{model}(\sigma^o_{snow,FP}, \sigma^o_{canopy}, K'_e, FP) - \sigma^o_{obs}\right]^2\right\} \tag{8.2}$$

$$t_{two-way} = e^{-2K'_eFP} \tag{8.3}$$

The inversion was implemented over the full range of incidence angles from 34° to 61° at 17.2 GHz (VV, HH and VH) and the results summary is presented in Figure 8.11. Note that a different scale was used for σ° in the top and bottom panels. Observations at site 15 were made from a height of about 9.5 m thus the range to target was substantially greater than at site 20, which resulted in a proportionally weaker response due to instrument range limitations. The forest parameters *FF* and V_{FD} demonstrated similar performance in retrieval of $\sigma^o_{snow,FP}$. A comparison of $\sigma^o_{snow,FP}$, when retrieved using *FF* and V_{FD}, revealed very strong correlation while RMSE values indicated similar performance when compared with $\sigma^o_{obs,snow}$. Furthermore, an aggregation of results for all polarizations, incidence angles and both sites provided overall RMSE values of 1.79 and 1.80 for *FF* and V_{FD}. The bias, calculated as an average bias of all incidence angles per site and polarization, was positive in most cases, showing the retrieval tended to overestimate. Large differences between $\sigma^o_{snow,FF}$ and $\sigma^o_{snow,V_{FD}}$ occurred where

there was disagreement between *FF* and *VFD*. For example, the largest difference (2.1 dB) occurred at site 15 with HH polarization and an incidence angle of 58°. This corresponded with an *FF* of 0.39 and a V_{FD} of 0.81; $\sigma^o_{snow,V_{FD}}$ was much closer to σ^o_{obs}which underscores the utility of V_{FD}. Differences between $\sigma^o_{snow,FP}$ and σ^o_{obs} were primarily attributed to differences between the sub-canopy environment and the adjacent non-forested land.

Given the similarity in performance between the two forest parameters, these results support the use of V_{FD} for the retrieval of $\sigma^o_{snow,FP}$ from beneath a canopy in place of *FF*. With similar levels of accuracy, the primary benefit of this method remains the ability to retrieve $\sigma^o_{snow,FP}$ without the use of ancillary data. As an additional benefit, given that K'_e was a free parameter in (2), using V_{FD} as the *FP* in (1) and (2) allowed for the estimation of forest canopy transmissivity without ancillary data.

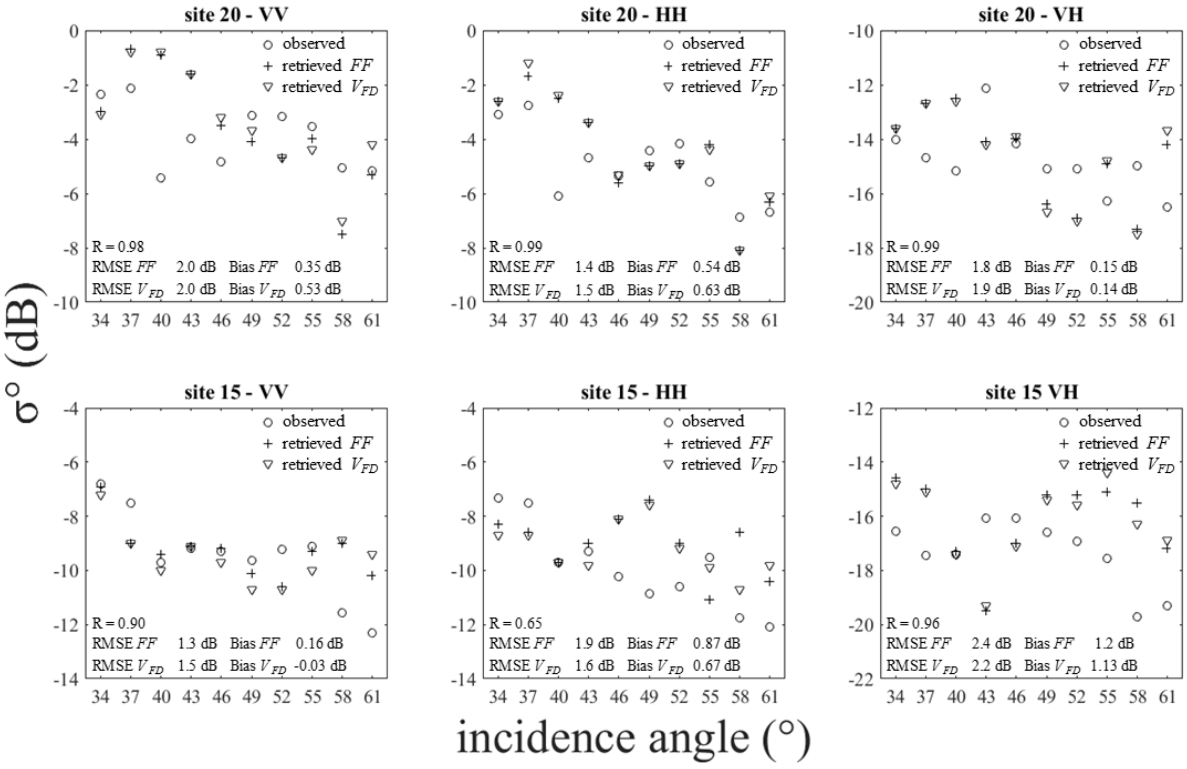

Figure 8-11. Results of $\sigma^o_{snow,FP}$ retrieval. Retrievals compared with observations from the adjacent non-forested sites. The RMSE and bias were averaged over all incidence angles. The correlation between $\sigma^o_{snow,FF}$ and $\sigma^o_{snow,V_{FD}}$ is shown.

8.8 Discussion

The results demonstrate the operational range of these methods for potential use in a SWE retrieval framework. These methods were able to identify forest with $FF > 16\%$, which represents a lower limit of sensitivity for UWScat. An airborne or spaceborne SAR instrument, with a coarser range resolution, may be less sensitive. This classification scheme was based on the average value of V_{FD} across an azimuth sweep, comprised of a varying number of independent samples instead of on a per-pixel basis. While these methods demonstrated the success of this classification scheme, it is recommended that it be repeated with airborne Ku- and X-band SAR data in order to fully assess the validity of this threshold for discriminating forested landscape.

The upper limit of applicability in dense forest canopy remains, however these methods will respond to naturally occurring gaps within a forest. If a forest has been identified as being too dense, there will still be occasional gaps in the canopy (eg. fallen trees, fire damage, etc.), identifiable by a reduction in V_{FD}. This method would be successful in retrieving SWE from within those gaps providing at least point estimates throughout the otherwise excluded dense forest region.

A limitation, which remains to be investigated, is the response of these methods to a land cover with more complex geometry than that which was observed in this study, including built environments or complex terrain. Dependent on their size and structure, these features could influence all three scattering mechanisms, but particularly V_{FD} since it captures all cross-polarized power. Complex built environments can cause co- and cross-polarization correlations which do not normally occur from natural distributed targets, violating the reflection symmetry assumption, thus artificially inflating V_{FD}. Adopting the 4-component method developed by Yamaguchi et al. (2005), which includes a helical scattering term associated with the scattering matrix of helices or circular polarization states often induced by built environments, could allow us to extend the methods in this study to include complex landscapes.

8.9 Conclusions

In this study UWScat, a ground-based radar scatterometer, was used to observe forested and non-forested landscapes at 9.6 GHz and 17.2 GHz, in a selection of terrestrial snow accumulation environments which included Churchill Manitoba, Tobermory Ontario, Grand Mesa Colorado, and TVC Northwest Territories. Forest canopy in a snow accumulation environment attenuated backscatter from the sub-canopy snow at 17.2 GHz, reducing sensitivity to SWE. At 9.6 GHz, forested sites consistently produced stronger backscatter than adjacent non-forested sites, but limited sensitivity to

SWE was observed. A larger difference in cross-polarized backscatter between forested and non-forested sites was observed which suggested an enhanced volume response from the canopy. Forested areas were identifiable by scatterometer range profiles, based on a significant increase in the number of inflection points, and by an increase in the proportion of volume scattering, as determined by the Freeman-Durden three-component decomposition model. A threshold was considered in order to distinguish forest from non-forested landscapes, and since range profiles are not available from SAR instruments, only the volume scattering proportion was used. A threshold of 50% volume scattering was used with good results to distinguish forest. From the results of the decompositions, it was suggested that the volume scattering proportion replace forest fraction as a means to scale backscatter emanating from the snowpack beneath a canopy in current SWE retrieval algorithms. This was tested in the retrieval of sub-canopy backscatter using the model of Cohen et al. (2015) and found to have similar performance to forest fraction. The use of V_{FD} has three distinct advantages: 1) It provides a current, real-time description of the forest condition; 2) It automatically accounts for incidence angle and canopy structure by providing a description of the scatterers encountered in each case without ancillary information; and 3) It provides coincident information on forest canopy in remote regions where no forest inventories or models exist. Results of a retrieval of sub-canopy snow backscatter showed similar accuracy when either *FF* or V_{FD} were used, however using V_{FD} should allow for a quicker operationalization of SWE retrieval with minimized complexity and a broader geographical range. An additional benefit of V_{FD} is it can be used within this model to estimate forest canopy transmissivity without ancillary data.

Before these methods are operationalized, some work remains to be completed. In order to use these methods in proximity to a built environment, adjustments to the decomposition should be made such as those suggested by Arii et al. (2011) or Yamaguchi et al. (2005) to account for the helical polarization state often introduced by irregularly shaped built environments. The threshold for distinguishing forest canopy should be tested on an airborne SAR in order to better test the accuracy of the classification since the scatterometer classification was not pixel based and included a variable number of samples in each result.

Overall, this study demonstrated sensitivity of 9.6 GHz and 17.2 GHz to a range of forest canopy conditions. These frequencies were shown to provide information linked to both forest biomass and snow accumulation with a useful application in SWE retrieval, which is something not currently possible at other frequencies. It also marked the first use of the Freeman-Durden three-component decomposition of scatterometer data at these frequencies.

8.10 Acknowledgements

The authors wish to thank NASA for support during the SnowEx17 field campaign, with special thanks to L. Brucker, K. Elder, and C. Hiemstra for their tremendous efforts. The authors also thank P. Marsh and B. Walker who facilitated the campaign in TVC and provided aerial photographs and meteorological data for that site. Special thanks are given to V. Vanthof for her efforts in the field and the Aurora Research Institute for logistical support. Acknowledgement is given to those involved in data collection during the Can-CSI/CASIX campaign and in Tobermory.

Chapter 9
Conclusions

9.1 Summary of work

The principal intent of this thesis was to develop knowledge of constraints for radar based SWE retrievals related to snowpack, vegetation, and subnivean conditions to improve retrieval accuracy. This included developing region-specific understanding of retrieval parameter variability that can help to mitigate uncertainty in SWE estimates with particular focus on stratigraphy, vegetation, and background scattering from subnivean soil. Ground-based radar scatterometer measurements at 17.2 GHz and 9.6 GHz, obtained with UWScat, provided data for evaluation in conjunction with coincident, *in situ* snowpack observations at sites in mid-latitude agricultural fields, coniferous forest, and arctic tundra. The four objectives were:

1. Demonstrate how physical processes driving the snow accumulation environment manifest regional outcomes in terms of parameterization and constraints.
2. Quantify effects of ice lenses, agricultural vegetation, and background scattering on retrievals.
3. Develop a means to constrain wind slab thickness in an arctic tundra snowpack.
4. Improve characterization of coniferous forest in a retrieval context.

The demonstrated importance of snow combined with the complexity of the snow accumulation environment and the potential for equifinality in SWE retrievals validate the need for this work, especially for successful operationalization of SWE retrievals in remote regions. The work contained in this thesis demonstrated how physical processes manifest regional outcomes which emphasize the need for regional constraints within SWE retrievals that leverage geographically distinct combinations of physical processes and environmental conditions. Such constraints have potential to simplify retrievals and, in some cases, provide information on the snowpack that may otherwise be lost due to snowpack or tree canopy attenuation. A series of unique and challenging experiments also quantified effects of ice lenses and vegetation on backscattered power along with that of the background scattering from underlying soil. This thesis provided a strong foundation for subsequent work from airborne and future spaceborne platforms to expand these ideas and identify the operational range and replicability of these results on a larger scale.

Following the preamble, characteristics and variability of terrestrial snow were discussed (Chapter 2), including common measurement techniques and their uncertainty. Fundamentals of the

radar power response were explored in Chapter 3, including an introduction to MEMS3&a which was used in Chapter 6. Chapter 4 presented a polarimetric description of a wave and its response to scattering. The FD3c, used in Chapters 7 and 8, was introduced. Since all radar measurements in this thesis were made with UWScat, a full instrument description was provided in Chapter 5.

In Chapter 6, the 17.2 GHz radar response of mid-latitude alfalfa fields in Maryhill and Englehart was explored through forward modeling and inversion of MEMLS3&a, in one of the very few mid-latitude snow radar experiments at this frequency. Scattering effects of vegetation and buried and surface ice lenses were also quantified. Separate retrieval algorithms were developed for Maryhill and Englehart based on snowpack conditions and optimization of Φ. Field conditions in Maryhill were classified as a maritime snow climate class while those in Englehart were classified as taiga snow according to the classification scheme of Sturm et al. (1995). For the Maryhill sites a single layer snowpack parameterization produced optimal results indicating that snowpack layers at this site were not radiometrically distinct. The optimal SWE retrieval resulted in an RMSE of 21.9 mm SWE using a mean bulk snow density while p_{ex} and h remained constrained free parameters. For the Englehart sites, a two-layer snowpack parameterization was optimal which was conceptualized as wind slab and depth hoar. The only free parameter was the wind slab p_{ex} which illustrated the radiometric significance of the upper snow layers at the site. Optimal retrieval parameterization resulted in an RMSE of 24.6 mm SWE. A soil subtraction scheme was tested to account for background scattering by subtracting snow-free, frozen ground measurements from the natural snow measurements prior to ingestion in the SWE retrieval algorithm. This improved retrieval results by 5.6 and 6.3 mm SWE for Maryhill and Englehart, respectively. Snow depths were constrained using *in situ* measurements which improved accuracy to 12.0 and 10.9 mm SWE for Maryhill and Englehart, respectively. These values compare well to the often-cited 30 mm accuracy requirement (eg. ESA, 2012). Retrieval accuracy for sites containing partially buried vegetation and ice lenses was 60.4 mm SWE RMSE. By constraining retrievals using *in situ* snow depth measurements, the retrieval RMSE improved to 21.1 mm SWE. Wet surface ice lenses and partially buried vegetation were observed to have the largest negative effect on retrieval accuracy and these observations benefited greatest from the use of *in situ* snow depths during retrieval which emphasized the need for detection of these features. The use of *in situ* snow depths was considered a local-scale solution.

Chapter 7 continued the exploration of stratigraphic constraints but in an arctic tundra environment. UWScat measurements in Trail Valley Creek at 17.2 GHz were combined with the FD3c decomposition to identify a means to constrain wind slab thickness in arctic SWE retrievals which is

important since arctic wind slab can introduce substantial attenuation limiting the radar response despite further accretion. Wind slab thickness was estimated from a positive linear relationship with the proportion of double-bounce scattering estimated from FD3c. The relationship was strongest at incidence angles ≥ 46° and where wind slab thickness ≥ 19 cm with the best results observed at 61° where wind slab thickness estimation resulted in an RMSE of 6.0 cm and wind slab layer SWE estimation RMSE of 5.5 mm when compared with *in situ* measurements. The double-bounce response in this range of incidence angle and wind slab thickness was associated with an extended path length through the wind slab layer where sparse scattering occurs, but becomes more likely as the path length increases, while scattering from subordinate snow and soil layers was minimized. Since a small double-bounce response was observed from snow-free ground, this method was recommended for use where depth hoar has developed, because the subnivean contribution to double-bounce scattering will likely be converted to volume scattering within the depth hoar layer.

Attenuation effects were also considered in Chapter 8 but in terms of coniferous forest canopy. UWScat measurements were made at 17.2 GHz and 9.6 GHz of coniferous forest near Churchill MB, Tobermory ON, Grand Mesa CO, and Trail Valley Creek NT. Peaks in the scatterometer range profiles were associated with forest canopy volume scattering, as determined from the FD3c, which was then compared with forest fraction obtained from optical imagery, demonstrating similar efficacy within the canopy transmission model of Cohen et al. (2015) to estimate subcanopy σ^o. A threshold of 50% V_{FD} was chosen, below which a scene was considered non-forested which worked well; The V_{FD} was sensitive to forest fraction exceeding 16%. While most SWE retrieval efforts from boreal forest make use of ancillary data, allometry, and canopy modeling, the use of V_{FD} introduces several important benefits: 1) it provides a current, real-time description of forest canopy, 2) it accounts for incidence angle and canopy geometry without ancillary information or canopy modeling, and 3) it provides canopy information in remote regions. With the retrieval of Cohen et al. (2015) it also allowed for the estimation of forest canopy transmissivity without ancillary forest data.

9.2 Limitations and uncertainty

9.2.1 Scaling

All radar measurements in this thesis were made with UWScat which enabled Ku- and X-band radar observations of snowpack, ice lenses, and vegetation at a fine scale. The methods described in previous chapters leveraged this to characterize and develop constraints based on target physical variation,

dielectric discontinuity, and scattering behaviour over short distances. While fine-scale observations from ground-based instruments such as UWScat facilitate controlled and customizable experiments, the spatial resolution, at 30 cm, is much finer than what is potentially available from spaceborne observations, permitting greater target isolation within scenes of greater homogeneity. For comparison, a recent spaceborne radar mission concept specified 250 m resolution with 50 m capability for observation of critical regions (Derksen et al., 2019) and prior to that, the CoReH20 mission proposal specified 50 m spatial resolution (Rott et al., 2010); measurements from such instruments will be sensitive to landscape scale variability while demonstrating less sensitivity to relatively small, discrete objects such as small, sparse trees with low-density canopy. Whereas UWScat was able to identify forest with an $FF > 16\%$ for example, this threshold need recalibration with coarse resolution measurements. Uncertainty therefore remains regarding the efficacy of the presented methods with spaceborne measurements and in particular, instrument sensitivity to subscale variability.

9.2.2 Logistical constraints

Logistical constraints associated with UWScat deployment prevented measurement over large scale spatial and temporal extents. With strong linkages to the discussion in Section 9.2.1, limited spatial sampling failed to replicate the variability that would be aggregated in a coarse resolution spaceborne pixel. The limited temporal sampling prevented a comprehensive understanding of the seasonal evolution of the snowpack and physical constraints, particularly at study sites outside of Maryhill where site access was more restrictive. Limited data presents uncertainty in terms of the range of applicability of the developed methods. Examples of this include understanding the temporal and spatial domain of single-layer and two-layer snowpack parameterizations in the mid-latitude region. More observations are needed to determine maximum detectable wind slab thickness and to develop more confidence in the relationship between wind slab thickness and double bounce scattering, particularly where wind slab thickness exceeds 19 cm. Despite these constraints, the work provides a strong foundation and direction for future study and could be used to generate initial constraints in a SWE retrieval.

9.2.3 Assumptions of FD3c

Chapters 7 and 8 made use of the FD3c decomposition in its original form which was optimized for forest canopy and makes important assumptions including reflection symmetry and modelling scatterers as randomly oriented dipoles. Since the FD3c decomposition was developed for forest canopy, these assumptions are better suited to Chapter 8, but they may have been less appropriate in

Chapter 7 where the model was used on radar measurements of a snowpack. In snowpacks with well-developed depth hoar, the snow grains may align in a vertical chain-like arrangement which exhibits order and is not random. In other snow conditions, while snow grains may be randomly oriented, modeling them as dipoles may be inappropriate, especially for the small, fractured grains found in wind slab or rounded grains common during equilibrium grain growth. Furthermore, parametrization of this model may become more complicated for snowpacks such as those in the arctic tundra which have distinct layers of wind slab and depth hoar with distinct grain structure and alignment. These assumptions will directly affect the estimated volume scattering proportion; however, the magnitude and direction of the effects is unclear. The original form of the FD3c decomposition was well suited to forest observations, and although it was not optimized for snow, the original form of the model provided strong insight into the nature of scattering within a snowpack. Furthermore, the relative contributions of surface and double-bounce scattering were independent of volume scattering assumptions which allowed for the estimation of wind slab thickness despite questions surrounding the representation of volume scatterers.

9.3 Recommendations

In this thesis, the potential effects of partially buried vegetation and wet surface ice lenses on backscatter and SWE retrievals at 17.2 GHz and 9.6 GHz were demonstrated. Wet surface ice lenses resulted in an underestimation of SWE by about 100 mm while the effects of partially buried vegetation resulted in an overestimation of SWE by a similar amount. Furthermore, coniferous forest canopy may lead to an underestimation of subcanopy SWE. Given the potential influence of vegetation and ice lenses on radar backscatter at these frequencies, it is important that such conditions be detected prior to SWE retrieval. Current radar-based efforts to detect green vegetation include polarimetric analysis, while detection of ice lenses leverages variation in H-polarized passive microwave brightness temperature measurements or makes use of snowpack modeling. However, more work is required to improve reliability of these methods, and, in terms of vegetation, detection techniques should include capacity for all potential vegetation types, beyond just agricultural residue or coniferous forest. Polarimetric modeling, analysis and decomposition is recommended to address these questions which demands fully polarimetric radar instruments. Decompositions should be modified to fit the composition of snow more closely. Furthermore, these methods should be integrated into radiative transfer models which must be able to deal with complex scenes including ice-layered snow and the

effects of partially buried vegetation. These conditions are most common in mid-latitude regions, but they are also expected to increase in frequency in the north with the projected warming.

Given the absence of spaceborne radar measurements at 17.2 GHz, polarimetric airborne measurements of snow should be made of natural snow in mid-latitude and arctic tundra environments to support and advance the work within this thesis. The benefits would be twofold. Firstly, this would allow for verification of the methods described in Chapters 6 through 8, given that the added datapoints would enhance the significance of the results while providing additional understanding of the spatial and temporal validity of methods that was not feasible during the field campaigns with UWScat. This should include acquisition of snow-free, frozen ground, where possible, to characterize background scattering and implement soil subtraction. It is also suggested to leverage regular agricultural landscapes to constrain SWE retrievals, which will require regional-level landscape observations. Secondly, an airborne platform should collect sufficient data to upscale and replicate coarse resolution spaceborne SAR data, until such data become available, since this was not possible with UWScat. This would permit exploration and adaptation of the methods herein to a coarse-resolution platform and enhance understanding of the effects of the increased heterogeneity within a larger pixel. A strong candidate for such work is the recently funded airborne CryoSAR instrument which is expected to launch during the winter of 2021-2022. Synergistic benefits may also be realized from collaboration with the multi-year NASA SnowEx campaign and the proposed Terrestrial Snow Mass Mission from Environment and Climate Change Canada and the Canadian Space Agency.

Finally, the effects of snowpack attenuation should be better integrated into retrieval efforts. This is particularly the case when implementing a soil subtraction scheme to account for background scattering from the soil (eg. Zhu et al., 2018). Neglecting snowpack attenuation during soil subtraction may result in an underestimation of retrieved SWE in magnitude proportional to the magnitude of attenuation which may occur in deeper snow or that featuring substantial wind slab or scattering. Snowpack attenuation should also be considered in conjunction with the methods described in Chapter 7 to improve SWE retrievals of arctic tundra snow, or any snowpack featuring a substantial wind slab layer. Once the wind slab thickness has been estimated, the backscattered response could then be scaled by the effective attenuation thus correcting the measured backscatter for input into the SWE retrieval.

References

Adams, E. E. & D. A. Miller. (2003). Ice crystals grown from vapor onto an orientated substrate: application to snow depth-hoar development and gas inclusions in lake ice. Journal of Glaciology, 49(164), 8–12. doi: 10.3189/172756503781830953.

An, W., Cui, Y., & Yang, J. (2010). Three-component model-based decomposition for polarimetric SAR data. IEEE Transactions on Geoscience and Remote Sensing, 48(6), 2732–2739. doi: 10.1109/TGRS.2010.2041242.

Antropov, O., Rauste, Y., & Hame, T. (2011). Volume scattering modeling in PolSAR decompositions: Study of ALOS PALSAR data over boreal forest. IEEE Transactions on Geoscience and Remote Sensing, 49(10), 3838–3848. doi: 10.1109/TGRS.2011.2138146.

Arii, M., Van Zyl, J. J., & Kim, Y. (2010). A general characterization for polarimetric scattering from vegetation canopies. IEEE Transactions on Geoscience and Remote Sensing, 48(9), 3349–3357. doi: 10.1109/TGRS.2010.2046331.

Arii, M., Van Zyl, J. J., & Kim, Y. (2011). Adaptive model-based decomposition of polarimetric SAR covariance matrices. IEEE Transactions on Geoscience and Remote Sensing, 49(3), 1104–1113. doi: 10.1109/TGRS.2010.2076285.

Armstrong, R. L. (1980). An analysis of compressive strain in adjacent temperature- gradient and equi-temperature layers in a natural snow cover. Journal of Glaciology, 26(94), 283–289. doi: 10.1017/S0022143000010820.

Arons, E. M., & Colbeck, S. C. (1995). Geometry of heat and mass transfer in dry snow: A review of theory and experiment. Reviews in Geophysics, 33(4), 463–493. doi: 10.1029/95RG02073.

Atwood, D. K., Gunn, G. E., Roussi, C., Wu, J., Duguay, C., & Sarabandi, K. (2015). Microwave backscatter from arctic lake ice and polarimetric implications. IEEE Transactions on Geoscience and Remote Sensing, 53(11), 5972–5982. doi: 10.1109/TGRS.2015.2429917.

Ballester-Berman, D. J., & Lopez-Sanchez, J. M. (2010). Applying the Freeman-Durden decomposition concept to polarimetric SAR interferometry. IEEE Transactions on Geoscience and Remote Sensing, 48(1), 466–479. doi: 10.1109/TGRS.2009.2024304.

Balzter, H., Baker, J. R., Hallikainen, M., & Tomppo, E. (2017). Retrieval of timber volume and snow water equivalent over a Finnish boreal forest from airborne polarimetric synthetic aperture radar. Internalional Journal of Remote Sensing, 23(16), 3185-3208. doi: 10.1080/01431160110076199.

Barnett, T. P., Adam, J. C., & Lettenmaier, D. P. (2005). Potential impacts of a warming climate on water availability in snow-dominated regions. Nature, 438, 303–309. doi: 10.1038/nature04141.

Bartelt, P., & Lehning, M. (2002). A physical SNOWPACK model for the Swiss avalanche warning: Part I: Numerical model. Cold Regions Science and Technology, 35(3), 123–145. doi: 10.1016/S0165-232X(02)00074-5.

Benson, C. S., & Sturm, M. (1993). Structure and wind transport of seasonal snow on the Arctic slope of Alaska. Annals of Glaciology, 18, 261–267. doi: 10.3189/s0260305500011629.

Bokhorst, S., Pedersen, S. H., Brucker, L., Anisimov, O., Bjerke, J. W., Brown, R. D., Ehrich, D., Essery, R. L. H., Heilig, A., Ingvander, S. Johnasson, C., Johansson, M., Jónsdóttir, S., Inga, N., Luojus, K., Macelloni, G., Mariash, H., McLennan, D., Rosqvist, G. N., … Callaghan, T. V. (2016). Changing arctic snow cover: A review of recent developments and assessment of future needs for observations, modelling, and impacts. Ambio, 45, 516-537. doi: 10.1007/s13280-016-0770-0.

Bormann, K. J., Brown, R. D., Derksen, C., & Painter, T. H. (2018). Estimating snow-cover trends from space. Nature Climate Change, 8(11), 924–928. doi: 10.1038/s41558-018-0318-3.

Bormann, K. J., Westra, S., Evans, J. P., & McCabe, M. F. (2013). Spatial and temporal variability in seasonal snow density. Journal of Hydrology, 484, 63-73. doi: 10.1016/j.jhydrol.2013.01.032.

Brandt, J. P., Flannigan, M. D., Maynard, D. G., Thompson, I. D., & Volney, W. J. A. (2013). An introduction to Canada's boreal zone: Ecosystem processes, health, sustainability, and environmental issues. Environmental Reviews, 21(4), 207–226. doi: 10.1139/er-2013-0040.

Brown, R. D. (2000). Northern Hemisphere snow cover variability and change. 1915-97. Journal of Climate, 13(13), 2339–2355. doi: 10.1175/1520-0442(2000)013<2339:NHSCVA>2.0.CO;2.

Brown, R. D., & Mote, P. W. (2009). The response of northern hemisphere snow cover to a changing climate. Journal of Climate, 22(8), 2124–2145. doi: 10.1175/2008JCLI2665.1.

Brown, R., Schuler, D. V., Bulygina, O., Derksen, C., Luojus, K., Mudryk, L., Wang, L., & Yang, D. (2017). Arctic terrestrial snow cover. In Snow, Water, Ice, and Permafrost in the Arctic (SWIPA) 2017 (pp. 25–64). Arctic Monitoring and Assessment Programme (AMAP): Oslo, Norway.

Brucker, L., Royer, A., Picard, G., Langlois, A., & Fily, M. (2011). Hourly simulations of the microwave brightness temperature of seasonal snow in Quebec, Canada, using a coupled snow evolution-emission model. Remote Sensing of Environment, 115(8), 1966–1977. doi: 10.1016/j.rse.2011.03.019.

Brun, E., David, P., Sudul, M., & Brunot, G. (1992). A numerical model to simulate snow-cover stratigraphy for operational avalanche forecasting. Journal of Glaciology, 38(128),13–22. doi: 10.3189/s0022143000009552.

Campbell, B. A. (2002). Radar remote sensing of planetary surfaces. Cambridge: Cambridge University Press.

Canada Energy Regulator. (2021). Provincial and Territorial Energy Profiles. Retrieved from https://www.cer-rec.gc.ca/en/data-analysis/energy-markets/provincial-territorial-energy-profiles/provincial-territorial-energy-profiles-ontario.html.

Canadian Centre for Remote Sensing. (2015). Radar polarimetry. Retrieved from https://www.nrcan.gc.ca/earth-sciences/geomatics/satellite-imagery-and-air-photos/satellite-imagery-and-products/educational-resources/tutorial-radar-polarimetry/9579.

Canadian Soil Information Service. Soil survey of Bruce County (Report No. 16 of the Ontario Soil Survey). Retrieved from https://bit.ly/2EzxXDJ.

Caroll, T. (1977). A comparison of the CRREL 500 cm3 tube and the ILTS 200 and 100 cm3 box cutters used for determining snow densities. Journal of Glaciology, 18(79), 334-337. doi:10.3189/S0022143000021420.

Chang, W., Tan, S., Lemmetyinen, J., Tsang, L., Xu, X., & Yueh, S. H. (2014). Dense media radiative transfer applied to SnowScat and SnowSAR. IEEE Journal of Selected Topics in Applied Earth Observation Remote Sensing, 7(9), 3811–3825. doi: 10.1109/JSTARS.2014.2343519.

Cloude, S. R. (1992). Uniqueness of Target Decomposition Theorems in Radar Polarimetry. In Boerner, W.-, M., Brand, H., Cram, L.A., Holm, W.A., Stein, D.E., Wiesbeck, W. et al. (Eds.), Direct and Inverse Methods in Radar Polarimetry, Part 1, NATO ASI Series C (350) (pp. 267-296). Kluwer: Norwell.

Cloude, S. R. (2010). Polarisation. Applications in remote sensing. New York: Oxford.

Cloude, S. R., & Pottier, E. (1996). A Review of target decomposition theorems in radar polarimetry. IEEE Transactions on Geoscience and Remote Sensing, 34(2), 498–518. doi: 10.1109/36.485127.

Colbeck, S. C. (1980). Thermodynamics of snow metamorphism due to variations in curvature. Journal of Glaciology, 26(94), 291–301. doi: 10.1017/S0022143000010832.

Colbeck, S. C. (1982). An overview of seasonal snow metamorphism. Reviews of Geophysics and Space Physics, 20(1), 45–61. doi: 10.1029/RG020i001p00045.

Colbeck, S. C. (1983). Theory of metamorphism of dry snow. Journal of Geophysical Research, 88(C9), 45–61. doi: 10.1029/JC088iC09p05475.

Colbeck, S. C. (1986). Classification of seasonal snow cover crystals. Water Resources Research, 22(9 S), 59S-70S. doi: 10.1029/WR022i09Sp0059S.

Colbeck, S. C. (1987). A review of the metamorphism and classification of seasonal snow cover crystals. Proceedings of the Davos Symposium, IAHS Publ., 162, 3-34. Retrieved from http://hydrologie.org/redbooks/a162/iahs_162_0003.pdf.

Colbeck, S. C. (1991). The layered character of snow covers. Reviews of Geophysics, 29(1), 81–96. doi: 10.1029/90RG02351.

Cohen, J. (1994). Snow cover and climate. Weather, 49(5), 150-156. doi:10.1002/j.1477-8696.1994.tb05997.x.

Cohen, J., Lemmetyinen, J., Pulliainen, J., Heinila, K., Montomoli, F., Seppanen, J., & Hallikainen, M. T. (2015). The effect of boreal forest canopy in satellite snow mapping-A multisensor analysis. IEEE Transactions on Geoscience and Remote Sensing, 53(12), 6593–6607. doi: 10.1109/TGRS.2015.2444422.

Conger, S. M., & McClung, D. M. (2009). Comparison of density cutters for snow profile observations. Journal of Glaciology, 55(189), 163–169. doi: 10.3189/002214309788609038.

Cui, Y., Xiong, C., Lemmetyinen, J., Shi, J., Jiang, L., Peng, B., Li, H., Zhao, T., Ji, D., & Hu, T. (2016). Estimating snow water equivalent with backscattering at X and Ku band based on absorption loss. Remote Sensing, 8(6): 505. doi: 10.3390/rs8060505.

Cumming, W. A. (1952). The dielectric properties of ice and snow at 3.2 centimeters. Journal of Applied Physics, 23(7), 768–773. doi: 10.1063/1.1702299.

Deems, J. S., Painter, T. H., & Finnegan, D. C. (2013). Lidar measurement of snow depth: A review. Journal of Glaciology, 59(215), 467–479. doi: 10.3189/2013JoG12J154.

Denoth, A. (1994). An electronic device for long-term snow wetness recording. Annals of Glaciology, 19, 104–106. doi: 10.3189/s0260305500011058.

Derksen, C., & Brown, R. (2012). Spring snow cover extent reductions in the 2008-2012 period exceeding climate model projections. Geophysical Research Letters, 39(L19504), 1–6. doi: 10.1029/2012GL053387.

Derksen, C., Lemmetyinen, J., King, J., Belair, S., Garnaud, C., Lapointe, M., Crevier, Y., Burbidge, G., & Siqueira, P. (2019). A dual-frequency Ku-band radar mission concept for seasonal snow. IEEE International Geoscience and Remote Sensing Symposium (IGARSS), 5742–5744. doi: 10.1109/IGARSS.2019.8898030.

Derksen, C., Lemmetyinen, J., Toose, P., Silis, A., Pulliainen, J., & Sturm, M. (2014). Physical properties of Arctic versus subarctic snow: Implications for high latitude passive microwave snow water equivalent retrievals. Journal of Geophysical Research Atmospheres, 119(12), 7254–7270. doi: 10.1002/2013JD021264.

Derksen, C., Smith, S.L., Sharp, M., Brown, L., Howell, S., Copland, L., Mueller, D. R., Gauthier, Y., Fletcher, C. G., Tivy, A., Bernier, M., Bourgeois, J., Brown, R., Burn, C. R., Duguay, C., Kushner, P., Langlois, A., Lewkowicz, A. G., Royer, A., & Walker, A. (2012). Variability and change in the Canadian cryosphere. Climate Change, 115(1), 59–88. doi: 10.1007/s10584-012-0470-0.

Derksen, C., Sturm, M., Liston, G. E., Holmgren, J., Huntington, H., Silis, A., & Solie, D. (2009). Northwest Territories and Nunavut snow characteristics from a subarctic traverse: Implications for passive microwave remote sensing. Journal of Hydrometeorology, 10(2), 448–463. doi: 10.1175/2008jhm1074.1.

Derksen, C., Teich, M., Brady, M., & King, J. (2017). SnowEx17 SnowMicroPen (SMP) raw Penetration force profiles: Version 1; NASA National Snow and Ice Data Center, Distributed Active Archive Center: Boulder, CO, USA. doi: 10.5067/ZPOLBRHVWG5V.

Dobson, M. C., Pierce, L., Sarabandi, K., Ulaby, F. T., & Sharik, T. (1992a). Preliminary analysis of ERS-1 SAR for forest ecosystem studies. IEEE Transactions on Geoscience and Remote Sensing, 30, 203–211. doi: 10.1109/36.134071.

Dobson, M. C., Ulaby, F. T., Le Toan, T., Beaudoin, A., Kasischke, E. S., & Christensen, N. (1992b). Independence of radar backscatter on coniferous forest biomass. IEEE Transactions on Geoscience and Remote Sensing, 30(2), 412–415. doi: 10.1109/36.134090.

Dobson, M. C., Ulaby, F., & Pierce, L. (1995). Land-cover classification and estimation of terrain attributes using synthetic aperture radar. Remote Sensing of Environment, 51(1), 199–214. doi: 10.1016/0034-4257(94)00075-X.

Domine, F., Barrere, M., & Morin, S. (2016). The growth of shrubs on high Arctic tundra at Bylot Island: impact on snow physical properties and permafrost thermal regime. Biogeosciences Discussions, 13(23), 6471-6486. doi: 10.5194/bg-13-6471-2016.

Domine, F., Barrere, M., Sarrazin, D., Morin, S., & Arnaud, L. (2015). Automatic monitoring of the effective thermal conductivity of snow in a low-Arctic shrub tundra. The Cryosphere, 9(3), 1265–1276. doi: 10.5194/tc-9-1265-2015.

Domine, F., Salvatori, R., Legagneux, L., Salzano, R., Fily, M., & Casacchia, R. (2006). Correlation between the specific surface area and the short wave infrared (SWIR) reflectance of snow. Cold Regions Science and Technology, 46(1), 60–68. doi: 10.1016/j.coldregions.2006.06.002.

Dozier, J., Bair, E. H., & Davis, R. E. (2016). Estimating the spatial distribution of snow water equivalent in the world's mountains. Wiley Interdisciplinary Reviews: Water, 3(3), 461–474. doi: 10.1002/wat2.1140.

Durand, M., Kim, E. J., & Margulis, S. A. (2008). Quantifying uncertainty in modeling snow microwave radiance for a mountain snowpack at the point-scale, including stratigraphic effects. IEEE Transactions on Geoscience and Remote Sensing, 46(6), 1753–1767. doi: 10.1109/TGRS.2008.916221.

Durden, S. L., Van Zyl, J. J., & Zebker, H. A. (1989). Modeling and observation of the radar polarization signature of forested areas. IEEE Transactions on Geoscience and Remote Sensing, 27(3), 290–301. doi: 10.1109/36.17670.

Elachi, C., Kuga, Y., McDonald, K. C., Sarabandi, K., Senior, T. B. A., Ulaby, F. T., van Zyl, J. J., Whitt, M. W., & Zebker, H. A. (1990). Radar polarimetry for geoscience applications. Ulaby, F. T., Elachi, C. (Ed.). Norwood: Artech House Inc.

Elder, K., Brucker, L., Hiemstra, C., & Marshall, H. (2018). SnowEx17 community snow pit measurements: Version 1; Boulder: NASA National Snow and Ice Data Center, Distributed Active Archive Center. doi: 10.5067/Q0310G1XULZS.

Environment and Climate Change Canada. (2015). Canadian climate normals. Retrieved from https://climate.weather.gc.ca/climate_normals/index_e.html.

Environment and Climate Change Canada. (2018a). Canadian climate normals 1981–2010 station data—Inuvik A Northwest Territories. Retrieved from https://bit.ly/2GFYkdR.

Environment and Climate Change Canada. (2018b). Canadian climate normals 1981–2010 station data—Churchill A Manitoba. Retrieved from https://bit.ly/2LoH631.

Environment and Climate Change Canada (2018c). Canadian climate normals 1981–2010 station data—Wiarton A Ontario. Retrieved from https://bit.ly/2QYA5LR.

Environment and Climate Change Canada (2018d). Historical data. Retrieved from https://bit.ly/2JjRnPp.

ESA. (2012). Report for Mission Selection: CoReH20 (Report ESA SP-1324/2; 3 volume series), Noordwijk: European Space Agency.

Evans, D. L., Farr, T. G., van Zyl, J. J., & Zebker, H. A. (1988). Radar polarimetry: Analysis tools and applications. IEEE Transactions on Geoscience and Remote Sensing, 26(6), 774-789. doi: 10.1109/36.7709.

Fierz, C., Armstrong, R. L., Durand, Y., Etchevers, P., Greene, E., McClung, D. M., Nishimura, K., Satyawali, P. K., & Sokratov, S. A. (2009). The international classification for seasonal snow on the ground (IHP-VII Technical Documents in Hydrology No 83, IACS Contribution no. 1). Paris: UNESCO-IHP.

Flanner, M. G., Shell, K. M., Barlage, M., Perovich, D. K., & Tschudi, M. A. (2011). Radiative forcing and albedo feedback from the Northern Hemisphere cryosphere between 1979 and 2008. Nature Geoscience, 4(3), 151–155. doi: 10.1038/ngeo1062.

Freeman, A. (2007). Fitting a two-component scattering model to polarimetric SAR data from forests. IEEE Transactions on Geoscience and Remote Sensing, 45(8), 2583–2592. doi: 10.1109/TGRS.2007.897929.

Freeman, A., & Durden, S. L. (1993). A three-component scattering model to describe polarimetric SAR data. Proceedings of SPIE (1748), Radar Polarimetry, 213–224. doi: 10.1117/12.140618.

Freeman, A., & Durden, S. L. (1998). A three-component scattering model for polarimetric SAR data. IEEE Transactions on Geoscience and Remote Sensing, 36(3), 963–973. doi: 10.1109/36.673687.

Fung, A. K., Li, Z., & Chen, K. S. (1992). Backscattering from a randomly rough dielectric surface. IEEE Transactions on Geoscience and Remote Sensing, 30(2), 356–369. doi: 10.1109/36.134085.

Fung, A. K., Liu, W. Y., Chen, K. S., & Tsay, M. K. (2002). An improved IEM model for bistatic scattering from rough surfaces. Journal of Electromagnetic Waves and Applications, 16(5), 689-702. doi: 10.1163/156939302X01119.

Gallet, J. -C., Domine, F., Zender, C. S., & Picard, G. (2009). Measurement of the specific surface area of snow using infrared reflectance in an integrating sphere at 1310 and 1550 nm. The Cryosphere, 3(2), 167-182. doi: 10.5194/tc-3-167-2009.

Geldsetzer, T. (2009). The dielectric and polarimetric microwave scattering properties of snow covered sea ice. Ph.D. Thesis, University of Calgary, Calgary, Canada. doi: 10.11575/PRISM/2580.

Geldsetzer, T., Mead, J. B., Yackel, J. J., Scharien, R. K., & Howell, S. E. L. (2007). Surface-based polarimetric C-band scatterometer for field measurements of sea ice. IEEE Transactions on Geoscience and Remote Sensing, 45(11), 3405–3416. doi: 10.1109/TGRS.2007.907043.

Grenfell, T. C., & Warren, S. G. (1999). Representation of a nonspherical ice particle by a collection of independent spheres for scattering and absorption of radiation. Journal of Geophysical Research, 104(D24), 31697–31709. doi: 10.1029/1999JD900496.

Goodison, B. E., Ferguson, H. L. & McKay, G. A. (1981) Measurement and data analysis. In D. M. Gray & D. H. Male (Eds.), Handbook of Snow, Principles, Processes, Management, and Use. (pp. 191–274). Willowdale: Pergamon Press.

Gunn, G. E., Brogioni, M., Duguay, C., Macelloni, G., Kasurak, A., & King, J. (2015a). Observation and modeling of X- and Ku-band backscatter of snow-covered freshwater lake ice. IEEE Journal of Selected Topics in Applied Earth Observations and Remote Sensing, 8(7), 3629–3642. doi: 10.1109/JSTARS.2015.2420411.

Gunn, G. E., Duguay, C. R., Atwood, D. K., King, J., & Toose, P. (2018). Observing scattering mechanisms of freshwater lake ice using polarimetric RADARSAT-2 (C-band) and UW-Scat (X- and Ku-bands). IEEE Transactions on Geoscience and Remote Sensing, 56(5), 2887-2903. doi: 10.1109/TGRS.2017.2786158.

Gunn, G. E., Duguay, C. R., Brown, L. C., King, J., Atwood, D., & Kasurak, A. (2015b). Freshwater lake ice thickness derived using surface-based X- and Ku-band FMCW scatterometers. Cold Regions Science and Technology, 120, 115-126. doi: 10.1016/j.coldregions.2015.09.012.

Hajnsek, I., Jagdhuber, T., Schön, H., & Papathanassiou, K. P. (2009). Potential of estimating soil moisture under vegetation cover by means of PolSAR. IEEE Transactions on Geoscience and Remote Sensing, 47(2), 442–454. doi: 10.1109/TGRS.2008.2009642.

Hallikainen, M., Ulaby, F. T., & Abdelrazik, M. (1986). Dielectric properties of snow in the 3 to 37 GHz range. IEEE Transactions on Antennas and Propagation, 34(11). 1329-1340. doi: 10.1109/TAP.1986.1143757.

Hall, D. K., Kelly, R. E. J., Foster, J. L., & Chang, A. T. C. (2005). Estimation of snow extent and snow properties. In Anderson, M.G. (Ed.), Encyclopedia of Hydrological Sciences (pp. 811-829). doi: 10.1002/0470848944.hsa062.

Harlow, C., & R. Essery. (2012), Tundra snow emissivities at MHS frequencies: MEMLS validation using airborne microwave data measured during CLPX-II. IEEE Transactions on Geoscience and Remote Sensing, 50(11), 4262–4278. doi: 10.1109/TGRS.2012.2193132.

Henderson, G. R., Peings, Y., Furtado, J. C., & Kushner, P. J. (2018). Snow-atmosphere coupling in the Northern Hemisphere. Nature Climate Change, 8(11), 954-963. doi:10.1038/s41558-018-0295-6.

IGOS. (2007). Integrated global observing strategy cryosphere theme report – For the monitoring of our environment from space and from Earth (Report: WMO/TD-No. 1405). Geneva: World Meteorological Organization.

Johnson, J. B., & Marks, D. (2004). The detection and correction of snow water equivalent pressure sensor errors. Hydrological Processes, 18(18), 3513–3525. doi: 10.1002/hyp.5795.

Jonas, T., Marty, C., & Magnusson, J. (2009). Estimating the snow water equivalent from snow depth measurements in the Swiss Alps. Journal of Hydrology, 378(1–2), 161–167. doi: 10.1016/j.jhydrol.2009.09.021.

Judson, A., & Doesken, N. (2000). Density of freshly fallen snow in the central Rocky Mountains. Bulletin of the American Meteorological Society, 81(7), 1577–1587. doi: 10.1175/1520-0477(2000)081<1577:DOFFSI>2.3.CO;2.

Kelly, R. (2009). The AMSR-E snow depth algorithm: Description and initial results. Journal of the Remote Sensing Society of Japan, 29(1), 307-317. doi: 10.11440/rssj.29.307.

Kelly, R., & Thompson, A. (2018). SnowEx17 Ground-based UWScat Ku- and X-band frequency modulated continuous wave radar: Version 1. Boulder: NASA National Snow and Ice Data Center, Distributed Active Archive Center. doi: 10.5067/ZW3UUYUZRYJO.

Kendra, J. R., Sarabandi, K., & Ulaby, F. T. (1998). Radar measurements of snow: experiment and analysis. IEEE Transactions on Geoscience and Remote Sensing, 36(3), 864–879. doi: 10.1109/36.673679.

Kershaw, P. G., & McCulloch, J. Midwinter snowpack variation across the Arctic treeline, Churchill, Manitoba, Canada. Arctic, Antarctic and Alpine Research, 39(1), 9–15. doi: 10.1657/1523-0430(2007)39[9:MSVATA]2.0.CO;2.

Kim, D. J., Choi, S. I., Ryszard, O., Feyen, J., & Kim, H. S. (2000). Determination of moisture content in a deformable soil using time-domain reflectometry (TDR). European Journal of Soil Science, 51(1), 119–127. doi: 10.1046/j.1365-2389.2000.00284.x.

Kinar, N. J., & Pomeroy, J. W. (2015). Measurement of the physical properties of the snowpack. Reviews of Geophysics, 53(2), 481-544. doi: 10.1002/2015RG000481.

King. J. M. L.(2014). Remote Sensing Observations of Tundra Snow with Ku- and X-band Radar. Ph.D. Thesis, University of Waterloo, Waterloo, Canada. Retrieved from http://hdl.handle.net/10012/8218.

King, J., Derksen, C., Toose, P., Langlois, A., Larsen, C., Lemmetyinen, J., Marsh, P., Montpetit, B., Roy, A., Rutter, N., & Sturm, M. (2018). The influence of snow microstructure on dual-frequency radar measurements in a tundra environment. Remote Sensing of Environment, 215(15), 242–254. doi: 10.1016/j.rse.2018.05.028.

King, J. M. L., Kelly, R., Kasurak, A., Duguay, C., Gunn, G., & Mead, J. B. (2013). UW-Scat : A ground-based dual-frequency scatterometer for observation of snow properties. IEEE Geoscience and Remote Sensing Letters. 10(3), 528–532. doi: 10.1109/LGRS.2012.2212177.

King, J., Kelly, R., Kasurak, A., Duguay, C., Gunn, G., Rutter, N., Watts, T., & Derksen, C. (2015). Spatio-temporal influence of tundra snow properties on Ku-band (17.2 GHz) backscatter. Journal of Glaciology, 61(226) 267–279. doi: 10.3189/2015JoG14J020.

Kokhanovsky, A. A., & Zege, E. P. (2004). Scattering optics of snow. Applied Optics, 43(7), 1589-1602. doi: 10.1364/AO.43.001589.

Kujala, K., Seppälä, M., & Holappa, T. (2008). Physical properties of peat and palsa formation. Cold Regions Science and Technology, 52(3), 408–414. doi: 10.1016/j.coldregions.2007.08.002.

Kukula, G. J. (1978). Recent Changes in Snow and Ice. In Gribbin, J. (Ed.) Climatic Change (pp. 115-129). Cambridge University Press, Cambridge.

Kunkel, K. E., Robinson, D. A., Champion, S., Yin, X., Estilow, T., & Frankson, R.M. (2016). Trends and extremes in northern hemisphere snow characteristics. Current Climate Change Reports, 2, 65–73. doi: 10.1007/s40641-016-0036-8.

Langlois, A., Brucker, L., Kohn, J., Royer, A., Derksen, C., Cliche, P., Picard, G., Willemet, J. M. & Fily, M. (2009). Simulation of snow water equivalent (SWE) using thermodynamic snow models in Québec, Canada. Journal of Hydrometeorology, 10(6), 1447–1463. doi: 10.1175/2009JHM1154.1.

Larue, F., Royer, A., De Sève, D., Roy, A., Picard, G., & Vionnet, V. (2018). Validation and optimization of coupled snowpack evolution and microwave emission model over north-eastern Canada. Water Resources Research, 54(7), 4823-4848. doi: 10.1029/2017WR022132.

Lee, J-. S., Grunes, M. R., Pottier, E., & Ferro-Famil, L. (2004). Unsupervised terrain classification preserving polarimetric scattering characteristics. IEEE Transactions on Geoscience and Remote Sensing, 42(4), 722–731. doi: 10.1109/TGRS.2003.819883.

Lee, J-. S., & Pottier, E. (2009). Polarimetric radar imaging: From basics to applications. Boca Raton: CRC Press.

Leinss, S., Kontu, A., Löwe, H., & Proksch, M. (2020). Modeling the evolution of the structural anisotropy of snow. Cryosphere, 14(1), 51–75. doi: 10.5194/tc-14-51-2020.

Leinss, S., Wiesmann, A., Lemmetyinen, J., & Hajnsek, I. (2015). Snow water equivalent of dry snow measured by differential interferometry. IEEE Journal of Selected Topics in Applied Earth Observation and Remote Sensing, 8(8), 3773–3790. doi: 10.1109/JSTARS.2015.2432031.

Lemmetyinen, J., Derksen, C., Rott, H., Macelloni, G., King, J., Schneebeli, M., Wiesmann, A., Läppanen, L, Kontu, A., & Pulliainen, J. (2018). Retrieval of effective correlation length and snow water equivalent from radar and passive microwave measurements. Remote Sensing, 10(2), 170. doi: 10.3390/rs10020170.

Lemmetyinen, J., Kontu, A., Pulliainen, J., Vehviläinen, J., Rautiainen, K., Wiesmann, A., Mätzler, C, Werner, C., Rott, H., Nagler, T., Schneebeli, M., Proksch, M., Schüttemeyer, D., Kern, M., & Davidson, M. W. J. (2016). Nordic snow radar experiment. Geoscientific Instrumentation, Methods and Data Systems, 5(2), 403–415. doi: 10.5194/gi-5-403-2016.

Lemmetyinen, J., Pulliainen, J., Rees, A., Kontu, A., & Derksen, C. (2010). Multiple-layer adaptation of HUT snow emission model: comparison with experimental data. IEEE Transactions on Geoscience and Remote Sensing, 48(7), 2781–2794, doi:10.1109/TGRS.2010.2041357, 2010. 2608, 2619, 2626.

Le Toan, T., Beaudoin, J. R., & Guyon, D. (1992). Relating forest biomass to SAR data. IEEE Transactions on Geoscience and Remote Sensing, 30(2), 403–411. doi: 10.1109/36.134089.

Lin, C. C., Rommen, B., Floury, N., Schüttemeyer, D., Davidson, M. W. J., Kern, M., Kontu, A., Pulliainen, J., Wiesmann, A., Werner, C. L., Mätzler, C., Schneebeli, M., Proksh, M., & Nagler, T. (2016). Active microwave scattering signature of snowpack- Continuous multiyear SnowScat observation experiments. IEEE Journal of Selected Topics in Applied Earth Observation and Remote Sensing, 9(8), 3849–3869. doi: 10.1109/JSTARS.2016.2560168.

Liston, G. E., & Hiemstra, C. A. (2011). The changing cryosphere: Pan-Arctic snow trends (1979-2009). Journal of Climate, 24(21), 5691–5712. doi: 10.1175/JCLI-D-11-00081.1.

Liston, G. E., Mcfadden, J. P., Sturm, M., & Pielke, R. A. (2002). Modelled changes in arctic tundra snow, energy and moisture fluxes due to increased shrubs. Global Change Biology, 8(1), 17–32. doi: 10.1046/j.1354-1013.2001.00416.x.

Löwe, H., & Picard, G. (2015). Microwave scattering coefficient of snow in MEMLS and DMRT-ML revisited: The relevance of sticky hard spheres and tomography-based estimates of stickiness. Cryosphere, 9(6), 2101–2117. doi: 10.5194/tc-9-2101-2015.

Ma, W., Xiao, P., Zhang, X., Song, Y., Ma, T., & Ye, L. (2020). Retrieving snow wetness based on surface and volume scattering simulation. ISPRS Journal of Photogrammetry and Remote Sensing, 169, 17–28. doi: 10.1016/j.isprsjprs.2020.08.021.

Macelloni, G., Brogioni, M., Montomoli, F., & Fontanelli, G. (2012). Effect of forests on the retrieval of snow parameters from backscatter measurements. European Journal of Remote Sensing, 45(1), 121–132. doi: 10.5721/EuJRS20124512.

Macelloni, G., Brogioni, M., Montomoli, F., Paloscia, S., Lemmetyinen, J., Pulliainen, J., & Rott, H. (2014). Monitoring snow parameters in boreal forest using multi-frequency SAR data. In Proceedings of the 2014 XXXIth URSI General Assembly and Scientific Symposium (URSI GASS), Beijing, China, 16–23 August 2014; pp. 4–6.

Magagi, R., Bernier, M., & Ung, C. H. (2002). Quantitative analysis of RADARSAT SAR data over a sparse forest canopy. IEEE Transactions on Geoscience and Remote Sensing, 40(6), 1301–1313. doi: 10.1109/TGRS.2002.800235.

Marbouty, D. (1980). An experimental study of temperature-gradient metamorphism. Journal of Glaciology, 26(94), 303-312. doi: 10.3189/S0022143000010844.

Marsh, P., & Pomeroy, J. (1996). Meltwater fluxes at an Arctic forest-tundra site. Hydrological Processes, 10(10), 1383–1400. doi: 10.1002/(SICI)1099-1085(199610)10:10<1383::AID-HYP468>3.0.CO;2-W.

Marshall, H. P., Conway, H., & Rasmussen, L. A. (1999). Snow densification during rain. Cold Regions Science and Technology, 30(1–3), 35–41. doi: 10.1016/S0165-232X(99)00011-7.

Marshall, H., & Johnson, J. B. (2009). Accurate inversion of high-resolution snow penetrometer signals for microstructural and micromechanical properties. Journal of Geophysical Research, 114(F4), 1–18. doi: 10.1029/2009JF001269.

Mathieu, R., Sbih, M., Viau, A. A., Anctil, F., Parent, L. E., & Boisvert, J. (2003). Relationships between Radarsat SAR data and surface moisture content of agricultural organic soils. International Journal of Remote Sensing, 24(24), 5265–5281. doi: 10.1080/0143116031000115247.

Matson, M., & Wiesnet, D. R. (1981). New data base for climate studies. Nature, 289, 451-456. doi: 10.1038/289451a0.

Mätzler, C. (1996a). Microwave permittivity of dry snow. IEEE Transactions on Geoscience and Remote Sensing, 34(2), 573-581. doi: 10.1109/36.485133.

Mätzler, C. (1996b). Notes on microwave radiation from snow samples and emission of layered snowpacks (Research Report No. 96-09 1996, updated Feb. 2004 Notes 1 to 14). Bern: Institute of Applied Physics.

Mätzler, C. (1987). Applications of the interaction of microwaves with the natural snow cover. Remote Sensing Reviews, 2(2), 259–387. doi: 10.1080/02757258709532086.

Mätzler, C. (1998). Improved Born approximation for scattering of radiation in a granular medium. Journal of Applied Physics, 83(11), 6111–6117. doi: 10.1063/1.367496.

Mätzler, C. (2002). Relation between grain-size and correlation length of snow. Journal of Glaciology, 48(162), 461-466. doi: 10.3189/1727565027818.

Mätzler, C., & Melsheimer, C. (2006). Radiative transfer and microwave radiometry in Mätzler, C. (Ed.), Thermal Microwave Radiation – Applications for Remote Sensing (pp. 1-23). London: The Institution of Engineering and Technology.

Mätzler, C., & Wegmüller, U. (1987). Dielectric properties of freshwater ice at microwave frequencies. Journal of Physics D: Applied Physics, 20(12), 1623–1630. doi: 10.1088/0022-3727/20/12/013.

Mätzler, C., & Wiesmann, A. (1999). Extension of the microwave emission model of layered snowpacks to coarse-grained snow. Remote Sensing of Environment, 70(3), 317–325. doi: 10.1016/S0034-4257(99)00047-4.

Mätzler, C., Wiesmann, A., Schwank, M., & Proksch, M. (2014). Documentation for MEMLS _ Active Microwave Emission Model of Layered Snowpacks Adapted to Include Backscattering (Report No. 2013-03-MW). Bern: Institute of Applied Physics.

McNairn, H., Duguay, C., Brisco, B., & Pultz, T. (2002). The effect of soil and crop residue characteristics on polarimetric radar response. Remote Sensing of Environment, 80(2), 308–320. doi: 10.1016/S0034-4257(01)00312-1.

McNairn, H., Shang, J., Jiao, X., & Champagne, C. (2009). The contribution of ALOS PALSAR multipolarization and polarimetric data to crop classification. IEEE Transactions in Geoscience and Remote Sensing, 47(12), 3981–3992. doi: 10.1109/TGRS.2009.2026052.

Miller, D. A., & Adams, E. E. (2009). A microstructural dry-snow metamorphism model for kinetic crystal growth. Journal of Glaciology, 55(194), 1003–1011. doi: 10.3189/002214309790794832.

Montomoli, F., Macelloni, G., Brogioni, M., Lemmetyinen, J., Cohen, J., & Rott, H. (2016). Observations and simulation of multifrequency SAR data over a snow-covered boreal forest. IEEE Journal of Selected Topics in Applied Earth Observation and Remote Sensing, 9(3), 1216–1228. doi: 10.1109/JSTARS.2015.2417999.

Montomoli, F., Macelloni, G., Brogioni, M., Lemmetyinen, J., & Rott, H. (2015). Estimation of vegetation and soil backscattering for the retrieval of SWE in sparse forests. International IEEE Geoscience and Remote Sensing Symposium (IGARSS), 1602–1605. doi: 10.1109/IGARSS.2015.7326090.

Montpetit, B., Royer, A., Langlois, A., Cliche, P., Roy, A., Champollion, N., Picard, G., Domine, F., & Obbard, R. (2012). Instruments and methods new shortwave infrared albedo measurements for snow specific surface area retrieval. Journal of Glaciology, 58(211), 941–952. doi: 10.3189/2012JoG11J248.

Montpetit, B., Royer, A., Roy, A., & Langlois, A. (2018). In-situ passive microwave emission model parameterization of sub-arctic frozen organic soils. Remote Sensing of Environment, 205, 112–118. doi: 10.1016/j.rse.2017.10.033.

Montpetit, B., Royer, A., Roy, A., Langlois, A., & Derksen, C. (2013). Snow microwave emission modeling of ice lenses within a snowpack using the microwave emission model for layered snowpacks. IEEE Transactions in Geoscience and Remote Sensing, 51(9), 4705–4717. doi: 10.1109/TGRS.2013.2250509.

Mougin, E., Lopes, A., Karam, M. A., & Fung, A. K. (1993). Effect of tree structure on X band microwave signature of conifers. IEEE Transactions on Geoscience and Remote Sensing, 31(3), 655–667. doi: 10.1109/36.225532.

Mudryk, L. R., Derksen, C., Kushner, P. J., & Brown, R. (2015). Characterization of Northern Hemisphere snow water equivalent datasets, 1981-2010. Journal of Climate, 28(20), 8037–8051. doi: 10.1175/JCLI-D-15-0229.1.

Mudryk, L. R., Kushner, P. J., Derksen, C., & Thackeray, C. (2017). Snow cover response to temperature in observational and climate model ensembles. Geophysical Research Letters, 44(2), 919–926. doi: 10.1002/2016GL071789.

Mudryk, L., Santolaria-Otín, M., Krinner, G., Ménégoz, M., Derksen, C., Brutel-Vuilmet, C., Brady, M., & Essery, R. (2020). Historical Northern Hemisphere snow cover trends and projected changes in the CMIP6 multi-model ensemble. Cryosphere, 14(7), 2495–2514. doi: 10.5194/tc-14-2495-2020.

Nagare, R. M., Schincariol, R. A., Quinton, W. L., & Hayashi, M. (2012). Effects of freezing on soil temperature, freezing front propagation and moisture redistribution in peat: Laboratory investigations. Hydrology and Earth System Sciences, 16(2), 501–515. doi: 10.5194/hess-16-501-2012.

Nandan, V., Scharien, R., Geldsetzer, T., Mahmud, M., Yackel, J. J., Islam, T., Gill, J. P. S., Fuller, M. C., Gunn, G., & Duguay, C. (2017). Geophysical and atmospheric controls on Ku-, X- and C-band backscatter evolution from a saline snow cover on first-year sea ice from late-winter to pre-early melt. Remote Sensing of Environment, 198, 425–441. doi: 10.1016/j.rse.2017.06.029.

NASA. (2017). SnowEx17 Meteorological Station Data (Mesa West).

Natali, S. M., Watts, J. D., Rogers, B. M., Potter, S., Ludwig, S. M., Selbmann, A. K., Sullivan, P. F., Abbott, B. W., Arndt, K. A., Birch, L., Björkman, M. P., Bloom, A. A., Celis, G., Christensen, T. R., Christiansen, C. T., Commane, R., Cooper, E. J., Crill, P., Czimczik, C., … Zona, D. (2019). Large loss of CO2 in winter observed across the northern permafrost region. Nature Climate Change, 9(11), 852–857. doi: 10.1038/s41558-019-0592-8.

National Academies of Sciences, Engineering, and Medicine. (2019). Thriving on Our Changing Planet: A Decadal Strategy for Earth Observation from Space: An Overview for Decision Makers and the Public. Washington: The National Academies Press. doi: 10.17226/25437.

Nolin, A. W. (2010). Recent advances in remote sensing of seasonal snow. Journal of Glaciology, 56(200), 1141–1150. doi: 10.3189/002214311796406077.

Oh, Y., Sarabandi, K., & Ulaby, F. T. (1992). An empirical model and an inversion technique for radar scattering from bare soil surfaces. IEEE Transactions on Geoscience and Remote Sensing, 30(2), 370–381. doi: 10.1109/36.134086.

Ontario Ministry of Agriculture, Food, and Rural Affairs. (2017). Census of agriculture. Retrieved from https://www.omafra.gov.on.ca/english/stats/census/summary.html.

Ontario Ministry of Agriculture, Food, and Rural Affairs. (2020). Ontario gross domestic product (GDP) for agri-food sector, 2009-2019 ($ million). Retrieved from https://www.omafra.gov.on.ca/english/stats/economy/index.html.

Overland, J., Walsh, J., & Kattsov, V. (2017). Trends and feedbacks. In: Snow, Water, Ice and Permafrost in the Arctic (SWIPA) 2017 (pp. 9-23). Oslo: Arctic Monitoring and Assessment Programme (AMAP).

Park, S. E., Yamaguchi, Y., Singh, G., Yamaguchi, S., & Whitaker, A. C. (2014). Polarimetric SAR response of snow-covered area observed by multi-temporal ALOS PALSAR fully polarimetric mode. IEEE Transactions on Geoscience and Remote Sensing, 52(1), 329–340. doi: 10.1109/TGRS.2013.2240000.

Paterson, W. S. B. (1981). The physics of glaciers, 2nd ed. Oxford: Pergamon Press.

Picard, G., Arnaud, L., Domine, F., & Fily, M. (2009). Determining snow specific surface area from near-infrared reflectance measurements: Numerical study of the influence of grain shape. Cold Regions Science and Technology, 56(1), 10–17. doi: 10.1016/j.coldregions.2008.10.001.

Picard, G., Brucker, L., Roy, A., Dupont, F., Fily, M., Royer, A., & Harlow, C. (2013). Simulation of the microwave emission of multi-layered snowpacks using the Dense Media Radiative transfer theory: the DMRT-ML model. Geoscientific Model Development, 6(4), 1061–1078. doi: 10.5194/gmd-6-1061-2013.

Pinzer, B. R., Schneebeli, M., & Kaempfer, T. U. (2012). Vapor flux and recrystallization during dry snow metamorphism under a steady temperature gradient as observed by time-lapse micro-tomography. Cryosphere, 6(5), 1141–1155. doi: 10.5194/tc-6-1141-2012.

Pohl, S., Davison, B., Marsh, P., & Pietroniro, A. (2005). Modelling spatially distributed snowmelt and meltwater runoff in a small arctic catchment with a hydrology land-surface scheme (WATCLASS). Atmosphere-Ocean, 43(3), 193–211. doi: 10.3137/ao.430301.

Polder, D., & van Santen, J. H. (1946). The effective permeability of mixtures of solids. Physica, 12(5), 257-271. doi: 10.1016/S0031-8914(46)80066-1.

Pomeroy, J., & Gray, D. (1995). Snowcover Accumulation, Relocation, and Management (Science Report No. 7). Saskatoon: National Hydrological Research Institute, University of Saskatchewan.

Pomeroy, J. W., Gray, D. M., & Landine, P. G. (1993). The Prairie Blowing Snow Model : Characteristics , validation , operation. Journal of Hydrology, 144(1-4), 165–192. doi: 10.1016/0022-1694(93)90171-5.

Pomeroy, J. W., Marsh, P., & Gray, D. M. (1997). Application of a distributed blowing snow model to the arctic. Hydrological Processes, 11(11), 1451–1464. doi: 10.1002/(sici)1099-1085(199709)11:11<1451::aid-hyp449>3.0.co;2-q.

Proksch, M., Löwe, H., & Schneebeli, M. (2015). Density, specific surface area , and correlation length of snow measured by high-resolution penetrometry. Journal of Geophysical Research: Earth Surface, 120(2), 346–362. doi: 10.1002/2014JF003266.

Proksch, M., Mätzler, C., Wiesmann, a., Lemmetyinen, J., Schwank, M., Löwe, H., & Schneebeli, M. (2015). MEMLS3&a: Microwave Emission Model of Layered Snowpacks adapted to include backscattering. Geoscience Model Development, 8(8), 2605–2652. doi: 10.5194/gmdd-8-2605-2015.

ProSensing. (2009). X-band and Ku-band polarimetric scatterometers. Operations Manual. Amherst: ProSensing.

Pulliainen, J., Luojus, K., Derksen, C., Mudryk, L., Lemmetyinen, J., Salminen, M., Ikonen, J., Takala, M., Cohen, J., Smolander, T., & Norberg, J. (2020). Patterns and trends of Northern Hemisphere snow mass from 1980 to 2018. Nature, 581, 294-298. doi: 10.1038/s41586-020-2258-0.

Rango, A., Chang, A. T. C., & Foster, J. L. (1979). The utilization of spaceborne microwave radiometers for monitoring snowpack properties. Hydrology Research, 10(1). 25-40. doi: doi: 10.2166/nh.1979.0003.

Rannie, W. (2016). The 1997 flood event in the Red River basin: Causes, assessment and damages. Canadian Water Resources Journal, 41(1-2). doi: 10.1080/07011784.2015.1004198.

Rees, A., Lemmetyinen, J., Derksen, C., Pulliainen, J., & English, M. (2010). Observed and modelled effects of ice lens formation on passive microwave brightness temperatures over snow covered tundra. Remote Sensing of Environment, 114(1), 116–126. doi: 10.1016/j.rse.2009.08.013.

Riseborough, D., Anisimov, O., Guodong, C., Lunardini, V. J., Gavrilova, M., Köster, E. A., Koerner, R. M., Meier, M. F., Smith, M., Baker, H., Grave, N. A., Clapperton, C. M., Brugman, M., Hodge, S. M., Menchaca, L., Judge, A. S., Quilty, P. G., Hansson, R., Heginbottom, J.A., … Sayles, F. (1990). Seasonal snow cover, ice, and permafrost. In Tegart, W.J. McG., Sheldon, G.W, & Griffiths, D.C. (Eds.), Climate Change. The IPCC Impacts Assessment. Canberra: Australian Government Publishing Service.

Roth, C. H., Malicki, M. A., & Plagge, R. (1992). Empirical evaluation of the relationship between soil dielectric constant and volumetric water content as the basis for calibrating soil moisture measurements by TDR. Journal of Soil Science, 43(1), 1–13. doi: 10.1111/j.1365-2389.1992.tb00115.x.

Rott, H., Yueh, S. H., Cline, D. W., Duguay, C., Essery, R., Haas, C., Hélière, F., Kern, M., Macelloni, G., Malnes, E., Nagler, T., Pulliainen, J., Rebhan, H., & Thompson, A. (2010). Cold regions hydrology high-resolution observatory for snow and cold land processes. Proceedings of IEEE, 98(5), 752–765. doi: 10.1109/JPROC.2009.2038947.

Roy, A., Picard, G., Royer, A., Montpetit, B., Dupont, F., Langlois, A., Derksen, C., & Champollion, N. (2013). Brightness temperature simulations of the Canadian seasonal snowpack driven by measurements of the snow specific surface area. IEEE Transactions in Geoscience and Remote Sensing, 51(9), 4692–4704. doi: 10.1109/TGRS.2012.2235842.

Royer, A., Roy, A., Montpetit, B., Saint-Jean-Rondeau, O., Picard, G., Brucker, L., & Langlois, A. (2017). Comparison of commonly-used microwave radiative transfer models for snow remote sensing. Remote Sensing of Environment, 190(1), 247–259. doi: 10.1016/j.rse.2016.12.020.

Rutter, N., Pan, J., Durand, M., King, J., Derksen, C., & Larue, F. (2018). SnowEx17 laser snow microstructure specific surface area data: Version 1. Boulder: NASA National Snow and Ice Data Center, Distributed Active Archive Center. doi: 10.5067/H9C1UVWN1UK3.

Rutter, N., Sandells, M. J., Derksen, C., King, J., Toose, P., Wake, L., Watts, T., Essery, R., Roy, A., Royer, A., Marsh, P., Larsen, C., & Sturm, M. (2019). Effect of snow microstructure variability on Ku-band radar snow water equivalent retrievals. Cryosphere, 13(11), 3046-3059. doi: 10.5194/tc-13-3045-2019.

Rutter, N., Sandells, M., Derksen, C., Toose, P., Royer, A., Montpetit, B., Langlois, A., Lemmetyinen, J., & Pulliainen, J. (2014). Snow stratigraphic heterogeneity within ground-based passive microwave radiometer footprints: Implications for emission modeling. Journal of Geophysical Research, 119(3), 550–565. doi: 10.1002/2013JF003017.

Sandells, M., Essery, R., Rutter, N., Wake, L., Leppänen, L., & Lemmetyinen, J. (2017). Microstructure representation of snow in coupled snowpack and microwave emission models. Cryosphere, 11(1), 229–246. doi: 10.5194/tc-11-229-2017.

Schneebeli, M., & Johnson, J. B. (1998). A constant-speed penetrometer for high resolution snow stratigraphy. Annals of Glaciology, 26, 107–111. doi: 10.3189/1998AoG26-1-107-111.

Schneebeli, M., Pielmeier, C., & Johnson, J. B. (1999). Measuring snow microstructure and hardness using a high resolution penetrometer. Cold Regions Science and Technology, 30(1-3), 101–114. doi: 10.1016/S0165-232X(99)00030-0.

Sekelsky, S. M. (2002). Near-field reflectivity and antenna boresight gain corrections for millimeter-wave atmospheric radars. Journal of Atmospheric and Oceanic Technology, 19(4), 468–477. doi: 10.1175/1520-0426(2002)019<0468:NFRAAB>2.0.CO,2.

Shi, J., & Dozier, J. (2000). Estimation of snow water equivalence using SIR-C / X-SAR, Part I : Inferring snow density and subsurface properties. IEEE Transactions on Geoscience and Remote Sensing, 38(6), 2465–2474. doi: 10.1109/36.885195.

Sihvola, A., & Tiuri, M. (1986). Snow fork for field determination of the density and wetness profiles of a snow pack. IEEE Transactions on Geoscience and Remote Sensing, GE-24(5), 717–721. doi: 10.1109/TGRS.1986.289619.

Singh, G., Venkataraman, G., Yamaguchi, Y., & Park, S. E. (2014). Capability assessment of fully polarimetric alos-palsar data for discriminating wet snow from other scattering types in mountainous regions. IEEE Transactions on Geoscience and Remote Sensing, 52(2), 1177–1196. doi: 10.1109/TGRS.2013.2248369.

Smith, C. D., Kontu, A., Laffin, R., & Pomeroy, J. W. (2017). An assessment of two automated snow water equivalent instruments during the WMO Solid Precipitation Intercomparison Experiment. Cryosphere, 11(1), 101–116. doi: 10.5194/tc-11-101-2017.

Statistics Canada. (2020). Table 17-10-0009-01, Population estimates, quarterly. Retrieved from http://www150.statcan.gc.ca/t1/tbl1/en/tv.action?pid=1710000901.

Stiles, W. H., & Ulaby, F. T. (1981). Dielectric Properties of Snow (RSL Technical Report 527-1). Lawrence: Remote Sensing Laboratory.

Sturm, M., & Benson, I. C. S. (1997). Vapor transport, grain growth and depth-hoar development in the subarctic snow. Journal of Glaciology, 43(143), 42-59. doi: 10.3189/S0022143000002793.

Sturm, M., & Benson, C. (2004). Scales of spatial heterogeneity for perennial and seasonal snow layers. Annals of Glaciology, 38(1), 253–260. doi: 10.3189/172756404781815112.

Sturm, M., & Douglas, T. (2005). Changing snow and shrub conditions affect albedo with global implications. Journal of Geophysical Research, 110(G1), 1–13. doi: 10.1029/2005jg000013.

Sturm, M., Durand, M., Robinson, D., & Serreze, M. (2016). Got Snow? The Need to Monitor Earth's Snow Resources. Retrieved from https://snow.nasa.gov/sites/default/files/Got_SnowSM.pdf.

Sturm, M., & Holmgren, J. (1998). Differences in compaction behavior of three climate classes of snow. Annals of Glaciology, 26, 125–130. doi: 10.3189/1998AoG26-1-125-130.

Sturm, M., Holmgren, J., & Liston, G. (1995). A seasonal snow cover classification system for local to global applications. Journal of Climate, 8(5), 1261-1281. doi: 10.1175/1520-0442(1995)008<1261:ASSCCS>2.0.CO;2.

Sturm, M., Goldstein, Michael, A., & Parr, C. (2017). Water and life from snow: A trillion dollar science question. Water Resources Research, 53(5), 2051–2073. doi: 10.1002/2017WR020840.

Sturm, M., Liston, G. E., Benson, C. S., & Holmgren, J. (2001). Characteristics and growth of a snowdrift in Arctic Alaska, U.S.A. Arctic, Antarctic, and Alpine Research, 33(3), 319–329. doi: 10.1080/15230430.2001.12003436.

Sturm, M., Taras, B., Liston, G. E., Derksen, C., Jonas, T., & Lea, J. (2010). Estimating snow water equivalent using snow depth data and climate classes. Journal of Hydrometeorology, 11(6), 1380–1394. doi: 10.1175/2010JHM1202.1.

Surendar, M., Bhattacharya, A., Singh, G., Yamaguchi, Y., & Venkataraman, G. (2015). Development of a snow wetness inversion algorithm using polarimetric scattering power decomposition model. International Journal of Applied Earth Observation and Geoinformation, 42, 65–75. doi: 10.1016/j.jag.2015.05.010.

Techel, F., & Pielmeier, C. (2011). Point observations of liquid water content in wet snow - Investigating methodical, spatial and temporal aspects. Cryosphere, 5(2), 405–418. doi: 10.5194/tc-5-405-2011.

Thompson, A., & Kelly, R. (2019). Observations of a Coniferous Forest at 9.6 and 17.2 GHz : Implications for SWE Retrievals. Remote Sensing, 11(1), 1-6. doi: 10.3390/rs11010006.

Thompson, A., & Kelly, R. (2021a). Considerations for Ku-band radar retrieval of snow water equivalent at mid-latitude Ontario agricultural sites. Canadian Journal of Remote Sensing, 47(1), 119-142 . doi: 10.1080/07038992.2021.1898938.

Thompson, A, & Kelly, R. (2021b). Estimating wind slab thickness in a tundra snowpack. Remote Sensing Letters. Accepted for publication. doi: 10.1080/2150704X.2021.1961174.

Thompson, A., Kelly, R., & King, J. (2019). Sensitivity of Ku- and X-Band Radar Observations to Seasonal Snow in Ontario, Canada. Canadian Journal of Remote Sensing, 45(6), 829–846. doi: 10.1080/07038992.2019.1704621.

Tinga, W. R., Voss, W. A. G., & Blossey, D. F. (1973). Generalized approach to multiphase dielectric mixture theory. Journal of Applied Physics, 44(9), 3897–3902. doi: 10.1063/1.1662868.

Tiuri, M. (1984). The complex dielectric constant of snow at microwave frequencies. IEEE Journal of Oceanic Engineering, 9(5), 377-382. doi: 10.1109/JOE.1984.1145645.

Trudel, M., Magagi, R., & Granberg, H. B. (2009). Application of target decomposition theorems over snow-covered forested areas. IEEE Transactions on Geoscience and Remote Sensing, 47(2), 508–512. doi: 10.1109/TGRS.2008.2009122.

Tsang, L., Pan, J., Liang, D., Li, Z., Cline, D. W., & Tan, Y. (2007). Modeling active microwave remote sensing of snow using dense media radiative transfer (DMRT) theory with multiple-scattering effects. IEEE Transactions on Geoscience and Remote Sensing, 45(4), 990–1004. doi: 10.1109/TGRS.2006.888854.

Tuttle S. E., Cho, Eunsang, Restrepo, P. J., Jia, X., Vuyovich, C. M., Cosh, M. H., & Jacobs, J. M. (2017). Remote sensing of drivers of spring snowmelt flooding in the North Central U.S.. In: Lakshmi V. (Ed), Remote Sensing of Hydrological Extremes. Cham: Springer Remote Sensing/Photogrammetry. doi:10.1007/978-3-319-43744-6_2.

Ulaby, F. T., & Long, D. G. (2014). Microwave radar and radiometric remote sensing. Ann Arbor: University of Michigan Press.

Ulaby, F., Moore, R., & Fung, A. (1981). Microwave Remote Sensing: Active and Passive. Volume I. Microwave remote sensing fundamentals and radiometry. Reading: Addison-Wesley.

Ulaby, F., Moore, R., & Fung, A. (1986a). Microwave Remote Sensing: Active and Passive. Volume II. Radar Remote Sensing and Surface Scattering Emission Theory. Reading: Addison-Wesley.

Ulaby, F., Moore, R., & Fung, A. (1986b). Microwave Remote Sensing: Active and Passive. Volume III. Microwave Remote Sensing: From Theory to Applications. Reading: Addison-Wesley.

Ulaby, F. T., Sarabandi, K., McDonald, K., Whitt, M., & Dobson, C. M. (1990). Michigan microwave canopy scattering model. International Journal of Remote Sensing, 11(7), 1223–1253. doi: 10.1080/01431169008955090.

Ulaby, F. T., & Stiles, W. H. (1981). Microwave response of snow. Advances in Space Research, 1(10), 131–149. doi: 10.1016/0273-1177(81)90389-6.

Ulaby, F. T., Stiles, W. H., & Abdelrazik, M. (1984). Snowcover influence on backscattering from terrain. IEEE Transactions on Geoscience and Remote Sensing, GE-22(2), 126–133. doi: 10.1109/TGRS.1984.350604.

Ulaby, F. T., & van Zyl, J. J. (1990). Wave properties and polarization. In Ulaby, F.T., & Elachi, C. (Eds.), Radar Polarimetry for Geoscience Applications (pp. 2-16). Norwood: Artech House.

United States Department of Agriculture. (2018). Natural Resources Conservation Service, Soils. Web soil Survey. Retrieved from https://websoilsurvey.sc.egov.usda.gov/App/HomePage.htm.

van Zyl, J. J. (1989). Unsupervised classification of scattering behavior using radar polarimetry data. IEEE Transactions on Geoscience and Remote Sensing, 27(1), 36–45. doi: 10.1109/36.20273.

van Zyl, J. J. (1993). Application of Cloude's target decomposition theorem to polarimetric imaging radar data. Proceedings of SPIE, Radar Polarimetry, 1748, 184-191. doi: 10.1117/12.140615.

van Zyl, J. J., Arii, M., & Kim, Y. (2008). Requirements for model-based polarimetric decompositions. Proceedings of the 7th European Conference on Synthetic Aperture Radar, 417–420. Retrieved from https://ieeexplore.ieee.org/document/5757155.

van Zyl, J. J., Arii, M., & Kim, Y. (2011). Model-based decomposition of polarimetric SAR covariance matrices constrained for nonnegative eigenvalues. IEEE Transactions on Geoscience and Remote Sensing, 49(9), 3452–3459. doi: 10.1109/TGRS.2011.2128325.

van Zyl, J. J., & Kim, Y. (2011). Synthetic Aperture Radar Polarimetry. Hoboken: Wiley.

van Zyl, J. J., Zebker, H. A., & Elachi, C. (1987). Imaging radar polarization signatures: Theory and observation. Radio Science, 22(4), 529–543. doi: 10.1029/RS022i004p00529.

van Zyl, J. J., Zebker, H. A., & Elachi, C. (1990). Polarimetric SAR applications. In Ulaby, F. T., & Elachi, C. (Eds.), Radar Polarimetry for Geoscience Applications (pp. 315-360). Norwood: Artech House.

Vargel, C., Royer, A., St-Jean-Rondeau, O., Picard, G., Roy, A., Sasseville, V., & Langlois, A. (2020). Arctic and subarctic snow microstructure analysis for microwave brightness temperature simulations. Remote Sensing of Environment, 242(1), 111754. doi: 10.1016/j.rse.2020.111754.

Wang, J. R., & Schmugge, T. J. (1980). An empirical model for the complex dielectric permittivity of soils as a function of water content. IEEE Transactions on Geoscience and Remote Sensing, GE-18(4), 288–295. doi: 10.1109/TGRS.1980.350304.

Warren, S. G. (1982). Optical properties of snow. Reviews of Geophysics, 20(1), 67–89. doi: 10.1029/RG020i001p00067.

Watanabe, M., Shimada, M., Rosenqvist, A., Tadono, T., Matsuoka, M., Romshoo, S. A., Ohta, K., Furuta, R., Nakamura, K., & Moriyama, T. (2006). Forest structure dependency of the relation between L-band σo and biophysical parameters. IEEE Transactions on Geoscience and Remote Sensing, 44(11), 3154–3164. doi: 10.1109/TGRS.2006.880632.

Wegmüller, U., & Mätzler, C. (1999). Rough bare soil reflectivity model. IEEE Transactions on Geoscience and Remote Sensing, 37(3), 1391–1395. doi: 10.1109/36.763303.

Western Regional Climate Center. (2018). Mesa Lakes Resort, Colorado climate summary. Retrieved from https://wrcc.dri. edu/cgi-bin/cliMAIN.pl?co5520.

Wiesmann, A., Christian, M., & Weise, T. (1998). Radiometric and structural measurements of snow samples. Radio Science, 33(2), 273–289. doi: 10.1029/97RS02746.

Wiesmann, A., Fierz, C., & Mätzler, C. (2000). Simulation of microwave emission from physically modeled snowpacks. Annals of Glaciology, 31, 397–401. doi: 10.3189/172756400781820453.

Wiesmann, A., & Ma, C. (1999). Microwave Emission Model of Layered Snowpacks. Remote Sensing of Environment, 70(3), 307-316. doi: 10.1016/S0034-4257(99)00046-2.

Woodhouse, I. (2006). Introduction to microwave remote sensing. Boca Raton: CRC Press.

Wu, T. D., & Chen, K. S. (2004). A reappraisal of the validity of the IEM model for backscattering from rough surfaces. IEEE Transactions on Geoscience and Remote Sensing, 42(4), 743-753. doi: 10.1109/TGRS.2003.815405.

Xiong, C., Shi, J., & Lemmetyinen, J. (2014). Refinement of the X and Ku band dual-polarization scatterometer snow water equivalent retrieval algorithm. IEEE Geoscience and Remote Sensing Symposium (IGARSS), 2419–2422. doi: 10.1109/IGARSS.2014.6946960.

Yamaguchi, Y., Moriyama, T., Ishido, M., & Yamada, H. (2005). Four-component scattering model for polarimetric SAR image decomposition. IEEE Transactions on Geoscience and Remote Sensing, 43(8), 1699–1706. doi: 10.1109/TGRS.2005.852084.

Yamaguchi, Y., Sato, A., Boerner, W. M., Sato, R., & Yamada, H. (2011). Four-component scattering power decomposition with rotation of coherency matrix. IEEE Transactions on Geoscience and Remote Sensing 49(6), 2251–2258. doi: 10.1109/TGRS.2010.2099124.

Yosida, Z. (1955). Physical studies on deposited snow. 1. Thermal properties. Contributions from the Institute of Low Temperature Science, 7, 19–74. Retrieved from http://hdl.handle.net/2115/20216.

Yueh, S. H., Dinardo, S. J., Akgiray, A., West, R., Cline, D. W., & Elder, K. (2009). Airborne Ku-Band polarimetric radar remote sensing of terrestrial snow cover. IEEE Transactions on Geoscience and Remote Sensing, 47(10), 3347–3364. doi: 10.1109/TGRS.2009.2022945.

Zhu, J., Tan, S., King, J., Derksen, C., Lemmetyinen, J., & Tsang, L. (2018). Forward and inverse radar modeling of terrestrial snow using SnowSAR data. IEEE Transactions on Geoscience and Remote Sensing, 56(12), 7122-7132. doi: 10.1109/TGRS.2018.2848642.